UC Berkeley

UC Berkeley Previously Published Works

Title

Thermo-Hydro-Chemical Simulation of Mid-Ocean Ridge Hydrothermal Systems: Static 2D Models and Effects of Paleo-Seawater Chemistry

Permalink

https://escholarship.org/uc/item/2cm0j256

Journal

Geochemistry Geophysics Geosystems, 23(12)

ISSN

1525-2027

Authors

DePaolo, Donald J

Sonnenthal, Eric L

Pester, Nicholas J

Publication Date

2022-12-01

DOI

10.1029/2022gc010524

Copyright Information

This work is made available under the terms of a Creative Commons Attribution License, available at https://creativecommons.org/licenses/by/4.0/

Peer reviewed

eScholarship.org Powered by the California Digital Library
University of California

Check for updates

Geochemistry, Geophysics, Geosystems®

AGU ADVANCING EARTH AND SPACE SCIENCE

RESEARCH ARTICLE
10.1029/2022GC010524

Key Points:

- Mid-ocean ridge hydrothermal systems, a key component of global geochemical cycles, involve coupled heat transfer, fluid flow, and chemical reactions
- The thermo-hydro-chemical code ToughReact has the capabilities to simulate the coupled processes and improve understanding of these critical global systems
- We use the model to assess effects of different seawater chemistry in the Cretaceous and Precambrian, which include large differences in Sr isotope and Na exchange

Supporting Information:

Supporting Information may be found in the online version of this article.

Correspondence to:

D. J. DePaolo,
depaolo@eps.berkeley.edu

Citation:

DePaolo, D. J., Sonnenthal, E. L., & Pester, N. J. (2022). Thermo-hydro-chemical simulation of mid-ocean ridge hydrothermal systems: Static 2D models and effects of paleo-seawater chemistry. *Geochemistry, Geophysics, Geosystems*, *23*, e2022GC010524. https://doi.org/10.1029/2022GC010524

Received 12 MAY 2022
Accepted 8 NOV 2022

© 2022 The Authors.
This is an open access article under the terms of the Creative Commons Attribution-NonCommercial License, which permits use, distribution and reproduction in any medium, provided the original work is properly cited and is not used for commercial purposes.

Thermo-Hydro-Chemical Simulation of Mid-Ocean Ridge Hydrothermal Systems: Static 2D Models and Effects of Paleo-Seawater Chemistry

Donald J. DePaolo[1,2], Eric L. Sonnenthal[2], and Nicholas J. Pester[1,2]

[1]Department of Earth and Planetary Science, University of California, Berkeley, Berkeley, CA, USA, [2]Energy Geosciences Division, Lawrence Berkeley National Laboratory, Berkeley, CA, USA

Abstract Decades of research have resulted in characterization of the ocean floor manifestations of mid-ocean ridge (MOR) hydrothermal systems, yet numerical models accounting for the connections between heat transfer, hydrology and geochemistry have been slow to develop. The Thermo-hydro-chemical code ToughReact can be used to describe the coupled effects of fluid flow, heat transfer, and fluid-rock chemical interactions that occur in MOR systems. We describe the results of 2-dimensional simulations of steady state flow in fractured diabase with mineral-fluid chemical reactions. Basal heating and specified permeability yield maximum temperature of 400°C. Total fluid flux and high fracture flow velocities are in accord with observations. Fluid chemistry, mineralogical changes and $^{87}Sr/^{86}Sr$ ratios can be compared to observations to assess and calibrate models. Simulated high temperature fracture fluids have Mg and SO_4 near zero, elevated Ca and $^{87}Sr/^{86}Sr$ of about 0.7040. Total alteration is 10%–50% for simple models of spreading. Anhydrite forms mainly near the base of the upwelling zone and results in substantial local fracture porosity reduction. A calibrated model is used to predict how Sr isotopes and other features of altered oceanic crust would be different in the Cretaceous (95 Ma) early Proterozoic (1,800 Ma) and Archean (3,800 Ma), when seawater may have had high Ca and Sr concentrations, lower pH, higher temperature, and lower Na, Mg, and SO_4. The simulations are offered as a start on what ultimately may require a longer-term community effort to better understand the role of MOR thermo-hydro-chemical systems in Earth evolution.

Plain Language Summary This paper describes the results of a numerical simulation of the thermal, hydrological, and chemical processes that occur in a simplified mid-ocean ridge (MOR) hydrothermal system. The simulations exhibit the relationships between fluid flow, temperature, heat transfer, and mineral-fluid reactions. A simplified rock composition is used corresponding to diabase. The model accounts for flow mainly in fractures, and can reproduce many of the key aspects of seafloor vent fluid chemistry and the altered rocks found in ophiolites. Sr isotopes are also tracked. There are several key issues that must be addressed in constructing such models, and many of these are described in detail. The model parameters are calibrated against modern seafloor hydrothermal systems and then used to predict how the geochemical processes, including Sr isotope exchange, would be affected by changing seawater chemical composition, as is likely to be the case for Cretaceous, Paleozoic and Precambrian oceans. The simulations presented are viewed as a first step in building a more complete simulation capability for MOR hydrothermal systems to better understand their role in Earth evolution.

1. Introduction

One of the most powerful long-term drivers of seawater chemistry and global climate is chemical exchange in mid-ocean ridge (MOR) hydrothermal systems (Berner, 1991; Holland, 1984). Both experimental and field observations demonstrate that hydrothermal circulation results in a chemical flux to and from the oceans from altered basalt and diabase. Subseafloor reactions at elevated temperatures remove Mg and SO_4 from seawater, fixing them in secondary minerals within the crust, and release Ca and Sr from basalt (Elderfield & Schultz, 1996; Seyfried, 1987; Seyfried & Bischoff, 1979; Staudigel, 2003; Wheat & Mottl, 2000; Wolery & Sleep, 1976). In addition to the enhanced transport of transition metals that characterize "black smoker" fluids, associated chemical exchange modifies S, O, and Sr isotope ratios (Bickle & Teagle, 1992; Butterfield et al., 2001; Gregory, 2003; Hess et al., 1991; Muelenbachs, 1998; Muelenbachs et al., 2003; Palmer & Edmond, 1989; Seyfried & Shanks, 2004). Slow changes in the chemical fluxes in MOR systems over tens of millions of years

15252027, 2022, 12, Downloaded from https://agupubs.onlinelibrary.wiley.com/doi/10.1029/2022GC010524, Wiley Online Library on [21/06/2023]. See the Terms and Conditions (https://onlinelibrary.wiley.com/terms-and-conditions) on Wiley Online Library for rules of use; OA articles are governed by the applicable Creative Commons License

contribute to changes in the carbon cycle and hence contribute to changes in atmospheric CO_2 and global climate (Berner, 1991, 2003, 2004; Sleep et al., 2012; Sleep & Zahnle, 2001; Walker et al., 1981).

In this paper we present the results of simulations of a simplified model MOR hydrothermal system using the ToughReact software developed at Lawrence Berkeley National Laboratory (Sonnenthal et al., 2014; Xu et al., 2011). The simulator calculates flow and heat transport driven by a basal magmatic heat flux, and allows for flow concentrated in fractures, an important aspect of MOR systems. Fluid-rock chemical interaction by kinetically-controlled mineral dissolution and precipitation are included, which allows us to evaluate the model output by comparison to the chemistry of deep-sea vent fluids and mineralogical alteration observed in ophiolites and basement drill cores. We have also added a simulation of Sr isotope exchange, another gauge of fluid-rock interaction. The objectives are to better understand the relationships between heat transport, fluid flow, chemical interactions, and mineral alteration without imposing a flow regime, and using data available in the literature for mineral-fluid thermodynamics and reaction rates. The model we describe here, which is based loosely on fast-spreading ridges, reproduces many of the salient features of MOR hydrothermal systems and serves as a baseline to evaluate the effects of changing boundary conditions. We use the model specifically to investigate the effects of different paleo-seawater compositions, where Mg, SO_4, and pH were lower, and Ca, Sr, and temperatures were higher. Our simulations are offered as a first step in what probably requires a community effort to develop models that can serve as worthy accompaniment to continued observation and characterization of seafloor hydrothermal systems.

1.1. Value of a Thermo-Hydro-Chemical Modeling Framework

There is a lot known about MOR hydrothermal systems. This knowledge includes the basic features of fluid chemical evolution (quantitative Mg and SO_4 removal, Ca addition, Ca-Mg exchange, Sr isotopes), the extent and mineralogy of secondary mineral formation, the scale of the fluid fluxes and heat transfer, and the role of fractures in focusing fluid flow. But there is also a lot that is not known, and probably cannot be inferred solely from observation of active systems or ophiolites. For example, there is little knowledge of the internal structure of active systems—such as the 2D and 3D distribution of fluid flow velocities and temperature, and in particular their relation to mineral stability, reaction rates, and secondary mineral formation. Vent fluids can be sampled, which are an end product of the fluid-rock exchange, and one that may not be entirely representative, but the evolution of the fluids, and the likely range of fluid compositions within the system, cannot be directly observed (cf. Larson et al., 2015).

Reconstructing hydrothermal system evolution from observations is difficult, because the fluids are always moving, being heated, flow velocities increasing as heating progresses (see below), being refreshed and mixed with new cooler, less evolved fluid, and responding to competing reaction kinetics of the dissolving unstable primary minerals, and precipitating secondary minerals. A further complication not applicable to continental hydrothermal systems is that fresh new rock is continually being made at the ridge axis, and this rock then migrates through the temperature-flow field as the seafloor spreads. Although it has been argued that the first order features of vent fluids can be understood in terms of "equilibration" of the fluids with the rocks at high temperature, there is little likelihood that the fluids, especially those flowing in fractures at velocities of 100's of meters per year under conditions of changing pressure and temperature, are generally equilibrated with the rocks. Even if they approach equilibrium at 400°C, they will not necessarily be at equilibrium at 100°C, 200°C, or 300°C.

Because the controlling parameters in modern systems are difficult to describe quantitatively, it is difficult to predict geochemical changes when conditions are changed. For example, in modern systems, there is a large range of seafloor spreading rates. Flow models have been best developed for fast-spreading ridges, which may be the most systematic (Coumou et al., 2008; Hasenclever et al., 2014; Theissen-Krah et al., 2011, 2016). Fluid heating in slower spreading ridges must be different, as is the depth of fluid penetration (Barreyre et al., 2018; Kanzaki, 2020).

The chemical composition of seawater has not been constant through Earth history. Modern seawater has the critical reactive components Mg^{2+}, Ca^{2+} and SO_4^{2-} in the concentration ratios 54:10:28 (in mmol/kg). Available data indicate that during the Cretaceous and early Paleozoic, seawater had lower $Mg^{2+}$and SO_4^{2-}, and higher Ca^{2+} (Blättler & Higgins, 2014; Holland, 2003; Horita et al., 2002; Lowenstein et al., 2001, 2014; Turchyn

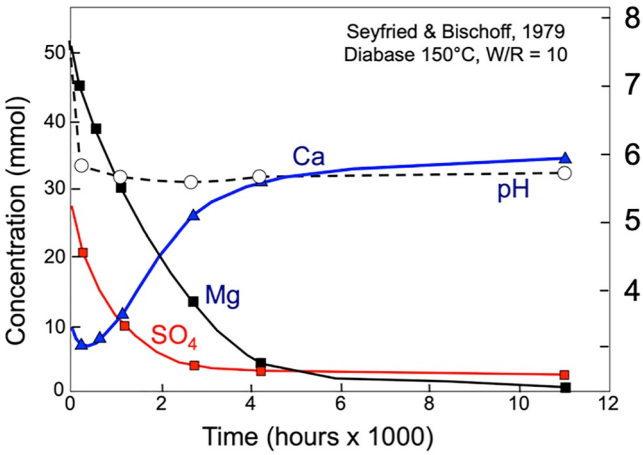

Figure 1. Changes in fluid Ca, Mg, SO_4, and pH, during an experiment where a seawater-like fluid is reacted with diabase at 150°C. At this temperature the experimental timescale for Mg removal is about 3,000 hr or about 0.35 years, with mineral reactive surface area maximized. In this amount of time, fracture fluids can flow more than 100 m, a clear indication that fracture fluids in a mid-ocean ridge hydrothermal system will not be in equilibrium with the surrounding rock matrix. This type of situation requires a reactive transport model to simulate the fluid and rock evolution in time and space.

& DePaolo, 2019). These differences, possibly also aided by differences in deep water temperature and pH (Coogan & Gillis, 2013, 2018), could change the amount and character of basalt-seawater chemical interaction (Antonelli et al., 2017; Coogan, 2009). Similar, perhaps more extreme, differences in seawater chemistry also apply to the Precambrian, when SO_4 may have been extremely low (Crowe et al., 2014; Habicht et al., 2002; Lowenstein et al., 2001, 2014) and Ca (and Sr?) extremely high (Halevy & Bachan, 2017). Possible evidence of these types of differences is shown by effects on Sr isotopes in altered rocks of Cretaceous ophiolites (Coogan, 2009).

The Sr isotope effect is also important because seawater $^{87}Sr/^{86}Sr$ is viewed as a monitor of the magnitude of global hydrothermal MOR geochemical fluxes (Francois & Walker, 1992; Hess et al., 1991; Palmer & Edmond, 1989) versus those for continental weathering. For example, slower spreading ridges have vent fluid with lower $^{87}Sr/^{86}Sr$ than fast spreading ridges (Bach & Humphris, 1999), but it is unclear how to generalize this observation into a statement about the relationship between global seafloor generation rates and the intensity of seawater-basalt chemical interaction.

2. Model Constraints From Observations

Models are of most value when there are sufficient constraints from observation, and for MOR systems there are abundant constraints. This section is a brief review of some of the key observations and previous modeling that are used to construct and evaluate the numerical THC model.

2.1. Hydrothermal Experiments

Much of the modern understanding of MOR chemical exchange is based on a combination of hydrothermal experiments (Berndt et al., 1988; Mottl & Holland, 1978; Rosenbauer & Bischoff, 1983; Seyfried & Bischoff, 1981; Seyfried & Janecky, 1985; Seyfried & Mottl, 1982), and detailed studies of the chemical composition of hydrothermal springs from active ridges (Butterfield et al., 1990, 1994, 2001; Charlou et al., 1996; Edmond et al., 1979, 1982; Gallant & Von Damm, 2006; Lilley et al., 2003; Michard et al., 1984; Pester et al., 2011, 2012, 2014; Seyfried et al., 2011; Von Damm et al., 1985).

The canonical fluid evolution is represented well by the results of 150°C seawater-basalt reaction experiments (Figure 1) by Seyfried and Bischoff (1979). As fluid reacts with diabase, the Mg and SO_4 concentrations decrease rapidly, ultimately going to effectively zero. In a compensatory way, Ca increases after first decreasing somewhat. The fluid starts with a pH close to 8, and ends at about 5.7. The final Ca concentration can be calculated approximately from charge balance, since the initial sum $(Ca + Mg–SO_4)_{SW}$ must be equal to that in the final fluid (this issue is treated more fully below). At higher temperature the fluids evolve more quickly and the ultimate pH is lower.

A key constraint from experimental studies is that high temperature vent fluids have near-zero Mg and SO_4 concentrations, and elevated Ca approximately equal to the initial Ca plus initial $(Mg–SO_4)$. As noted below, real fluids are more complicated because some SO_4 gets reduced to HS^-, the Na^+ concentration can change, especially if there is phase separation, and K^+, Fe^{2+}, and HCO_3^- also come into play.

2.2. Vent Fluid Chemistry

Vent fluid chemical and isotopic compositions have been studied extensively (Allen & Seyfried, 2003; Bach & Humphris, 1999; Bowers & Taylor, 1986; Bowers et al., 1988; Butterfield et al., 1990, 1994, 2001; Charlou et al., 1996; Edmond et al., 1979, 1982; Kadko & Butterfield, 1998; Kadko & Moore, 1988; Kadko et al., 1985; Kuhn et al., 2003; Lilley et al., 2003; Mottl et al., 2011; Ono et al., 2007; Pester et al., 2011, 2012, 2014; Seyfried et al., 2011; Von Damm, 1995; Von Damm et al., 1985; Wheat & Mottl, 2000). These studies provide information on the residence time, temperature history, reaction rates, and fluid-mineral reactions that apply to fluids in MOR

15252027, 2022, 12, Downloaded from https://agupubs.onlinelibrary.wiley.com/doi/10.1029/2022GC010524, Wiley Online Library on [21/06/2023]. See the Terms and Conditions (https://onlinelibrary.wiley.com/terms-and-conditions) on Wiley Online Library for rules of use; OA articles are governed by the applicable Creative Commons License

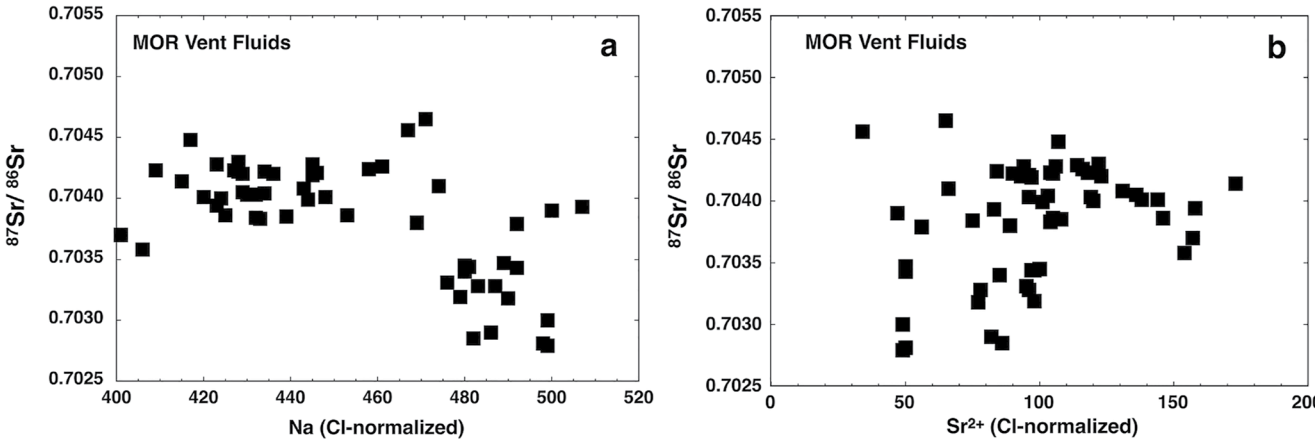

Figure 2. (a) Summary of vent fluid $^{87}Sr/^{86}Sr$ versus Na^+. Most fluids have $^{87}Sr/^{86}Sr$ near 0.7040 ± 0.0003 except for a set of high-Na (and low-Ca) fluids that have lower values more closely approaching those of the rocks (0.7025–0.7028). (b) Vent fluid $^{87}Sr/^{86}Sr$ versus Sr^{2+}. The isotope ratio helps constrain the total amount of fluid-rock interaction, and the Sr concentration helps constrain Sr partitioning into secondary phases. Data from a compilation of vent fluid analyses for which there are multiple measured parameters.

systems. As noted above, one key reaction effect that needs to be captured in reactive transport models is that Mg and SO_4 go to zero and Ca increases in the fluids. The changes related to Mg, Ca, and SO_4 are partly controlled by a charge balance constraint:

$$\left(Ca^{2+} + Mg^{2+} + SO_4^{2-}\right)_{SW} = \left(Ca^{2+} + Mg^{2+} + SO_4^{2-}\right)_{Vent} + \left(Fe^{2+} + 0.5\Delta K^{+}\right)_{Vent} \quad (1)$$

where ΔK^+ is the net change in K concentration from seawater to vent fluid. In most vent fluids the sum $(Fe^{2+} + 0.5\Delta K^+) \approx 10 \pm 5$ mmol, so this charge balance predicts for modern seawater that $(Ca^{2+})_{Vent} \approx 26$ mmol, which accords with observations. Additional second order complications at the ±2 mmol level are generated by reduction of SO_4 to HS-, and the addition of seawater HCO_3^- (2 mmol in seawater) to the balance.

Another type of constraint comes from Sr concentrations and Sr isotopes of vent fluids (Figure 2). The most common $^{87}Sr/^{86}Sr$ values are in the range 0.7037–0.7043, which represent a mixture of approximately 80% basalt-derived Sr and 20% seawater-derived Sr. A number of vents have lower $^{87}Sr/^{86}Sr$ of 0.7027–0.7035, and there is a correlation between spreading rate and average $^{87}Sr/^{86}Sr$ with faster spreading ridge values being generally above 0.7040 (Bach & Humphris, 1999). The isotopic data provide key constraints that can be used to evaluate and calibrate reactive transport models. The Sr isotopic data are also important because they are a sensitive measure of fluid-rock exchange, and the Sr concentration data are needed because they constrain the partitioning of Sr into secondary phases (cf. Gillis et al., 2005; Syverson et al., 2018).

Geochemical data have also been used to estimate the residence time of fluids in the hydrothermal system. Based on ^{226}Ra data Kadko and Moore (1988) and Kadko and Butterfield (1998) estimate that the residence time of fluid from first reaching 200°C to venting is less than 3 years in hydrothermal systems along the Juan de Fuca ridge where spreading rate is about 6 cm/yr.

2.3. Mineralogical and Structural Studies of Ophiolites and Drill Cores

There are many observations from ophiolites and basement drilling into the ocean floor that relate to mineralogical effects of hydrothermal alteration and hydrological characteristics (e.g., Alexander et al., 1993; Alt, 1995; Alt & Teagle, 2000; Alt et al., 2010; Bickle & Teagle, 1992; Bosch et al., 2004; Coogan, 2009; Coogan & Dosso, 2012; Farough et al., 2016; Fisher et al., 2014; Gillis, 1995; Gillis et al., 2005; Heft et al., 2008; Staudigel, 2003; Teagle et al., 1998, 2003). The most widely cited summary is that of Alt et al. (1986, 1996) from ODP Site 504B, which shows that in the warmer part of the system the primary secondary minerals are chlorite, albite, prehnite, tremolite-actinolite, and epidote, generally also including some mixed-layer chlorite-smectite, pyrite, talc, magnetite, titanite, quartz, and hornblende. This assemblage is typical of lower greenschist facies metamorphism of basalt.

15252027, 2022, 12, Downloaded from https://agupubs.onlinelibrary.wiley.com/doi/10.1029/2022GC010524, Wiley Online Library on [21/06/2023]. See the Terms and Conditions (https://onlinelibrary.wiley.com/terms-and-conditions) on Wiley Online Library for rules of use; OA articles are governed by the applicable Creative Commons License

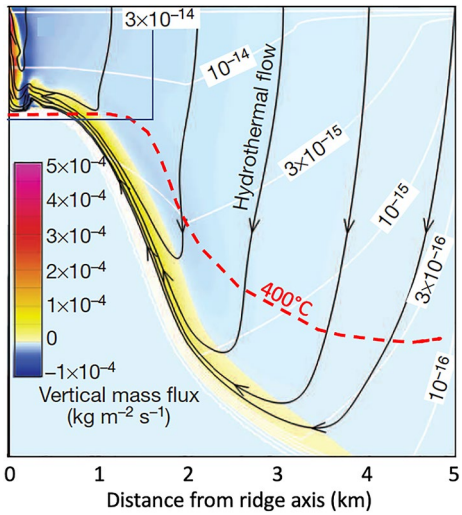

Figure 3. A 5 × 5 km cross section showing permeability contours (white lines), fluid flux values (color scale), and flow lines (black) for a 2D version of a thermo-hydrologic model of a fast-spreading ridge (Hasenclever et al., 2014). In this model, the deep circulation at distances greater than 1.5 km from the ridge axis cools the crust so that there is no magma present at depths less than 4–5 km as suggested by seismic data (Theissen-Krah et al., 2016). Virtually all of the near-axis flow is in rocks with $T \leq 400$°C. Our model domain corresponds to the 1.2 km high by 1.6 km wide rectangle at the upper left, but does not include the deeper flow.

With regard to permeability and fracture distribution, various studies of ophiolites have concluded that typical matrix porosity is 10% in basalt flows, and 2%–4% in sheeted dikes (Alt, 1995). Matrix permeabilities are in the range 10^{-14} (basalt) to 10^{-17} m^2 (dikes). Other studies have estimated slightly different values (Fisher et al., 2014; Gilbert and Bona, 2016; Gillis & Sapp, 1997; Nehlig, 1994). Fracture spacing typically varies between about 0.5 and 4 m in ophiolites, with 2 m being close to an average (Nehlig, 1994; van Everdingen, 1995).

2.4. Thermal-Hydrological Modeling

Early work on this issue emphasized the fluid fluxes required to account for the ocean floor heat flow data as a function of distance from ridge axes and age (Lowell, 1975; Sleep, 1991; Stein & Stein, 1994). These estimates are still useful guidelines for overall fluid fluxes. There are in fact relatively few studies where the fluid flow has been modeled in detail (Coumou et al., 2008, did the near-axis region), but there are other recent studies, in particular Hasenclever et al. (2014; also see Cherkaoui et al., 2003; Kanzaki, 2020; Theissen-Krah et al., 2016), which provide constraints on fluid fluxes and flow velocities.

Hasenclever et al. (2014) describe a 3D modeling study that resulted in a steady state flow and temperature field for a model fast spreading ridge (11 cm/yr full spreading rate; Figure 3). Some key features of their model, shown here in the 2D version, that are important for this work are (a) permeability at about 1 km depth is about 10^{-14} m^2, (b) there is a broad zone of fluid downwelling where fluid fluxes are small, extending outward from about 400 m from the ridge axis, (c) the near-ridge upwelling zone is narrow (ca. 100 m half-width) with fluid fluxes of 2–4 × 10^{-4} kg/m^2/s, and (d) there is a near-ridge downwelling zone with relatively high fluid fluxes (a few ×10^{-5} kg/m^2/s) that is about 150–300 m from the ridge axis. These four features are reproduced in our reactive transport model described below, but there is a fifth feature in the Hasenclever et al. (2014) model that is noteworthy. There is a zone of higher temperature fluid flow, just above the magma lens, that supplies roughly 40% of the total upwelling fluid at the ridge axis even though the fluid flow velocities are small. This part of the flow is an inference, based on the seismic structure typically observed (Theissen-Krah et al., 2016), but also helps to explain observed alteration at temperatures in excess of 400°C as described in Alt et al. (2010). The deep circulation cools the crust sufficiently so that there is no melt present at 5 km depth a few km from the ridge axis. A similar feature is found in the much earlier model of Cathles (1993).

Most of the features of the Hasenclever et al. study are found in the 2D models of Kanzaki (2020) for 9 cm/yr spreading rate. His models also show a narrow (100 m half-width) upwelling zone very near the ridge axis, a near-ridge enhanced-downwelling zone 150–300 m from the axis, and strong circulation down to about 1.5 km depth.

2.5. Models of Magma Chambers and Crustal Structure

A critical aspect of modeling hydrothermal circulation is the flux of heat supplied to the system from the magma chamber and/or dikes under and within the ridge at shallow depths below the seafloor. This aspect of ridges is not well constrained by heat flow measurements, is understood mainly as a result of modeling studies, and is best developed for fast spreading ridges where the geometry is likely to be simplest. For a spreading rate of 80–110 mm/yr, the depth to the top of the magma lens is estimated to be 1.4–1.6 km (Chen & Morgan, 1996; Canales et al., 2005; Figure 4). If we assume that the temperature at the base of the hydrothermal system is 400°C, the temperature of the top of the magma lens is 1,100°C (e.g., Liu & Lowell, 2009), and the distance is 200 m, then the steady state heat flux would be about 7 W/m^2 if the thermal conductivity is 2 W/m/K. If this flux is distributed over a distance of ±1 km from the ridge axis, the total heat supply would be 14 MW per kilometer of ridge length. This value is lower than estimated based on measured and modeled vent field heat fluxes, which are closer to 20–27 MW/km for spreading rates of 70–100 mm/yr (Baker, 2007). However, this difference might be expected because the sampled vent fields generally represent the highest temperature fluids, which if the convection is anything like that modeled by Coumou et al. (2008, 2009), are

15252027, 2022, 12, Downloaded from https://agupubs.onlinelibrary.wiley.com/doi/10.1029/2022GC010524, Wiley Online Library on [21/06/2023]. See the Terms and Conditions (https://onlinelibrary.wiley.com/terms-and-conditions) on Wiley Online Library for rules of use; OA articles are governed by the applicable Creative Commons License

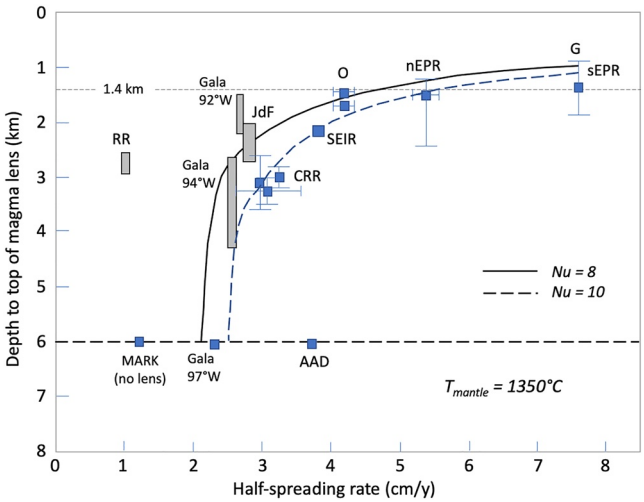

Figure 4. Summary figure adapted from Canales et al. (2005) showing that inferred depth to the magma lens varies with seafloor spreading rate. The heat flux values used for our simulations are roughly consistent with a magma lens at 1.4 km depth, which would correspond to full spreading rate of about 10 cm/yr. The dark lines correspond to Nusselt numbers of 8 and 10, which describe the ratio of advected heat to conducted heat in the hydrothermal system assuming a mantle temperature of 1,350°C. Ridge localities shown are RR (Reykjanes), JdF (Juan de Fuca), nEPR and sEPR (northern and southern East Pacific), O (EPR north of Orozco transform), CRR (Costa Rica), SEIR (Southeast Indian), G (EPR south of Garret Transform), Gala (Galapagos), MARK (mid-Atlantic south of Kane transform), AAD (Australia-Antarctic discordance).

not representative of the average near-axis heat flux but rather are biased toward higher values due to the focusing of upward advection. A different approach to estimating heat flux that attempts to couple magma cooling to hydrothermal convection, yields values of about 10 W/m^2 at the axis (Liu & Lowell, 2009), more in accord with the simple calculation based on temperatures and distance.

3. Elements of a Reactive Transport Model

The objective of the current work is to produce a 2D model of fluid flow, heat transfer, and chemical reactions between fluid and rock to test whether a simple version of the system can reproduce some of its important features, and yield a picture of the inner structure and relationships between temperature, flow, fluid chemistry, and rock alteration. As constraints we expect the model to produce vent fluids with chemistry and Sr isotopic composition that resemble those observed, using heat flux, permeability, and fracture spacing values that are believed to match typical MORs. A further constraint is that the mineralogy and extent of rock alteration should be compatible with observations.

The software used here is Tough React version 3.68 (Sonnenthal et al., 2014), which can simulate heat and mass transfer by circulating fluids (as in the TOUGH2 code), plus fluid-mineral interactions via dissolution of primary phases and precipitation/growth of secondary mineral phases. The code can handle any number of primary and secondary mineral phases, including minerals with solid solutions, and the database can be modified to simulate trace elements and isotopes. The code has a dual-permeability feature, critical for seafloor hydrothermal systems, that accounts for flow mainly in fractures and fracture-matrix communication by fluid phase chemical and thermal diffusion. The dual-permeability feature is advantageous for representing the fractured rocks of the oceanic crust, but it also introduces some effects that require evaluation (discussed further elsewhere in this manuscript), depending on how the capabilities of the software are employed. The code has many more features than are used in this study; adding them may be useful in future refinements of this work.

3.1. Specifications and Simplifications

To begin to use the ToughReact code to simulate a MOR hydrothermal system, it is desirable to reduce the complexities of the natural system to a level where essential aspects of the system are represented, but the boundary conditions and other aspects of the system are simplified. This process of conceptualizing the natural system for simulation involves a number of decisions, and ultimately the only way to evaluate the effects of those decisions is to change them systematically and determine what effects those changes have on the outcomes. Only part of this parameter sensitivity analysis has been done, but it is in any case a continuing process. In the remainder of this section the model computational grid set-up and input parameter decisions are described, as is their relationship to the known, measured, and inferred characteristics of MORs. The approach is to keep the model as simple as possible initially to determine how well a simple model reproduces observations. Adding additional complexity, and evaluating the impact of those additions, is a longer-term objective.

The simulations we have done, constructed to represent the hydrothermal circulation above a simplified fast-spreading ridge, have the following characteristics. Items with an asterisk are discussed further in subsequent sections.

1. A rectangular* computational grid that represents basalt and diabase overlain by an ocean of infinite volume with the seawater chemical composition and typical deep-water temperature (Figure 5).
2. Uniform rock permeability dominated by fracture permeability.*
3. Fractures spaced 2 m apart throughout the domain, both horizontally and vertically.
4. Rock of relatively simple mineralogy composed of plagioclase, clinopyroxene, orthopyroxene, olivine and magnetite.

15252027, 2022, 12, Downloaded from https://agupubs.onlinelibrary.wiley.com/doi/10.1029/2022GC010524, Wiley Online Library on [21/06/2023]. See the Terms and Conditions (https://onlinelibrary.wiley.com/terms-and-conditions) on Wiley Online Library for rules of use; OA articles are governed by the applicable Creative Commons License

15252027, 2022, 12, Downloaded from https://agupubs.onlinelibrary.wiley.com/doi/10.1029/2022GC010524, Wiley Online Library on [21/06/2023]. See the Terms and Conditions (https://onlinelibrary.wiley.com/terms-and-conditions) on Wiley Online Library for rules of use; OA articles are governed by the applicable Creative Commons License

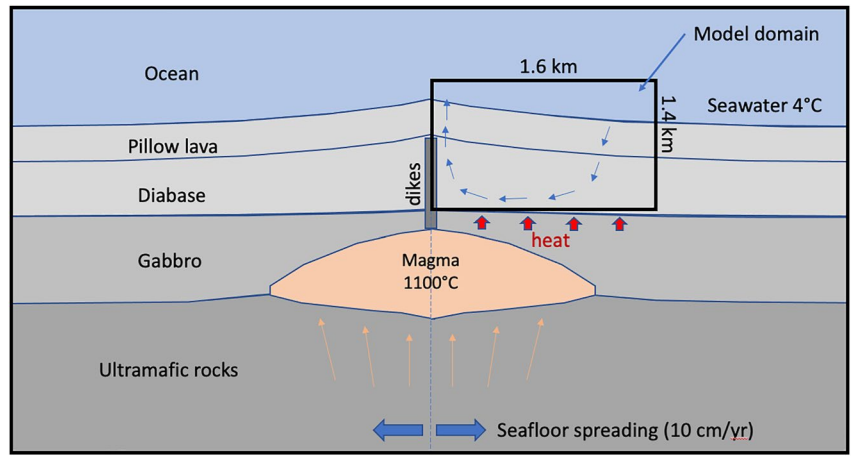

Figure 5. Schematic cross section of a fast-spreading ridge and the relationship to the model domain used for simulation. Our simulations vary from this picture in that (1) they do not include heating from dikes, (2) the upper boundary between rock and ocean is horizontal, as is the lower boundary, and (3) the rock section has uniform permeability rather than a layered structure.

5. Heating from below that mimics the effects of a steady state magma chamber centered on the ridge axis and about 200 m below the circulating fluids (Figure 4).*

There are a number of other specified aspects of the model.

1. No seafloor spreading.*
2. No dikes providing transient heating.
3. No glass in the rock, just igneous minerals as a starting composition.
4. First order kinetics for both dissolution and precipitation (Text S1 in Supporting Information S1).
5. Thermodynamic database modified from SOLTHERM.H6 (Reed and Palandri, 2006, and references therein).
6. Mineral specific reactive surface areas (RSA) are adjustable, but all primary minerals have the same values* Secondary mineral RSA are typically twice those of the primary minerals, except for quartz and albite, which are typically larger.*
7. Ionic diffusivities are temperature-dependent but all the same.
8. Salt-free water equation of state is used.
9. Permeability does not change due to dissolution and precipitation.*
10. 17 chemical components.
11. 5 primary minerals (plus Ca-Na and Mg-Fe solid solutions).
12. 16 secondary minerals (some with multiple components including Sr endmembers).
13. Sr and Sr isotope components are added into the thermodynamic database for plagioclase, clinopyroxene, anhydrite, tremolite and epidote (Text S2 in Supporting Information S1).

The mineral-fluid reactions are governed by temperature and pH—dependent kinetic rate constants, most of which have been taken from the compilation of Palandri and Kharaka (2004), but with some modifications for clinopyroxene, plagioclase, and anhydrite. For anhydrite we have used celestite kinetics from Dove and Czank (1995), which are consistent with the experimental results of Syverson et al. (2018). We use the thermodynamic data for clinopyroxene (CPX) proposed by Aradóttir, Sonnenthal, and Jónsson (2012). The formulations for each mineral and additional discussion of plagioclase and CPX kinetics, are provided in Text S1 in Supporting Information S1.

3.2. Rock Chemistry and Mineralogy

3.2.1. Primary Mineralogy

The rock mineralogy used has 56% plagioclase and 22% CPX, using the compositions An_{60} and the pyroxene used by Aradóttir, Sonnenthal, Björnsson, and Jónsson (2012). In addition, there is 15% orthopyroxene (OPX, Mg_{67}), 4% olivine (Mg_{75}), and 3% magnetite. Rock potassium is represented by 1% microcline reacting with

15252027, 2022, 12, Downloaded from https://agupubs.onlinelibrary.wiley.com/doi/10.1029/2022GC010524, Wiley Online Library on [21/06/2023]. See the Terms and Conditions (https://onlinelibrary.wiley.com/terms-and-conditions) on Wiley Online Library for rules of use; OA articles are governed by the applicable Creative Commons License

Table 1
Compositions of Model Diabase and Typical Mid-Ocean Ridge Basalt[a]

	Model	All MORB	N-MORB
SiO_2	50.11	50.47	50.42
Al_2O_3	15.39	14.70	15.13
Fe_2O_3	3.53	0.00	0.00
FeO	7.76	10.43[b]	9.82[b]
MgO	8.73	7.58	7.76
CaO	12.02	11.39	11.35
Na_2O	2.31	2.79	2.83
K_2O	0.16	0.165	0.14
Sr	115	129	128

[a]MORB compositions are from a compilation by Gale et al. (2013). Oxide concentrations in weight percent, Sr in parts per million. [b]Total Fe as FeO.

kinetics identical to plagioclase. For many of the simulations there is no mineral phase containing K, and there is no calcium carbonate phase in the secondary assemblage. The addition of K and a carbonate mineral have little effect on the outcomes. The primary minerals plagioclase and CPX include Sr (220 and 17.6 ppm respectively) with an $^{87}Sr/^{86}Sr = 0.7028$, which is the average for all MORs (Gale et al., 2013). Secondary Sr-bearing minerals are anhydrite ($K_{Sr/Ca} = 0.16$), tremolite ($K_{Sr/Ca} = 0.05$) and epidote ($K_{Sr/Ca} = 0.2$). More detail on the Sr partitioning and Sr isotopes is provided in Text S2 in Supporting Information S1. The primary mineral proportions yield an overall rock composition for the fresh rock that resembles MOR basalt and has Mg# = 62 (Table 1).

3.2.2. Secondary Mineralogy

Although there are other secondary minerals included in the simulations, the major secondary minerals that form in the simulations (in addition to anhydrite) are chlorite (clinochlore–daphnite), amphibole (tremolite–actinolite), and montmorillonite (Na, Ca, Mg, and K—montmorillonite). Minor amounts of epidote and substantial amounts of albite form in the highest temperature cells, and some pyrite forms where there are higher concentrations of HS^-. Low-Ca secondary feldspar is represented by three components, with An_0, An_{10} and An_{20}. Brucite does not form. For the amphibole, anhydrite and epidote, the thermodynamic database has been amended to include Sr-bearing mineral endmembers with thermodynamic data based on the Ca endmember to achieve the specified equilibrium Sr/Ca partitioning into the secondary minerals (see Text S2 in Supporting Information S1).

3.3. Heat Generation Profiles and Temperature

Two versions of the heat generation profile have been used, but the results presented here are mainly using profile 2 (Figure 6), which should be appropriate for fast spreading ridges. The maximum heat flux is 8 W/m^2 at the ridge axis. Simulations were also done using profile 2, a maximum axial heat flux of 10 W/m^2 and higher permeability ($3e-14$ m^2). This combination produces multiple thermal plumes rather than a simpler whole-system circulation. Although this type of flow could be realistic in fast spreading ridges, it was not pursued further for this study.

The heat generation profiles are Gaussian with the variable parameters being the standard deviation in meters, and a maximum and minimum value. The standard deviation can be considered as an estimate of the horizontal extent of the magma lens. For profile 2 the magma lens would extend about 1 km from the ridge axis. To match the heat flux profile, the depth to the top of the lens would need to increase from about 200 m below the computational domain at the ridge axis to about 600 m below at the point where the liquid fraction reaches zero. Correspondingly, the temperature of the magma would need to decrease from 1,100°C to 1,000°C, the latter slightly below the solidus temperature.

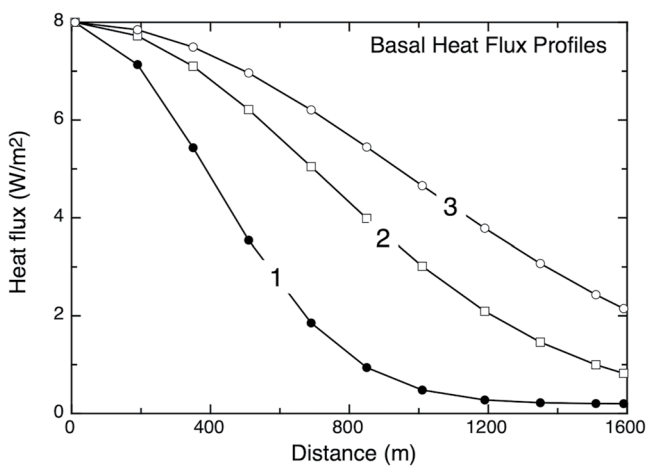

Figure 6. Basal heat flux models using a Gaussian form as a function of distance and the following parameters: Maximum flux 8 W/m^2, minimum flux 0.2 W/m^2, and standard deviation of 555 m (profile 1), 1,000 m (profile 2), and 1,350 m (profile 3). The standard deviation can be thought of as corresponding roughly to half the magma lens width.

3.4. Computational Grid Characteristics

Details of the computational grid are illustrated in Figure 7. The grid is set up to represent a dual permeability system. The fracture spacing is set typically at 2 m, and the grid block size is 20 m. Each grid block in 2 dimensions contains 100 matrix blocks (99% of grid block area) with the accompanying fracture space between them (1% of grid block area). Matrix porosity is 5% and fracture porosity is 50%. Matrix permeability is 10^{-18} m^2 and fracture permeability is 1.5×10^{-14} m^2. The code keeps track of just one chemical composition to represent the matrix blocks in a particular grid block, and one composition to represent the fracture fluid. If we denote the fracture spacing as equal to 2b, the diffusive fluxes between matrix block pore fluid and

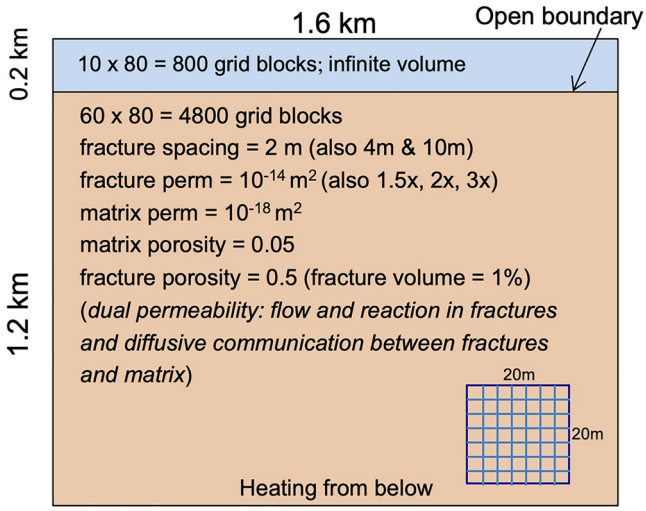

Figure 7. Summary of key features of the computational grid used for the simulations. The inset depicts a single 20 × 20 m grid block subdivided into matrix blocks that are 2 × 2 m in dimension; this depiction has only 49 blocks rather than 100 as in the simulations.

fracture fluid within each grid block are calculated as if the two fluid compositions were separated by a steady-state planar diffusional boundary layer of thickness b/3 (see Text S3 in Supporting Information S1 for further details).

The grid block size was set large enough to allow for relatively rapid simulations so that parameter sensitivity could be tested. In the typical configuration, one simulation takes between 2 days and a week, and is done in segments, each of which can take 1–60 hr using an iMac Pro (2017 version) with 10 cores (20 threads). The stepwise approach is useful because the performance of the code in terms of reaching chemical convergence needs monitoring. The 20 m grid block scale has some limitations, however, because temperature gradients are steep in the higher temperature parts of the simulation, up to about 200°C in 100 m (Figure 8). Consequently, there is spatial averaging within the grid blocks in parts of the simulation, which must be taken into account in assessing the results.

3.5. System Warm-Up

MOR systems are challenging to simulate for chemistry because the temperature varies from the seawater value of 4°C to over 400°C. Mineral-fluid reaction rates vary by a factor of about 10^4 to 10^6 over this temperature range (Text S1 in Supporting Information S1), so in one time step there is much more happening at high temperature than at low temperature. Fluid flow velocities also correlate with temperature and vary by factors of 20–50. As a result of the variability, it isn't possible to start the simulation "cold" with, for example, all of the rock and fluid at the seawater temperature and with realistic mineral-fluid reaction rates. The procedure used here is to start the system with cold seawater in the pores, but with a lower heating rate and with chemical reaction rates between mineral and fluid adjusted to be very slow but non-zero. Chemical reaction rates are regulated through the mineral RSA. The objective is to get fluid flow at steady state before introducing the mineral-fluid reactions at realistic rates. The procedure then is to increase the reaction rates in steps to allow the fluid chemistry to gradually adjust. The typical procedure used to achieve the results reported here is (with some minor variations):

1. Run the simulation for 2000 model years with 50% of the final heating from below and minimal chemical reactions. RSA for primary minerals in both matrix and fractures are set to 10^{-6} cm^2/g and 2×10^{-6} cm^2/g for secondary minerals, which yields chemical reaction rates about 500 times slower than for a more realistic system.
2. Run for an additional 600 model years with the full heating from below and RSA's at 10^{-6} cm^2/g and 2×10^{-6} cm^2/g. This step yields a steady state temperature and flow field with the full heating from below. Less time is needed than for the first phase because the fluid flow velocities are higher with higher heating rates.
3. Run an additional 100 years; RSA's increased to 10^{-5} cm^2/g and 2×10^{-5} cm^2/g
4. Run 100 years; RSA's at 10^{-4} cm^2/g and 2×10^{-4} cm^2/g*
5. Run 100 years; RSA's at 2×10^{-4} cm^2/g and 4×10^{-4} cm^2/g*
6. Run 50 years; RSA's at 3×10^{-4} cm^2/g and 5×10^{-4} cm^2/g*
7. Run 50 years; RSA's at 4×10^{-4} cm^2/g and 8×10^{-4} cm^2/g*
8. Run 100 additional years*

After step 8 the system has been running for 3100 model years, but only 150 years with full reactions, which is long enough to get close to quasi-steady state fluid chemistry (there is no true steady state for chemistry because the rock mineralogy is changing with time). For each of the steps marked with an asterisk, an alternative procedure is to use high RSA's for fracture minerals, up to 50 times higher. As explained below, values of 4×10^{-4} cm^2/g are appropriate for the *matrix* because they give geologically reasonable mineral dissolution rates for plagioclase and CPX at 300°C–350°C, proportionally slower rates at lower temperatures, and are consistent with the largely pervasive matrix alteration that characterizes the rocks at these temperatures (Text S3 in Supporting Information S1 and discussion below). However, the RSA parameter is not necessarily a measure of mineral surface area

15252027, 2022, 12, Downloaded from https://agupubs.onlinelibrary.wiley.com/doi/10.1029/2022GC010524, Wiley Online Library on [21/06/2023]. See the Terms and Conditions (https://onlinelibrary.wiley.com/terms-and-conditions) on Wiley Online Library for rules of use; OA articles are governed by the applicable Creative Commons License

15252027, 2022, 12, Downloaded from https://agupubs.onlinelibrary.wiley.com/doi/10.1029/2022GC010524, Wiley Online Library on [21/06/2023]. See the Terms and Conditions (https://onlinelibrary.wiley.com/terms-and-conditions) on Wiley Online Library for rules of use; OA articles are governed by the applicable Creative Commons License

as much as a way to accommodate the factors that contribute to slowing down reaction rates, including non-linear kinetics as discussed in Daval et al. (2010) and Dixit and Carroll (2007) for clinopyroxene.

For a ridge with a half-spreading rate of 5 cm/yr the rocks move a distance equal to 1 grid block width (20 m) in 400 years. To simulate the alteration over 400 years, the system can be run for an additional 200–300 years with the parameters set as in step 7, although there are issues with this approach when the higher RSA's are used for fractures, as discussed further below.

3.6. Reactive Surface Areas in Fractured Rock Systems

A critical issue in modeling reactive fluid-rock systems is in setting RSA of the minerals, which is difficult to get right in granular materials, and more uncertain in fractured rocks. In the ToughReact code the mineral dissolution and precipitation rates are calculated from an equation of the form:

$$\text{Rate} = k_0 A_r \left[1 - \left(\frac{Q}{K_{eq}}\right)^{\theta}\right]^{\eta} \quad (2)$$

where k_0 (in mol/m^2/s) is a rate "constant" that is dependent on temperature and pH, A_r (m^2/kg) is a specific RSA, and Q/K_{eq} is the saturation state of the fluid for a particular mineral. The exponents θ and η are empirical constants that can be used to fit available experimental data relating reaction rate to saturation index. In our simulations we have both exponents set to unity, which is a linear kinetic formulation, and is typical for reactive transport simulations. However, there are sufficient data available to show that the dissolution of silicates like plagioclase and CPX is not linear, but rather highly non-linear (Daval et al., 2010; Dixit & Carroll, 2007; Hellman et al., 2010). In general, the dissolution rate at SI values of 0.5 down to 0.01, where SI = log(Q/K_{eq}), are far lower than would be calculated using a linear formulation. We account for this difference by using a smaller value for the RSA, A_r. Another approach would be to adjust the rate constants, and use larger RSA (Aradóttir, Sonnenthal, Björnsson, & Jónsson, 2012), but the effect is the same.

In MOR systems there are constraints from observations in ophiolites and ocean crust drill cores that can be used to arrive at geologically reasonable mineral reaction rates. A well-documented example is the alteration observed at Site 504B (Alt et al., 1996), which is relatively young (6 Ma) oceanic crust that originated at a spreading center with a half-spreading rate of about 3–3.5 cm/yr. The spreading rate translates to the newly formed crust at the ridge moving away at the rate of 20 m every 600 years. The high temperature regions of the hydrothermal system extend only about 100–300 m from the axis, so the rocks in the dike section should stay hot (temperatures of 250–350°C where chlorite and amphibole form) for at most 10,000 years and perhaps only 3,000 years. The degree of alteration is variable, but the average rock becomes about 20%–50% converted from primary to secondary minerals in the time this greenschist facies metamorphism is active. The bulk reaction rate, in terms of fraction of rock (or individual mineral) dissolved per year is therefore about 0.00002–0.00005 years^{-1} (20%–50% divided by 10,000 years). If the time is shorter than 10,000 years, the rates can reach higher values of 0.0001–0.0002 years^{-1}. If the time is longer than 10,000 years, the inferred reaction rates are lower.

These observations need to be evaluated with reference to laboratory measured dissolution rate constants of minerals like plagioclase and clinopyroxene. At 300°C the rate constants for pH = 5, typical of the high-T parts of these systems, are about $k_0 = 10^{-6}$ mol/m^2/s or 30 mol/m^2/yr. If this number is multiplied by a RSA in units of m^2/mol, the result is the dissolution time constant in units of y^{-1}. To achieve a dissolution time constant of 0.0001 years^{-1} in a solution that is far from equilibrium requires that the RSA (or A_r) be about 3×10^{-6} m^2/mol, or about 1.2×10^{-5} m^2/kg. This makes the reaction time constant, which is $k_0 A_r \approx 30 * (3 \times 10^{-6}) \approx 0.0001$ years^{-1}. The rates can of course be lower with larger RSA if the solution is close to equilibrium, but if the departure from equilibrium term $|1 - Q/K_{eq}|$ is between 0.1 and 1, the likely values of RSA need to be very small relative to the area of a spherical 1 mm grain, which is close to 1 m^2/kg. The available experimental data for CPX and plagioclase dissolution kinetics, also suggest that reaction rates at small undersaturation can be more than 1,000 times slower than would be calculated for linear kinetics. The available data, however, do not cover near-equilibrium conditions (Q/K_{eq} of 0.5–1) and are not available for temperature greater than about 175°C (Daval et al., 2010; Dixit & Carroll, 2007).

15252027, 2022, 12, Downloaded from https://agupubs.onlinelibrary.wiley.com/doi/10.1029/2022GC010524, Wiley Online Library on [21/06/2023]. See the Terms and Conditions (https://onlinelibrary.wiley.com/terms-and-conditions) on Wiley Online Library for rules of use; OA articles are governed by the applicable Creative Commons License

The RSA values that are used in the simulations for the primary minerals (plagioclase, clinopyroxene, orthopyroxene and olivine) in the *matrix blocks* are typically 4×10^{-5} m^2/kg, which seems extremely low. However, these values yield dissolution time constants for plagioclase and CPX of about 0.0001 $years^{-1}$ at 300°C (faster for olivine), which are in the right range by comparison to natural systems. For reasons that are detailed in Supporting Information S1, these rates are also close to limiting values for the simulations as a consequence of the way that fracture-matrix diffusion is formulated in the code (as used here; Supporting Information S1), and furthermore allow for realistic modeling of pervasive rock alteration.

For the minerals in fractures, higher RSA values are likely, and simulation results are described here that have fracture mineral RSA's higher by a factor of 25 (or 50) relative to those in matrix. However, high RSA's for the fracture minerals introduces other issues. If the RSA's are increased by 50×, for example, then the dissolution timescale for the minerals becomes 100–200 years. This short timescale means that a simulation run for 200–400 years ceases to have meaning because the fracture mineralogy changes too much. In the real system, the large RSA's are likely, but continued fracturing of the rocks probably limits the lifetime of individual fractures (e.g., Ingebritsen et al., 2010). New fractures are continually being generated and it is likely that fluid flow is diverted into the newly formed fractures as older fractures are sealed and abandoned. Thus, for the simulations, the short timescale effect of rapid fracture mineral reaction may be meaningful only for modeling the initial quasi-steady state chemistry and isotopic composition of vent fluids (which is what we have used them for here). For the longer term (200–400 years) evolution of the matrix (which is 99.5% of the rock mass), the slightly different chemistry of the vent fluids generated by increasing the reaction rates of the fracture minerals does not greatly affect the extent of alteration of the matrix (the fluids still have very low Mg, near-zero SO_4, and high Ca, e.g.,). Our modeling over these longer timescales uses fracture mineral RSA's equal to those of the matrix minerals.

4. Simulation Results

4.1. Temperature

Rapid flow of cold seawater through the system results in only a small portion of the computational grid having a steady state temperature above 150°C (Figure 8). With heat flux profile 1 and a uniform permeability of 10^{-14} m^2, the maximum temperature is 380°C and there is a very small part of the grid in the lower left corner where temperatures are above 300°C (Figure 8b). Using heat flux profile 2 and a permeability of 1.5×10^{-14} m^2, the maximum T is 390°C and there is a larger region of high temperature at the base of the grid (Figure 8a). Regardless of the combination of heat flow and permeability, temperatures in excess of 150°C are confined to a small part of the computational grid in the lower left corner and along the left (axis) side where there is strong upwelling. Most of the grid is at $T < 80$°C and more than half is at $T < 20$°C. This pattern does not change with stronger heating from below because stronger heating increases the fluid flux, which moves heat out of the system faster.

Other heat flux—permeability combinations were also investigated, with the constraints that maximum temperature be below 400°C to avoid fluid phase density variations near the critical point of water, but above 375°C (Text S7 in Supporting Information S1). With heating profile 2, only permeability close to that used, 1.5e−14 and a maximum basal heat flux of 8 W/m^2 will satisfy these constraints. With heat flux profile 2 and a maximum heat flux of 10 W/m^2, permeability needs to be raised to 2.5e−14 or 3e−14 m^2, which causes Rayleigh-Taylor plumes to form at the base and non-steady flow. With heat flux profile 1, maximum flux values of 8–12 W/m^2, can be matched with permeabilities of 1 to 1.8e−14. Lower heat fluxes can be matched with lower permeability, but this combination produces quite different fluid evolution that is incompatible with observations. The model results clearly suggest that bulk permeability must be close to 10^{-14} m^2 in the natural systems.

Keeping the maximum temperature below 400°C, and balancing the values for heat input and permeability, is primarily an issue with simulating flow. However, it is also an important aspect of MOR fluid systems (Driesner, 2010; Jupp & Schultz, 2000, 2004). The critical point for H_2O is at 374°C and 220 bar. The base of the system in fast spreading ridges and in our simulations is at a pressure of about 360 bar, which is close enough to the critical pressure that there are rapid density changes that cause the simulations to slow to unusable rates. The rapid decreases in density also accelerate flow, which results in more effective cooling of the fluids. To produce fluid temperatures approaching 400°C requires balanced permeability and heating rate. The permeability we use of 1.5e−14 m^2 is close to the value needed to maximize vent fluid temperature (Driesner, 2010), independent of

10.1029/2022GC010524

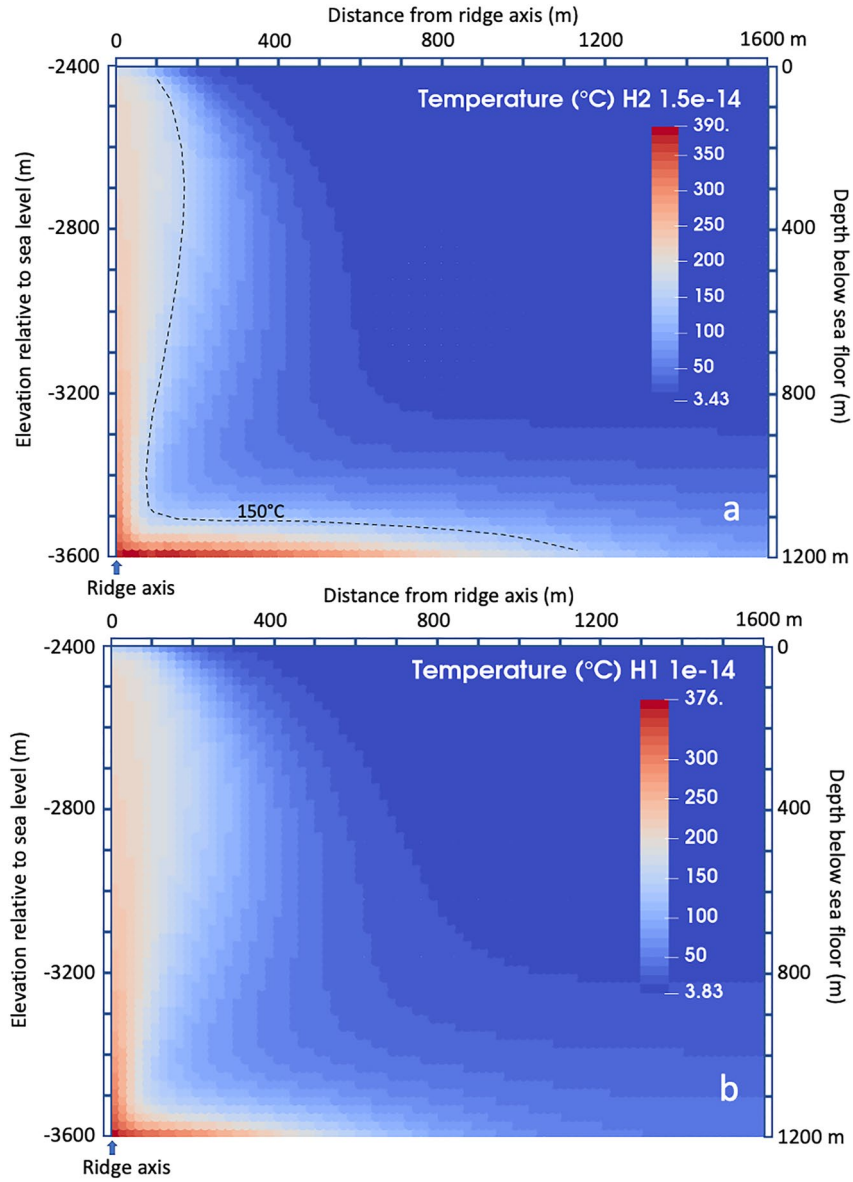

Figure 8. (a) Temperature field for heat generation profile 2 (H2; 8 W/m^2 max) and fracture permeability = 1.5e−14 m^2, also showing the 150°C isotherm. The scales show distance from the ridge axis, depth below the seafloor, and depth below sea level. This basal heating profile and permeability correspond to all other model output discussed in the main manuscript text. Most of the fluid-rock chemistry occurs above 150°C, and hence is confined to the L-shaped region where fluid is flowing sub-horizontally along the base of the system and vertically in the upflow zone near the ridge axis. (b) Temperature field for heat generation profile 1 (H1; 8 W/m^2 max) and fracture permeability = 1.0e−14 m^2. These figures, and similar ones to follow without the scales shown, are color contour maps representing the 1.2 km tall by 1.6 km wide computational domain, with the left side being the position of the ridge axis.

fluid phase salinity. Preliminary simulations we have done indicate that in slow-spreading ridges, where circulation is deeper and the base of the system is at 450–550 bar, fluid density is less sensitive to pressure, flow is less affected by proximity to the critical point, and steady flow is achieved at temperatures well in excess of 400°C.

4.2. Fluid Fluxes and Time Scales

For our model, with the combination of basal heat flux profile 2 and fracture permeability of 1.5×10^{-14} m^2, the maximum fluid flux in the upflow region is about 1.7×10^{-4} kg/m^2/s (Figure 9). A fluid flux of 10^{-4} kg/m^2/s

15252027, 2022, 12, Downloaded from https://agupubs.onlinelibrary.wiley.com/doi/10.1029/2022GC010524, Wiley Online Library on [21/06/2023]. See the Terms and Conditions (https://onlinelibrary.wiley.com/terms-and-conditions) on Wiley Online Library for rules of use; OA articles are governed by the applicable Creative Commons License

15252027, 2022, 12, Downloaded from https://agupubs.onlinelibrary.wiley.com/doi/10.1029/2022GC010524, Wiley Online Library on [21/06/2023]. See the Terms and Conditions (https://onlinelibrary.wiley.com/terms-and-conditions) on Wiley Online Library for rules of use; OA articles are governed by the applicable Creative Commons License

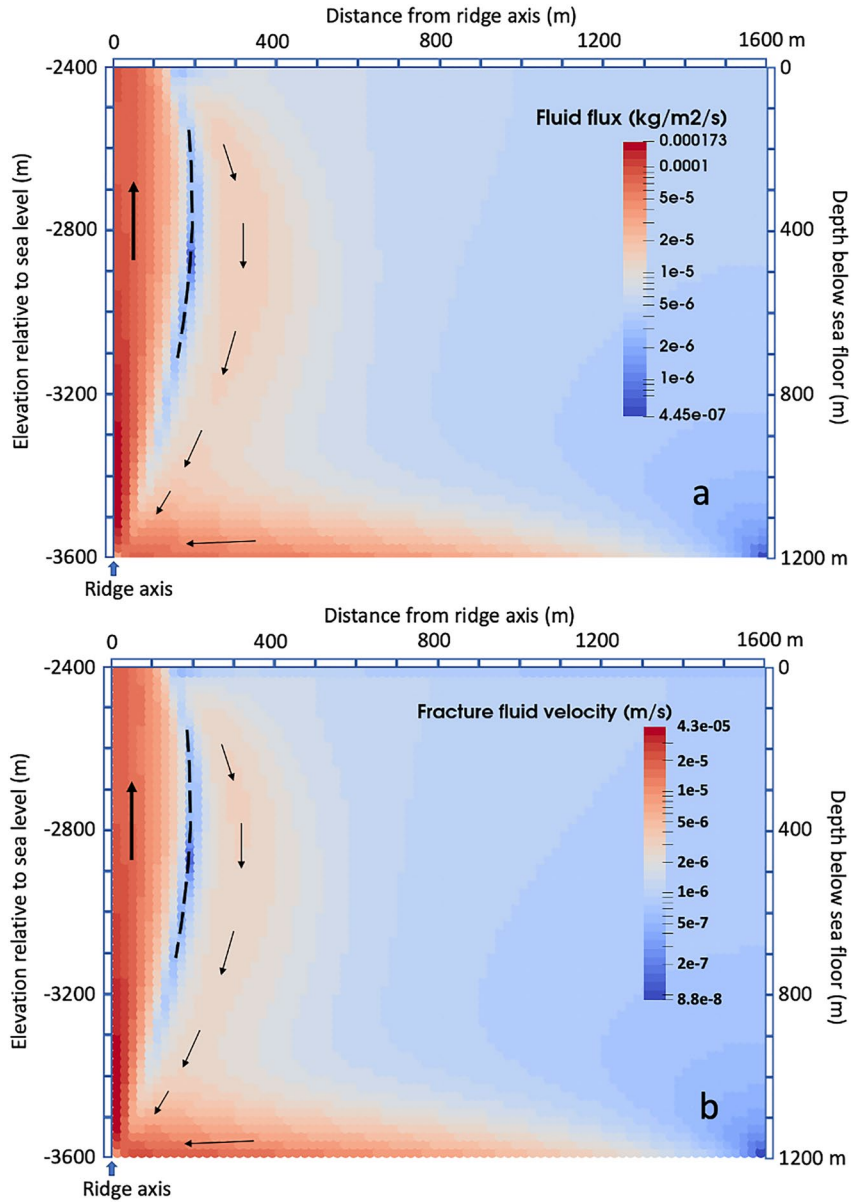

Figure 9. (a) Fluid flux for heat flux profile 2 and permeability of 1.5×10^{-14} m^2. The dashed line is the position of a stagnation zone; all flow to the left of it is upward and all flow to the right is downward. Along the bottom of the grid the flow is mostly horizontal but still has a component of downward flow. The high fluid flux in the lower third of the axial upflow zone occurs because of the relatively large decrease in water density with decreasing pressure at 300°C to 400°C and 350 bar. (b) Fluid velocity in the fractures at high temperature is in the range of 300–1,000 m/yr (1.5×10^{-5} to 3×10^{-5} m/s) and is highest in the lower part of the upflow zone. It can be inferred that fracture fluid travel time from first encountering temperature of 200°C to venting is 2–3 years.

corresponds to a fluid velocity in fractures of 2×10^{-5} m/sec or 630 m/yr. This velocity in turn corresponds to a transit time for fluid from first entry into the high T region to venting of about 2–3 years, which is compatible with observations (Kadko & Butterfield, 1998). The bulk average fluid velocity, accounting for the near-zero flow in matrix is about 60 m/yr. The 2D (1-permeability) porous flow models of Kanzaki (2020), produce fluid velocities of 100's m/yr at shallow levels where permeability is high, but are closer to 10's of meters per year at depth below 100 m.

Varying the heating rate and permeability yields a range of fluid fluxes and maximum temperatures, but the overall pattern of flow and temperature does not change much. The chemical results that are discussed here are

15252027, 2022, 12, Downloaded from https://agupubs.onlinelibrary.wiley.com/doi/10.1029/2022GC010524, Wiley Online Library on [21/06/2023]. See the Terms and Conditions (https://onlinelibrary.wiley.com/terms-and-conditions) on Wiley Online Library for rules of use; OA articles are governed by the applicable Creative Commons License

those that come from simulations using heating profile 2 and uniform fracture permeability of 1.5×10^{-14} m^2. A comparison of results with other permeability values and heating profiles is provided in Text S7 in Supporting Information S1.

An estimate of fluid residence time in the system can be obtained by comparing the total flux of fluid back to the ocean at the top of the upwelling zone to the total mass of fluid in the pore space of the rocks. Accounting for the fact that the simulation is only for one half of the system, the fluid flux for the full model system is about 5.2×10^5 kg/yr per meter of ridge length, similar to values deduced by Lowell et al. (2013) using a simpler flow model. The corresponding mass of fracture fluid is about 1.9×10^7 kg and the total mass of fracture and matrix fluid is 2.1×10^8 kg. Hence the flushing time for fracture fluid is 37 years, and for all fluid it is 407 years. The numbers, however, do not take account of the enhanced downflow and partial recirculation of fluid within about 600 m of the axis. The flushing time for the fracture fluid within 600 m of the spreading axis might be closer to 15 years. The full system fluid flux, when scaled to the global MOR length of 6.5×10^7 m, is 3.4×10^{13} kg/yr, approximately the estimated global average (Elderfield & Schultz, 1996).

It is instructive to compare the calculated fracture fluid residence times to the timescales for diffusive communication between the fractures and matrix. The time required for fracture fluid to traverse one grid block is order (20 m/500 m/yr) $\approx$ 0.04 years. For thermal equilibration, the characteristic time is about 0.03 years assuming a 1-m length scale (from matrix block center to fracture), so thermal equilibration is fast enough that there are only small differences in temperature between matrix and fracture, both for solid and fluid. The chemical diffusion timescale is longer; about 1 year at $T > 300$°C, a few years at 200°C, and about 10 years at 100°C. The chemical diffusion times are much longer than the time it takes fracture fluid to flow the 20-m width of a computational grid block. Consequently, the chemical composition of the matrix fluid is in general different from that of fluid in the fractures, especially in the higher temperature regions, but the larger scale patterns of fluid composition are similar for the matrix and fracture fluids (see Supporting Information S1 for additional discussion).

4.3. Fluid Chemistry

Our reference case simulation uses a starting mineralogy of 56% plagioclase by volume (including 0% or 1% microcline), 22% CPX, 15% OPX, 4% OL, and 3% magnetite, which applies to both matrix and fractures at the start of a simulation. In some simulations, fractures have no olivine and slightly more plagioclase and CPX. As noted above the heat flux - permeability combination yields fluid fluxes close to those of Hasenclever et al. (2014) and a maximum temperature of 390°C. The maximum temperature is an issue because the thermodynamic database used is designed for temperatures less than 300°C. However, of the 4,800 grid blocks in the simulation, 26 are at temperatures higher than 300°C, and 11 are above 350°C. The program extrapolates the data from 300°C where the temperature exceeds that value. The limitations of the thermodynamic database are evident in some aspects of analysis of reaction rates and alteration extent as noted below, but these limitations do not critically affect the performance of the simulated system as a whole. A higher temperature database has recently become available for the latest release of ToughReact (version 4.12), but that database cannot yet accommodate isotopes and has other limitations.

A key result from the simulations is that, because reaction rates reach significant levels only above 150°C (refer to Supporting Information S1), and because the fraction of the grid that is above 150°C is so small (Figure 8), most of the fluid chemical evolution is compressed into a limited region near the base and axis side of the computational grid. This is well illustrated by the SO_4 concentration (Figure 10). Near the base of the grid, the distance over which the SO_4 concentrations change from seawater values of 28 mM to zero is only about 60 m (about three grid blocks). This large gradient precisely locates the region where anhydrite is precipitating fastest. The chemically active regions of the model system are limited in extent and very close to the ridge axis and base of the circulation zone. The downflow regions are below 135°C except close to the base of the grid, so little chemical interaction occurs associated with downflow as, for example, was hypothesized by Bickle and Teagle (1992).

Our expectation is that the simulation using modern seawater composition, if it is close to reproducing the natural systems, should yield high temperature fracture fluids, and ultimately "vent fluid," with near-zero concentrations of Mg and SO_4, Ca concentration in the 20–40 mM range, and Na concentration between 420 and 490 mM, as

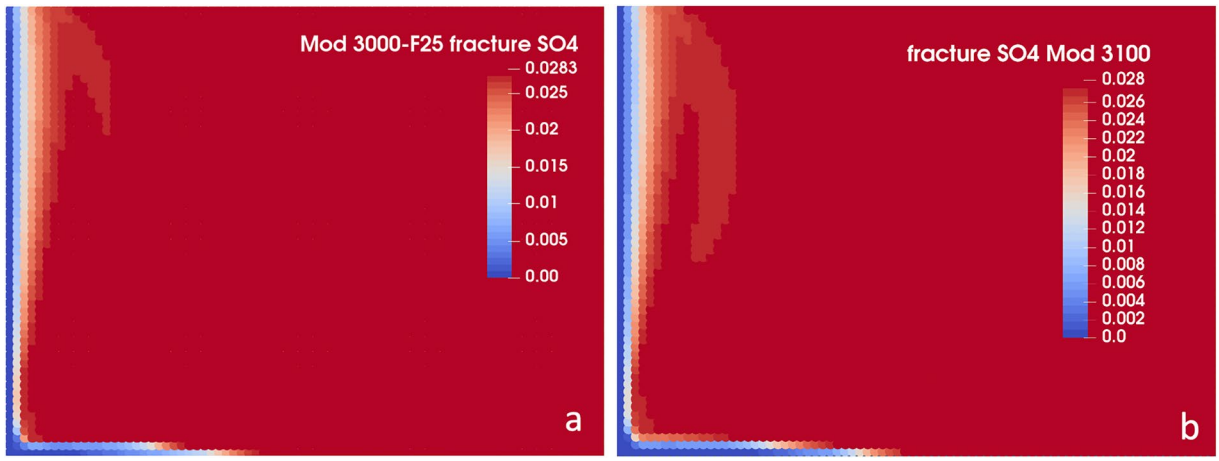

Figure 10. SO_4 concentration in fracture fluids for a simulation with (a) fracture mineral reactive surface areas (RSA) equal to 25× those of the matrix minerals after 150 years at maximum reaction rates, and (b) fracture minerals with RSA equal to those of matrix minerals after 150 years at maximum rates. Venting fluids carrying the most advected heat have near zero SO_4 in both cases.

well as some amount of HS^-. In addition, we expect that the $^{87}Sr/^{86}Sr$ ratio of the fracture fluid/vent fluid is in the range of 0.7040–0.7045 (Bach & Humphris, 1999), and the Sr concentration is in the 100 ± 50 μM range.

The simulations satisfy most of these expectations (Figures 10–12). The color contour plots show concentrations and Sr isotopic compositions within the 1,200 × 1600-m subseafloor part of the computational grid. The upflow zone is along the left (axial) side of the grid (Figure 9) where temperature is highest (Figure 8). The left-most column of grid blocks represents the highest temperature upflow fluid, and the uppermost grid block in that column represents the "vent" fluid composition. These model axial venting fluids are devoid of SO_4 (Figure 10) and contain HS- in mM concentrations. Mg is zero in the deep fluids (Figure 11) and the highest temperature (210°C) venting fluids. Ca concentration reaches values >80 mM in the deep hot zone and vents at 20–40 mM. The reason that the highest temperature venting fluid is not fully shifted from seawater to Mg = 0 is that the downwelling region about 200–400 m from the axis delivers cool, slightly modified seawater (54 mM Mg), deep into the system and this water is entrained into hotter, more chemically evolved fluid near the base of the upwelling zone at a depth of about 1,100 m below the seafloor (see Text S7 in Supporting Information S1). The other upwelling fluids slightly farther from the spreading axis have higher Mg because they never reach high temperature. Those fluids come from circulation around the stagnation zone that separates the upwelling and downwelling regions about 200 m from the axis (Figure 9).

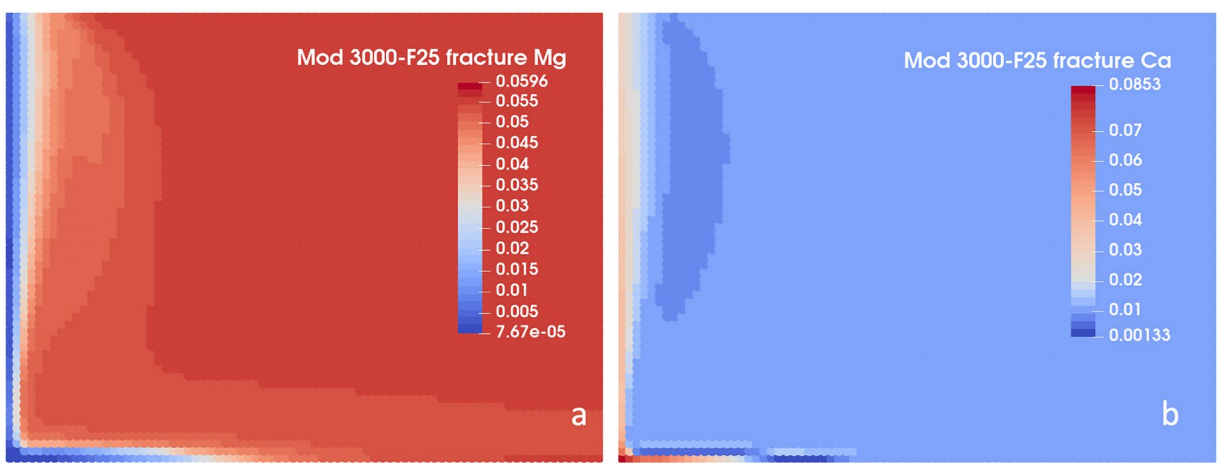

Figure 11. Mg and Ca concentrations in fracture fluids for a model with fracture mineral reactive surface area's 25× those of the matrix minerals. These figures represent a snapshot of fluid chemistry after the system has been running with full reaction rates for about 50–100 years. Venting fluids carrying the most advected heat have virtually zero Mg, and Ca of about 30 mM.

15252027, 2022, 12, Downloaded from https://agupubs.onlinelibrary.wiley.com/doi/10.1029/2022GC010524, Wiley Online Library on [21/06/2023]. See the Terms and Conditions (https://onlinelibrary.wiley.com/terms-and-conditions) on Wiley Online Library for rules of use; OA articles are governed by the applicable Creative Commons License

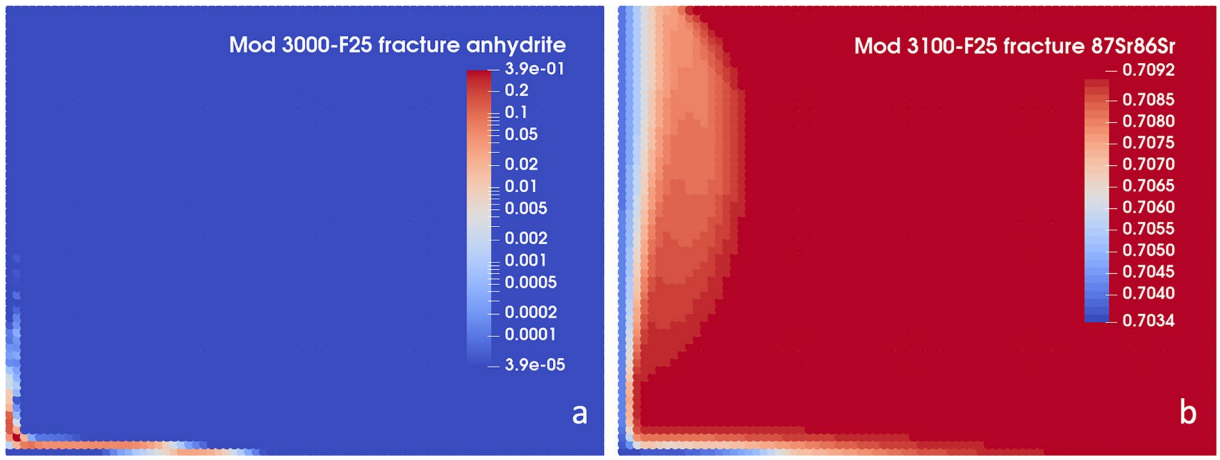

Figure 12. (a) Fracture anhydrite abundance and (b) fluid $^{87}Sr/^{86}Sr$ for a model with fracture mineral reactive surface area's 25× those of the matrix minerals. The amount of anhydrite increases with time, and if fracture clogging were included, the spatial distribution would also change somewhat (discussed in a later section); the $^{87}Sr/^{86}Sr$ changes only slowly with time as the solid mineralogy changes.

The chemistry of downwelling fluid near the ridge axis is influenced by what may be an artifact. Due to the large temperature contrast between upwelling fluids and the ocean bottom at the top of the upwelling region, there is complicated chemistry happening at the interface that modifies the fluid in the top 40 m of the section. One effect is to increase the Na content and thus density. This cooler, denser water flows outward and is incorporated into downwelling fluid just outboard of the stagnation zone. This modified fluid is a component of what is circulated into the roots of the upwelling zone. Circulation around a stagnation zone close to the spreading axis is found in other flow models (Coumou et al., 2009; Hasenclever et al., 2014; Kanzaki, 2020). Rapid recirculation is likely to be prominent along and near the ridge axis on the ocean floor. A mixing zone between high temperature fluids and seawater could occur in natural systems, and the mixed fluid could be recirculated to depth as in the simulations.

The variability in the upflow fluid (vent fluid) chemical composition as a function of distance from the ridge axis is shown in Figure 13. The most evolved fluids are closest to the spreading axis as they have traversed the highest temperature regions for the longest distance. With increasing distance from the axis, the fluids change composition significantly, especially beyond 50 m from the axis. There is also a good correlation of $^{87}Sr/^{86}Sr$ with fluid Mg concentration, and this correlation, with some additional scatter, extends to essentially all fluids in the high-T part of the system (see Supporting Information S1).

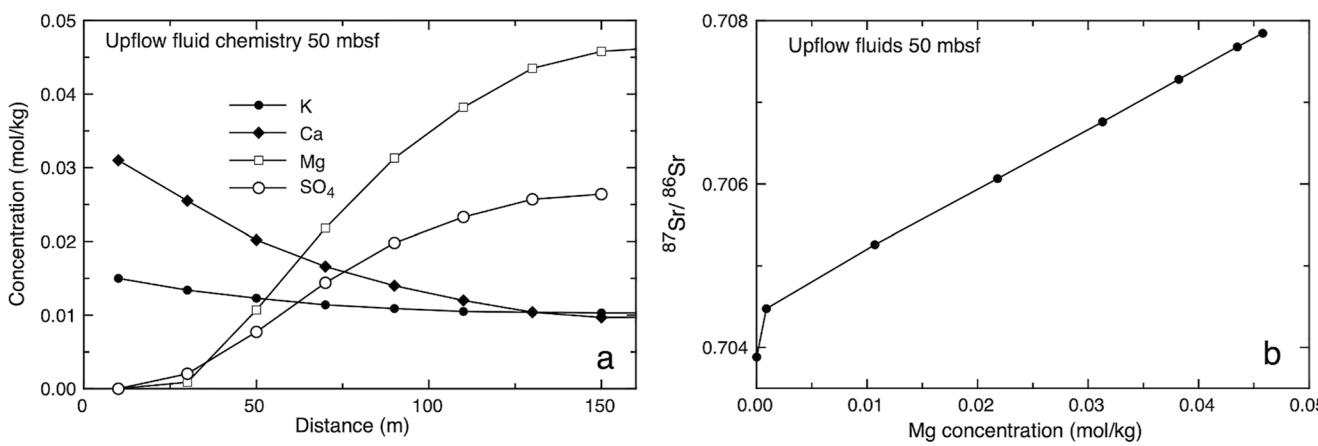

Figure 13. (a) Mg, Ca, and SO_4 profiles of simulated upwelling (vent) fluids within 160 m of the spreading axis and at a depth of 50 m below the seafloor. (b) Relationship between fluid $^{87}Sr/^{86}Sr$ and Mg concentration.

15252027, 2022, 12, Downloaded from https://agupubs.onlinelibrary.wiley.com/doi/10.1029/2022GC010524, Wiley Online Library on [21/06/2023]. See the Terms and Conditions (https://onlinelibrary.wiley.com/terms-and-conditions) on Wiley Online Library for rules of use; OA articles are governed by the applicable Creative Commons License

10.1029/2022GC010524

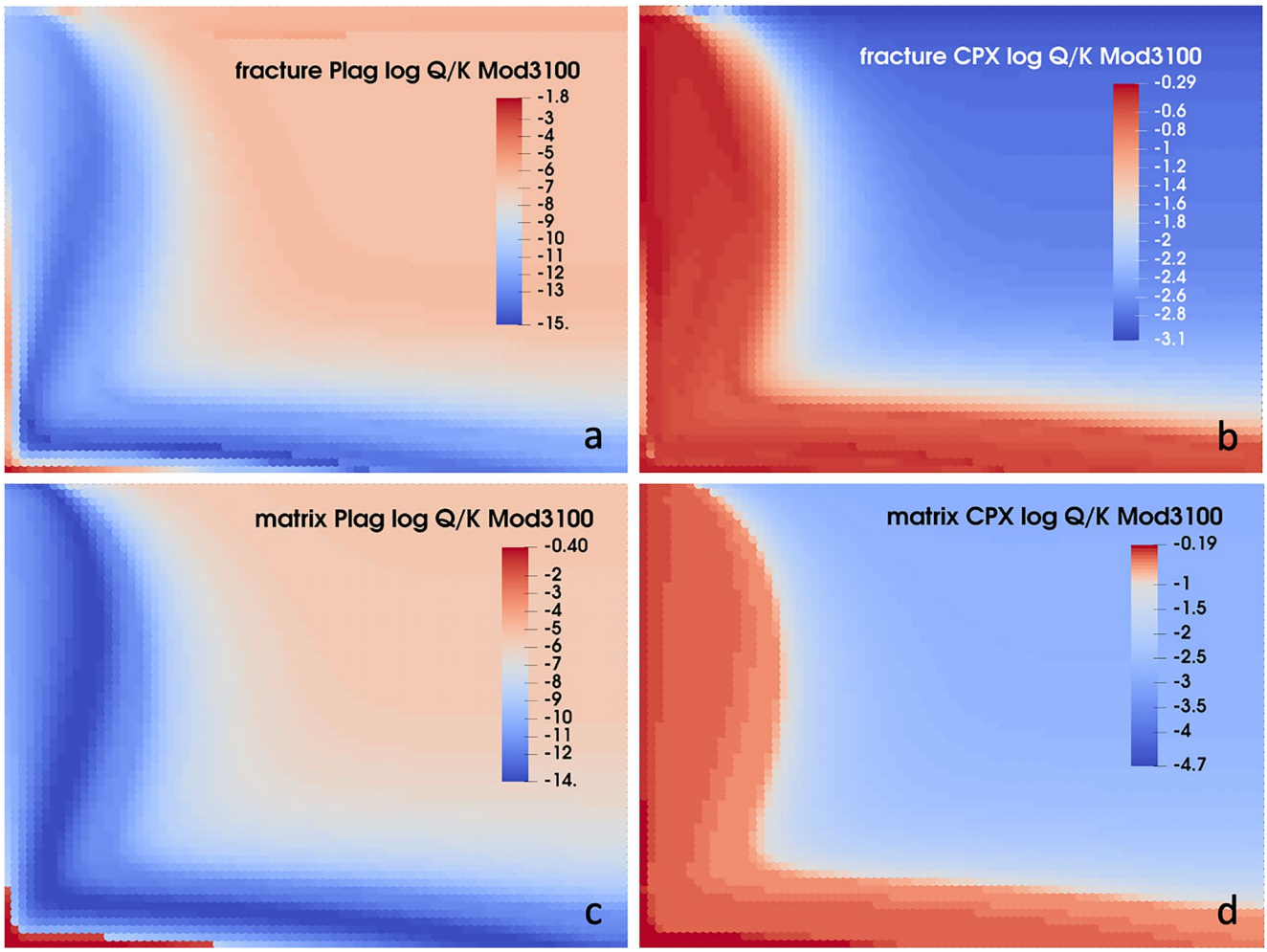

Figure 14. Saturation index ($\log_{10} Q/K_{eq}$) for plagioclase (Plag) and clinopyroxene (CPX) in fracture fluids and matrix fluids after the system has reached a near-steady state and mineral-fluid reactions are set at the maximum values used (model year 3100, step 8, modern seawater). Plagioclase is typically highly undersaturated in fracture fluids, but approaches equilibrium at the highest temperatures in matrix fluids. CPX is closer to equilibrium over a large area of the grid where temperatures are above about 80°C, and approaches equilibrium at temperatures above 200°C.

Within matrix blocks, where porosity is only 5%, the fluid compositions are more extreme than in the fractures because of the low water/rock ratio and slow communication between matrix fluid and fractures. For example, Mg is zero over a larger area of the high temperature region, Ca reaches concentrations greater than 60 mM, and HS-concentrations extend to over 5 mM.

4.4. Saturation State and Dissolution Rates of Primary Minerals

Included in the model output is a snapshot of the fluid saturation state with respect to all of the minerals and the rate at which minerals are dissolving and precipitating. Plotted in Figure 14 are examples for both the matrix fluids and the fracture fluids for plagioclase and CPX. Plagioclase is highly undersaturated almost everywhere in the system except for the highest temperature regions. In fracture fluids, the highest value of plagioclase Q/K_{eq} is $10^{-1.8}$ or about 0.016. The lowest values occur near the 150°C isotherm (see Figure 8b), where anhydrite formation is causing fluid Ca concentration to decrease faster than Ca is added to the fluid from dissolution of plagioclase and CPX. Plagioclase remains undersaturated in the upflow zone. The CPX saturation state of the fluids is much closer to equilibrium everywhere in the system ($Q/K_{eq} \approx 0.5$), and particularly where temperature is above about 80°C. Fluids in the upper part of the upflow zone, which should approximate vent fluid compositions, are quite close to CPX saturation.

15252027, 2022, 12, Downloaded from https://agupubs.onlinelibrary.wiley.com/doi/10.1029/2022GC010524, Wiley Online Library on [21/06/2023]. See the Terms and Conditions (https://onlinelibrary.wiley.com/terms-and-conditions) on Wiley Online Library for rules of use; OA articles are governed by the applicable Creative Commons License

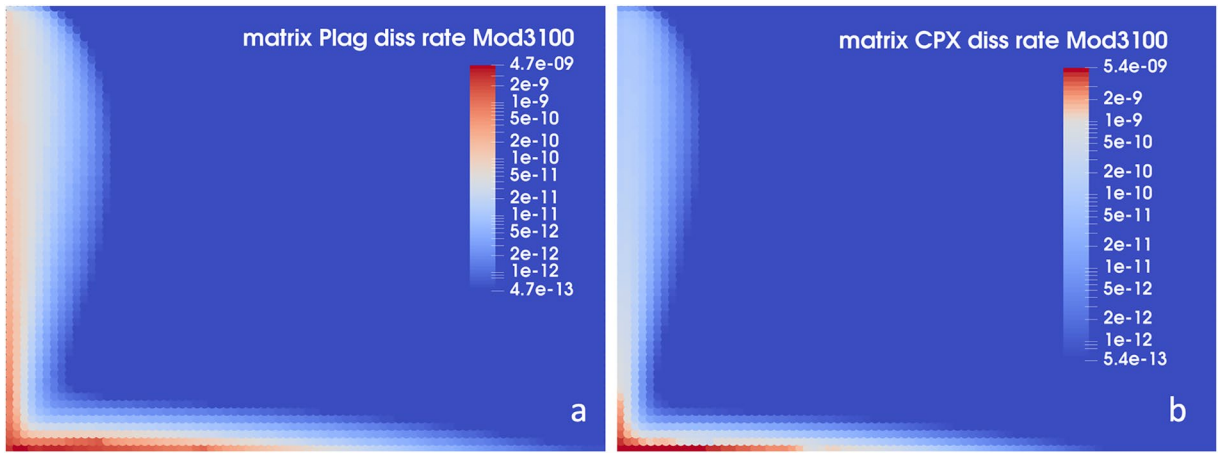

Figure 15. Maps of dissolution rates of (a) plagioclase (Plag) and (b) clinopyroxene (CPX) in matrix in units of moles dissolved per kg fluid per second. Mod3100 refers to model year 3100 (step 8) and modern seawater.

The dissolution rate constants for plagioclase and CPX (Text S1 in Supporting Information S1) were varied to evaluate the sensitivity of the results to those values. CPX values were modified upward and downward while retaining the same temperature dependence. For plagioclase we are using the "albite" kinetic parameters from Palandri and Kharaka (2004), which yield the highest rate constants at high temperature and lower constants at low temperature relative to more calcic feldspar. Use of, for example, the "labradorite" parameters results in fluid evolution being far too slow at high temperature. We experimented with plagioclase k values that are 20× higher than albite at 25°C, but with a lower activation energy so that the 350°C values are close to those of albite. The results with the modified plagioclase kinetics were only slightly different from those shown in Figures 13–18. A more important issue may be the non-linear kinetics of feldspar dissolution (e.g., Oelkers et al., 1994), which would tend to make plagioclase dissolve faster when the saturation index is extremely low.

The corresponding dissolution rates of plagioclase and CPX, unlike the saturation states, are similar (Figure 15). These figures show only the matrix rates because the matrix accounts for 99.5% of the rock mass. Above 150°C, the rates are in the range of 10^{-11} to 5×10^{-9} mol/kgf/s (moles per kilogram fluid per second) and are straightforward functions of temperature (Figure 20; Text S2 in Supporting Information S1). These rates correspond to fractional dissolution rates of 0.15%–75% in 100 years. The highest dissolution rates apply mainly to the region of horizontal flow at the base of the grid and in the lowermost part of the upflow zone. In the middle and upper parts of the upflow zone, which represents most of what will constitute the altered ocean floor after seafloor spreading moves the rocks away from the high temperature zone, the rates are between 1.5% and 15% per 1,000 years.

4.5. Distribution of Secondary Silicate Minerals and Extent of Rock Alteration

The predicted alteration extent and mineralogy from our simulations are important because they are an indication of whether the mineral-fluid reaction rates are realistic, and they can be evaluated by comparison to the results of extensive study of rock alteration in ophiolites and drill cores. Our ability to do this comparison is limited because of the simplicity of our model and the fact that we have not explicitly simulated seafloor spreading. However, we can use the results we have to make an approximate representation of the effects of seafloor spreading.

For example, if the temperature distribution remained unchanged with seafloor spreading (an issue i.e., discussed further below), and the half-spreading rate were 5 cm/yr, the integrated amount of rock alteration that the model produces can be roughly estimated from the output by summing the amount of alteration as a function of horizontal distance from the axis and accounting for the time it takes the rocks to traverse this distance (Figure 17). The amount of alteration referred to here is the fractional volume of secondary minerals, mostly chlorite and amphibole, with significant amounts of albite and epidote at $T \geq 250$°C, and minor montmorillonite. As discussed in

15252027, 2022, 12, Downloaded from https://agupubs.onlinelibrary.wiley.com/doi/10.1029/2022GC010524, Wiley Online Library on [21/06/2023]. See the Terms and Conditions (https://onlinelibrary.wiley.com/terms-and-conditions) on Wiley Online Library for rules of use; OA articles are governed by the applicable Creative Commons License

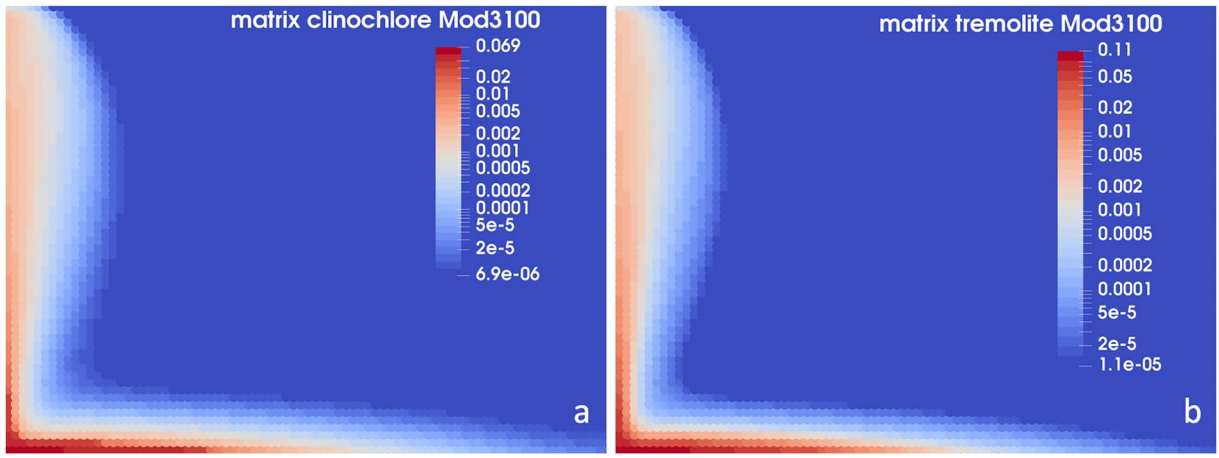

Figure 16. Distribution of secondary clinochlore and tremolite in units of volume percent of solid. The distribution generally reflects temperature (Figure 8a). Note the log scale. Chlorite has Fe/Mg between 0.5 and 1 whereas amphibole has Fe/Mg ≤ 0.1. Mod3100 refers to model year 3100 (step 8) and modern seawater.

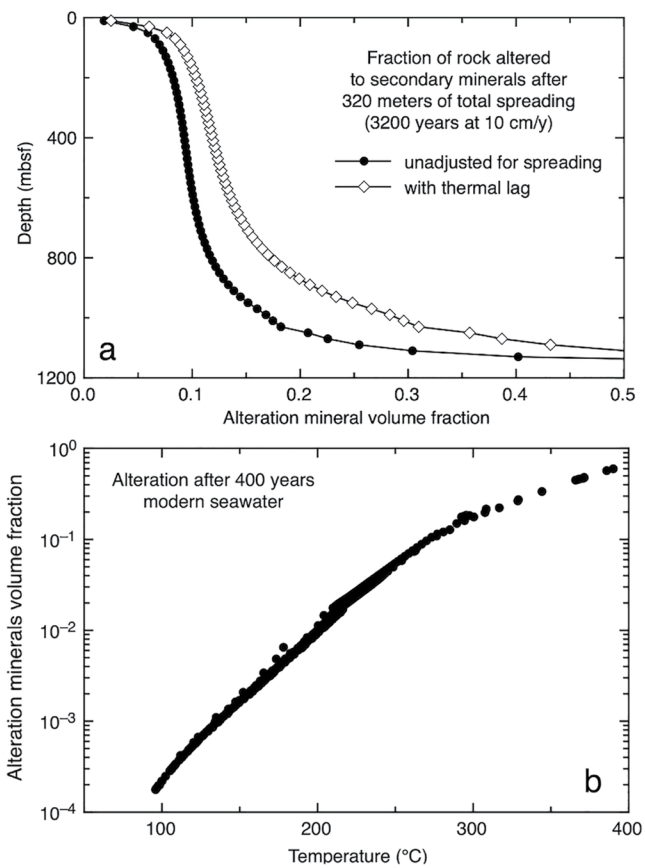

Figure 17. (a) Integrated volume fraction of altered rock versus depth below seafloor after 320 m of full spreading at 10 cm/yr. One curve shows data unadjusted for thermal effects of spreading and the other accounting for a thermal lag of 400 years. (b) Relationship between volume fraction of rock alteration and temperature after 400 years in the simulation. Rocks that have been held at 200°C–300°C reach 1%–20% alteration after 400 years. The degree of alteration is a simple function of temperature and time, and approximately doubles with an increase in temperature of 50°C.

Text S6 in Supporting Information S1, thermal memory effects of seafloor spreading would keep the system at higher temperature longer, increasing the total amount of alteration.

The alteration near the bottom boundary after what would be 3200 years of spreading at 10 cm/yr is large, well over 50%, but is not realistic (Figure 17). If the bottom boundary were sloped downward away from the spreading axis, this alteration would be spread out over some additional vertical interval. Between 1,100 m depth and 400 m depth, which might be representative of the sheeted dike portion of a natural section, the amount of alteration varies from about 45% to 12%, with an average of about 19% using the values adjusted for thermal lag. This amount of alteration is roughly compatible with observations, such as those reported in Alt et al. (1996) at Site 504B as well as Alt et al. (2010) and Heft et al. (2008). Alt et al. (1996) studied oceanic crust produced at a slower spreading ridge where circulation is deeper. For Site 504B samples between 1,550 and 2,100 m depth the fraction altered varies from about 10% to 50% with an average of roughly 30%. Site 1,256, which is in crust from a fast-spreading ridge, has a clear layering where lavas at depths less than 1,000 m have only been exposed to temperatures below 120°C, and a dike section between 1,000 and 1,450 m that has been altered at temperatures of 300°C–600°C. In the higher temperature region, the alteration is highly variable, from 10% to 80%. Similar observations have made at the Pito Deep Rift, where the average extent of alteration of the sheeted dike complex is estimated to be 27% although the range is up to 80% (Heft et al., 2008).

The close correlation between fraction of alteration and temperature in the model is shown in Figure 17b. The data for temperatures above 300°C are suspect due to the database issue, but are likely roughly correct as discussed in a later section. The fraction altered approximately doubles for every 50°C temperature increase. The model alteration mineralogy is summarized in Table 1, which represents data from arbitrary grid elements of different temperature. Olivine disappears after about 14% total alteration. Pyroxenes and plagioclase are reduced gradually as alteration increases. The secondary mineralogy is mostly chlorite and amphibole. Larger amounts of albite and epidote are present at higher temperature. Albite and epidote occur only in the matrix, where W/R ratios are lower, and at temperature above about 250°C. In

15252027, 2022, 12, Downloaded from https://agupubs.onlinelibrary.wiley.com/doi/10.1029/2022GC010524, Wiley Online Library on [21/06/2023]. See the Terms and Conditions (https://onlinelibrary.wiley.com/terms-and-conditions) on Wiley Online Library for rules of use; OA articles are governed by the applicable Creative Commons License

15252027, 2022, 12, Downloaded from https://agupubs.onlinelibrary.wiley.com/doi/10.1029/2022GC010524, Wiley Online Library on [21/06/2023]. See the Terms and Conditions (https://onlinelibrary.wiley.com/terms-and-conditions) on Wiley Online Library for rules of use; OA articles are governed by the applicable Creative Commons License

Table 2
Example Model Alteration Mineralogy (Volume % of Minerals)

Vol.% altered	0	5	10.9	21.7	33.5	59.8
Plagioclase	56	54.8	53.2	47.6	43	25.5
Clinopyroxene	22	18.5	15.5	11.8	6	2
Orthopyroxene	15	15	14.5	12.2	9.6	9.6
Olivine	4	2.8	1.1	0	0	0
Albite				3.2	6.7	19.7
Chlorite		2	4.6	7.5	10.9	15.8
Amphibole		2.9	6.2	8.1	13.4	14.8
Epidote				2.1	3.5	9.5
Magnetite	3	3	3	3	3	3
Temperature		249	276	308	344	390

simulations with enhanced reaction rates in fractures, small amounts of epidote form in fractures in the upflow zone (Text S7 in Supporting Information S1).

4.5.1. Rock Alteration and Seafloor Spreading

It is important to recognize that our model starts with fresh rock in the entire subseafloor part of the computational grid. In reality, all of the rock other than that close to the ridge axis has already been altered by the near-ridge processes and would contain a substantial fraction of secondary minerals, little if any olivine, and smaller volume fractions of plagioclase and pyroxene. The secondary minerals also have $^{87}Sr/^{86}Sr$ that is different from the fresh rock. The model as we have it constructed cannot accurately account for this alteration; it would require implementation of seafloor spreading to capture the continual supply of fresh rock at the ridge axis, the non-uniform distribution of alteration with depth, and the gradual increase in alteration as the rocks move away from the axis. We have, however, explored the effect of the entire grid being composed of altered rock with a mineralogy corresponding to about 15% alteration (Table 2), the rough column average weighted toward the deeper part of the section where most of chemical interaction occurs (Figure 17a). The results, some of which are provided in Text S7 in Supporting Information S1, are somewhat different in that the fluids are more depleted in Mg and somewhat higher in Ca. Other aspects of the simulations are broadly similar to those shown above for the model starting with fresh rock. Nevertheless, it must be an important longer-term objective to implement seafloor spreading in the simulations.

4.5.2. Secondary Mineral Kinetics

The appropriate RSA for secondary minerals are uncertain, but simulations have been run with a variety of values. The typical values used are twice those of the primary minerals, but in other cases higher values up to 10 or 20 times those of the primary minerals were used. A check on whether the secondary mineral RSA's are too small is the saturation indices of chlorite and tremolite (Figure 18). For chlorite, saturation index is very high at temperatures below 100°C (and in seawater), but in the main alteration zone where temperature is above 150°C chlorite values are between 0 and 2. Tremolite is highly oversaturated at about 100°C but has $\log(Q/K_{eq}) \leq 1$ at $T > 200$°C.

In the simulation results shown here, the RSA of albite is set to relatively large values to enhance the rate of formation. The higher albite values seem to be required to balance the release of Na from plagioclase dissolution so that fluid Na concentrations don't get too high. For albite, compositions of An_0, An_{10}, and An_{20} are included in some simulations. Most of the simulated secondary feldspar is An_0 (80%) and An_{10} (20%) which is in reasonable

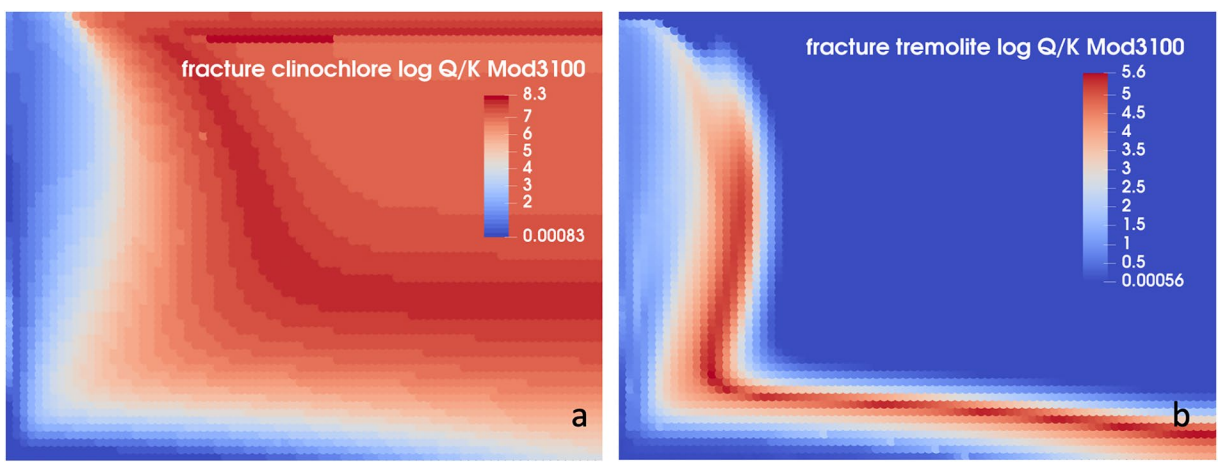

Figure 18. Saturation indices of secondary mineral components (a) clinochlore and (b) tremolite. The saturation index for anhydrite (not shown) is less than 0.5 everywhere. Mod3100 refers to model year 3100 (step 8) and modern seawater.

15252027, 2022, 12, Downloaded from https://agupubs.onlinelibrary.wiley.com/doi/10.1029/2022GC010524, Wiley Online Library on [21/06/2023]. See the Terms and Conditions (https://onlinelibrary.wiley.com/terms-and-conditions) on Wiley Online Library for rules of use; OA articles are governed by the applicable Creative Commons License

agreement with observations at Sites 504B and 1,256 (Alt et al., 1996, 2010). Many of the simulations include only An_0, but the amounts of total low-Ca plagioclase formed are still qualitatively similar.

4.5.3. Anhydrite Formation and Rock Permeability

It has been hypothesized that the precipitation of anhydrite in fractures tends to seal fractures and that this might be a major factor in determining the structure of hydrothermal systems (e.g., Lowell, 2003; Sleep, 1991). This aspect of the system has not been modeled completely here. For the model results shown above, permeability is NOT a function of porosity. Running the models without a porosity-permeability feedback is instructive, however, in that porosity evolution can be evaluated without flow changes causing difficulty in the simulation. A porosity-permeability feedback can then be added to determine its effects. An example run with no feedback (Figure 19a) is juxtaposed with the anhydrite distribution (Figure 19b). In general fracture porosity decreases significantly only where anhydrite is forming. Everywhere else, fracture porosity increases slightly or remains close to the starting value of 0.50.

With no feedback, anhydrite accumulation is concentrated in a few grid blocks and is associated with an 80%–95% drop in porosity in those grid blocks. When a porosity-permeability feedback is included the distribution of anhydrite is somewhat less concentrated and the total porosity reduction is smaller (Figures 19c and 19d). These differences appear subtle, but they can have a significant impact on flow. In the 2D simulation, anhydrite formation produces a lower-permeability layer about 30 m above the base of the computational grid. This layer acts as insulation and causes the temperature in the underlying higher permeability layer to increase, ultimately producing oscillatory behavior where temperature, flow and fluid chemistry undergo oscillations with a period of 70–80 years (Text S8 in Supporting Information S1). The oscillatory temperature variations at the base of the

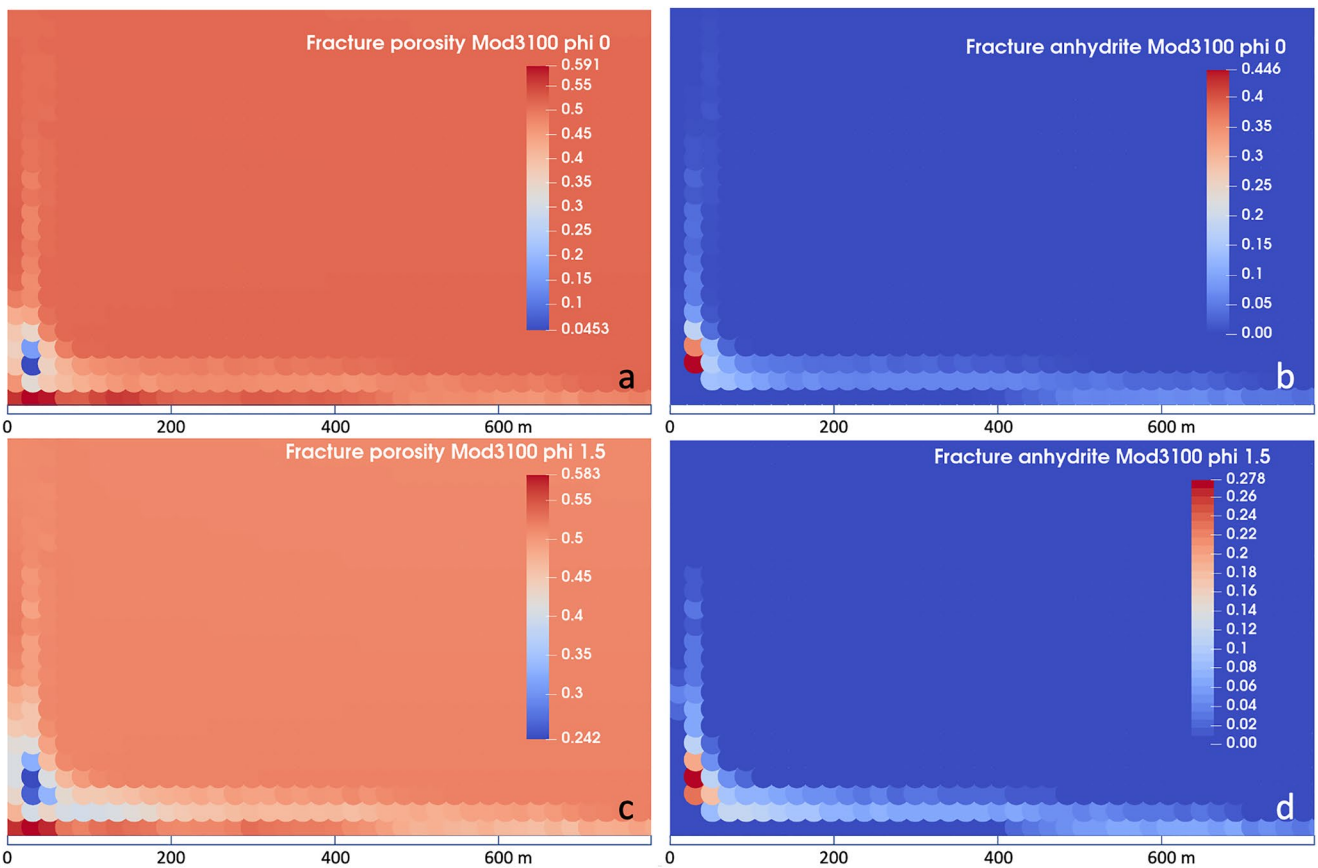

Figure 19. Effects of adding weak porosity-permeability feedback. Figures are 2× expansions of the high temperature corner of the computational grid and show results with permeability scaled as $(\phi/\phi_0)^0$ (a, b) and $(\phi/\phi_0)^{1.5}$ (c, d) denoted in the titles as "phi 0" and "phi 1.5." Vertical scale is the same as horizontal. With the porosity-permeability feedback, porosity decreases less in any one grid block, and anhydrite is distributed more evenly over more grid blocks, but anhydrite formation is still restricted to a small region of the grid. Mod3100 refers to 3100 years model time (step 8) and modern seawater.

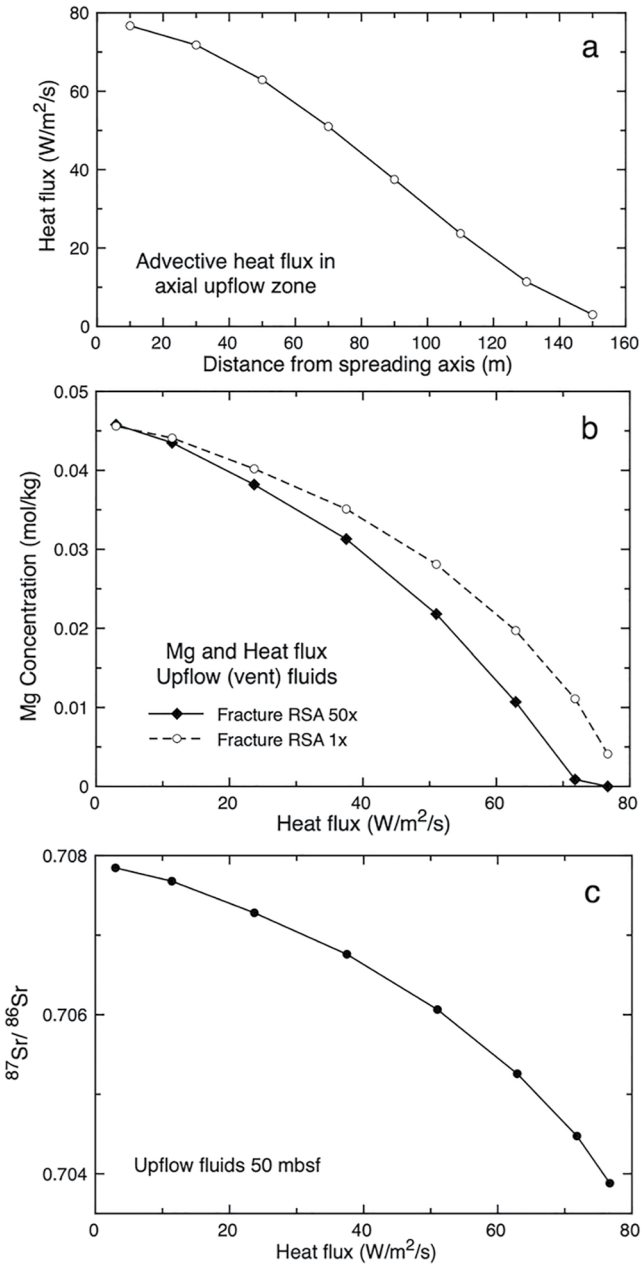

Figure 20. (a) Advective heat flux versus distance from spreading axis at 50 mbsf. (b) Heat flux versus fluid Mg concentration in model vent fluids. With increasing fracture mineral reaction rates, fluid Mg decreases, but significant heat is still carried by higher-Mg fluids (c) fluid $^{87}Sr/^{86}Sr$ versus heat flux for the case with increased reaction rates in fractures. All figures are for modern seawater and a model time of 3100 years.

system are large, ±40°C and are associated with oscillations in fluid chemistry and $^{87}Sr/^{86}Sr$.

Porosity-permeability feedback is important for modeling the effects on flow that could generate highly non-uniform flow fields, especially in 3D. However, for our purposes it may be of limited value. The appropriate feedback formulation is uncertain. We have experimented only with relatively weak dependence of permeability on porosity. As discussed previously, the likely case for MOR systems is that new fractures are being continuously generated. The vent fluid chemistry observed in nature may *require* the continual generation of new fresh fractures (next section), so having the model fractures seal with time would not correspond to the actual evolution of the fluid flow or fluid chemistry. The constraints we have for vent fluids–flux, temperature, and chemistry—can be interpreted in terms of a steady state system with a particular range of permeability and heating rate. This "steady state" can be produced by a continually operating process of fracture sealing and fracture generation. For our purposes, we seek the time-averaged properties, and several studies have concluded that the steady state would need to be characterized with a permeability near 10^{-14} m^2. In the 2D case that we have simulated, the formation of an insulating layer leads to pulsed behavior as the fluid in the lower layer heats above 400°C, expands, and the lower density fluid causes temporary acceleration of the flow, which then cools the lower layer until continued heat input reheats it and another cycle begins. Oscillatory temperature variations are closely tracked by mineral-fluid reaction rates, which means that matrix fluid chemistry follows closely in time, and fracture fluid chemistry responds slightly differently but in a similar fashion and with a similar cycle time. Elsewhere in the system, the temperature fluctuations and fluid chemistry variations are smaller (Text S8 in Supporting Information S1). The integrated rock alteration does not change significantly, and the effect of the temperature oscillations is to make the temperature distribution at the base of the upwelling zone more uniform, but with a similar average temperature. Our conclusion is that accounting for the effects of anhydrite formation on flow does not change the overall character of our 2D model system in terms of fluid fluxes, average fluid chemistry, and alteration mineralogy and extent. Much more work would need to be done to explore the effects of anhydrite formation on flow, and ultimately this would need to be addressed with 3D simulations.

4.6. Flow, Reaction, and Fluid Chemistry

In the simulations, the generation of vent fluids with near-zero Mg (e.g., Figure 14) is dependent on fluid-rock reaction in fractures. Unless the fracture minerals are reacting fast, the venting fluids tend to have slightly higher Mg of a few mM. However, deep fracture fluids along the base of the system have Mg ≈ 0 regardless of the fracture mineral reaction rates, and high temperature matrix fluids, which constitute 90% of the fluid volume in the high-T regions, have near-zero Mg in both the basal and upflow zones.

One reason that simulated vent fluids have non-zero Mg is the recirculation of seawater to the base of the upwelling zone and entrainment of this high-Mg fluid into the upwelling fluids. This entrainment also tends to cool the fluids; cooling of order 50°C is commensurate with addition of enough Mg to increase the high-T fluid concentration from zero to a few mM (Supporting Information S1). Another issue is with regard to spatial averaging within the 20-m grid blocks. The chemical and thermal gradients in the high temperature parts of the system are steep, and there may be difficulty in producing near-zero Mg fluid because of this.

15252027, 2022, 12, Downloaded from https://agupubs.onlinelibrary.wiley.com/doi/10.1029/2022GC010524, Wiley Online Library on [21/06/2023]. See the Terms and Conditions (https://onlinelibrary.wiley.com/terms-and-conditions) on Wiley Online Library for rules of use; OA articles are governed by the applicable Creative Commons License

15252027, 2022, 12, Downloaded from https://agupubs.onlinelibrary.wiley.com/doi/10.1029/2022GC010524, Wiley Online Library on [21/06/2023]. See the Terms and Conditions (https://onlinelibrary.wiley.com/terms-and-conditions) on Wiley Online Library for rules of use; OA articles are governed by the applicable Creative Commons License

4.6.1. Damköhler Numbers

The reduction of fluid Mg concentration during fluid-rock reaction, which is due to the rapid formation of secondary, Mg-rich, aluminosilicate minerals, is a measure of the competing effects of fluid flow velocity and reaction rate, and can be represented with a Domköhler number. However, estimating this number is complicated because the concentration of Mg in the fluid flowing in fractures is affected by reaction with the minerals lining the fractures as well by diffusive exchange with the matrix pore fluid. The fracture fluids with lowest Mg are those flowing sub-horizontally along the bottom of the system prior to entering the upflow zone (Figure 11). For these horizontal-flowing fluids, temperature increases from 150°C to 350°C, over a distance of about 400 m. Typical fluid velocity at these temperatures is 500 m/yr and fluid flux is 3,000 kg/m^2/yr or 3 m/yr. As noted in Text S2 in Supporting Information S1, at high T the chemical fluxes between matrix and fractures are approximately diffusion limited, and the applicable Damköhler number, if the fracture fluid chemistry were only affected by diffusive exchange with matrix fluid, is:

$$N_{\mathrm{D}} = \frac{3D\tau\phi_{\mathrm{m}}A_{\mathrm{fm}}\Delta C}{bqC_{\mathrm{f}}} \tag{3}$$

Using parameter values from the simulations, $D = 0.35$ m^2/yr, $\tau = 0.2$, $b = 1$ m, $q = 3$ m/yr, $\Delta C/C_{\mathrm{f}} \approx 1$ (the maximum), and $A_{\mathrm{fm}} = 2$, gives $N_{\mathrm{D}} = 0.007$. This result suggests that even at relatively high temperature, the fracture fluids are strongly influenced by transport. The parameter A_{fm} is the fracture-matrix surface area factor, which is 2 m^2/m^2 (800 m^2 for each 20 × 20 m grid block). The advective length scale (L_{adv}) for adjustment of the fracture fluid concentration C_{f} is about 170 m at $T \approx 350$°C. At lower temperature down to 150°C the Damköhler number is only slightly different because reaction rates and fluid fluxes change in parallel.

The above analysis is consistent with the model output. For fluids that are heating up before reaching the upflow zone, the Mg and SO_4 concentrations adjust rapidly enough to reach zero above 300°C. However, due to the influx of lower temperature, and chemically less evolved water at the base of the upflow zone, the venting fluids have low but non-zero concentrations of Mg. The SO_4 concentration is not as affected because the cooler fluids are stripped of SO_4 as they heat up above 150°C due to the high fluid Ca concentrations.

One feature of the model output that was unexpected is the region of low fracture fluid Ca concentration at depth of about 100–600 m in the neighborhood of the stagnation zone separating the upflow zone from the proximal downflow zone (Figure 11). The low Ca concentration is presumably due to anhydrite formation removing Ca as the fluids move into and up through the lower temperature fringe of the upflow zone, get heated above 150°C, and then circulate back down on the other side of the stagnation zone. Repeated cycling of fluid around the stagnation zone can potentially strip out fluid Ca without greatly affecting SO_4 concentration. The temperature of the stagnation zone for our simulation parameters is well defined at about 135°C, upwelling fluids are hotter and downwelling fluids are cooler. The low Ca concentrations in fracture fluids are associated with relatively small amounts of anhydrite forming in fractures and matrix in the upflow zone.

5. Vent Fluid Composition and Heat Flux

A potentially useful aspect of the model output is that it provides compositions of "vent" fluids and the relationship of those compositions to advective heat flux (Figure 20). For this comparison we use the fluid and heat flux values that apply to the grid blocks located 50 m below the ocean floor and within 150 m of the spreading axis. Virtually 100% of the magmatic heat entering the system from below is advected to the ocean within 150 m of the spreading axis in the simulated system (Figure 20a; see also Kanzaki, 2020). A substantial fraction of the heat is carried in intermediate-temperature fluids that have not evolved to zero Mg and SO_4 (Figure 20b). The average Mg concentration of venting, heat transporting fluids varies depending on the reaction rates of minerals in fractures, and is about 10 mM for the faster reacting case. Higher reaction rates might further lower the heat flux-weighted vent fluid average Mg concentration, suggesting that advected heat, advected fluid, and Mg removal from seawater are close to proportional as is generally assumed for ridge-crest hydrothermal systems, although it has been recognized that correlations between advected heat and Mg removal fluxes extend continuously to low temperature (Mottl & Wheat, 1994). In the model, the fast reaction in fractures quickly reduces the effects of the fracture mineral dissolution on fluid chemistry on timescales of decades, but in the real system, continued generation of

15252027, 2022, 12, Downloaded from https://agupubs.onlinelibrary.wiley.com/doi/10.1029/2022GC010524, Wiley Online Library on [21/06/2023]. See the Terms and Conditions (https://onlinelibrary.wiley.com/terms-and-conditions) on Wiley Online Library for rules of use; OA articles are governed by the applicable Creative Commons License

Table 3
Seawater Compositions

Component	Modern	95 Ma	1,800 Ma	3,800 Ma
Na	10,780	9,600	8,700	2,500
Ca	412	1,400	2,600	8,400
Mg	1,315	740	700	350
Fe	0	0	1.00E−04	1.00E−04
Sr	8	40	80	400
Al	1.00E−06	1.00E−06	1.00E−06	1.00E−06
SiO_2	1.00E−06	6	6	6
Cl	Chg Bal	Chg Bal	Chg Bal	Chg Bal
SO_4	2,700	960	100	10
Molar Ca/SO_4	0.35	3.5	30	30
$^{87}Sr/^{86}Sr$	0.70918	0.7074	0.7048	0.7020
pH	7.5	7	6.8	6.6
T	4	15	20	40
Rock $^{87}Sr/^{86}Sr$	0.7028	0.7028	0.7012[a]	0.6995[b]

Note. Concentrations in ppm.
[a]Ratio that would correspond to $\varepsilon_{Nd} = +5$ using the modern oceanic basalt correlation line. [b]This ratio is not well constrained, but is plausible for simple Earth evolution models.

new fractures and re-routing of fluid into newly formed fractures could maintain low fluid Mg concentrations in higher temperature vent fluids.

6. Effects of Changing Seawater Composition

As an example of the possible uses of MOR simulations for studying the behavior of seafloor hydrothermal systems under changing boundary conditions, we have attempted to use the model, as calibrated for modern seawater, to evaluate the effects of changing seawater composition. Simulations identical to those for modern systems were done using hypothetical Cretaceous (95 Ma), Proterozoic (1,800 Ma), and Archean (3,800 Ma) seawater. The parameters used for heat flux, permeability, fracture spacing, etc. were kept the same and the only change was the seawater composition. The logic is to first create a model system that produces a reasonable facsimile to a modern system in terms of vent fluid compositions and rock alteration and then to perturb it only by changing the seawater composition. The Cretaceous seawater composition for Ca, Mg, and SO_4, is based on the work of Lowenstein et al. (2001, 2014) and Horita et al. (2002) and the Proterozoic and Archean compositions are based on the models of Halevy and Bachan (2017). Cretaceous seawater Sr concentration is based on the analysis of Coogan (2009). Proterozoic and Archean seawater Sr is speculative, but follows the trend of higher Sr/Ca being associated with higher seawater Ca concentration. A summary of key components of the four seawater compositions is provided in Table 3. The main difference between the paleo-seawater compositions and modern seawater, is that Ca and Sr are substantially higher, and Na, Mg and SO_4 are lower. The paleo-seawater compositions also have lower pH and higher deep-water temperature.

The overall temperature, pH, major ion concentrations, and alteration patterns that are produced using paleoseawater compositions (Text S7 in Supporting Information S1) are difficult to distinguish from those in Figures 14–16 and Figures 18–21, except for the proportion of anhydrite, which reflects the lower seawater sulfate concentrations. The vent fluid compositions are different mainly in Ca, Sr and $^{87}Sr/^{86}Sr$ (Figure 21), and for the Archean case, Na.

The data from Cretaceous ophiolites indicates that the altered rocks of that age are more strongly affected by exchange with seawater Sr than are ocean floor rocks of age <6 Ma (Figure 22). The bulk Sr isotopic composition of the rocks is not fully represented in our simulations, but we can compare the isotopic composition of the primary Sr-bearing secondary mineral tremolite (Figure 23). It is likely that the other major Sr bearing secondary phase, low Ca plagioclase, would have a similar isotopic composition. The simulations show that the secondary mineralogy for the paleo-seawater cases will be much more strongly shifted toward the seawater Sr isotopic composition for the same amount of alteration.

The late Cenozoic drill core rocks are typically shifted only about 5%–10% toward the seawater $^{87}Sr/^{86}Sr$ value. Based on the modern curve in Figure 23, that shift could be accounted for with 15%–35% alteration, assuming that the Sr shift were proportional to alteration fraction. For the Oman ophiolite, where the observed Sr isotope shift is 20%–40% toward the seawater value, the 95 Ma curve would suggest that 30%–60% alteration is necessary. For Troodos, the shift is highly variable, but reaches 60% seawater component, and averages about 30%–40%. This implication is that the altered rock fraction for Troodos can approach 100%, although the average would be about 50%.

The difference in seawater Ca and Sr for the Cretaceous model, and probably also to a lesser degree the lower SO_4, results in the rocks being more shifted in $^{87}Sr/^{86}Sr$ toward the seawater value as previously noted by others (Bickle & Teagle, 1992; Coogan, 2009). However, the data from the Cretaceous ophiolites seem also to require that the rocks have experienced a larger amount of alteration, which in turn means they were exposed to high temperatures for a longer period of time. This difference was also discussed by Bickle and Teagle (1992). For the model presented here, longer times would be associated mainly with slower spreading. Troodos, which has generally

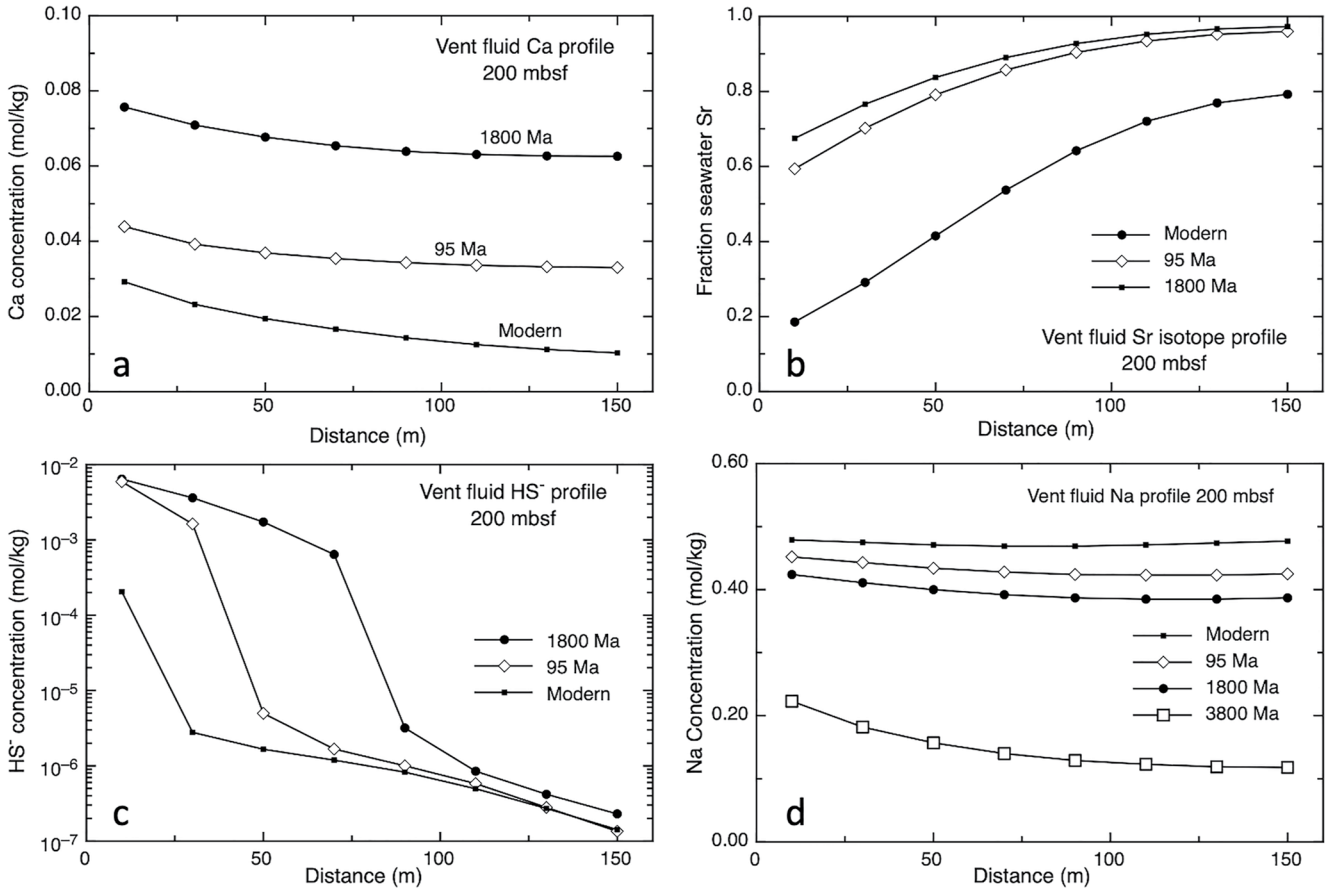

Figure 21. Comparison of "vent" fluid chemistry in a transect of upwelling fluids 200 m below the seafloor for model seafloor hydrothermal systems with different seawater chemistry and Sr isotopic composition. (a) Ca concentration versus distance from the spreading axis. (b) Sr isotopes expressed as the fraction of seawater Sr. (c) HS-concentration, and (d) Na concentration, which includes a model for Archean seawater. For the Archean case the venting fluid is markedly enriched in Na relative to seawater. Because the paleo-seawater compositions are high in Ca, there is relatively less enrichment in Ca in the venting fluids.

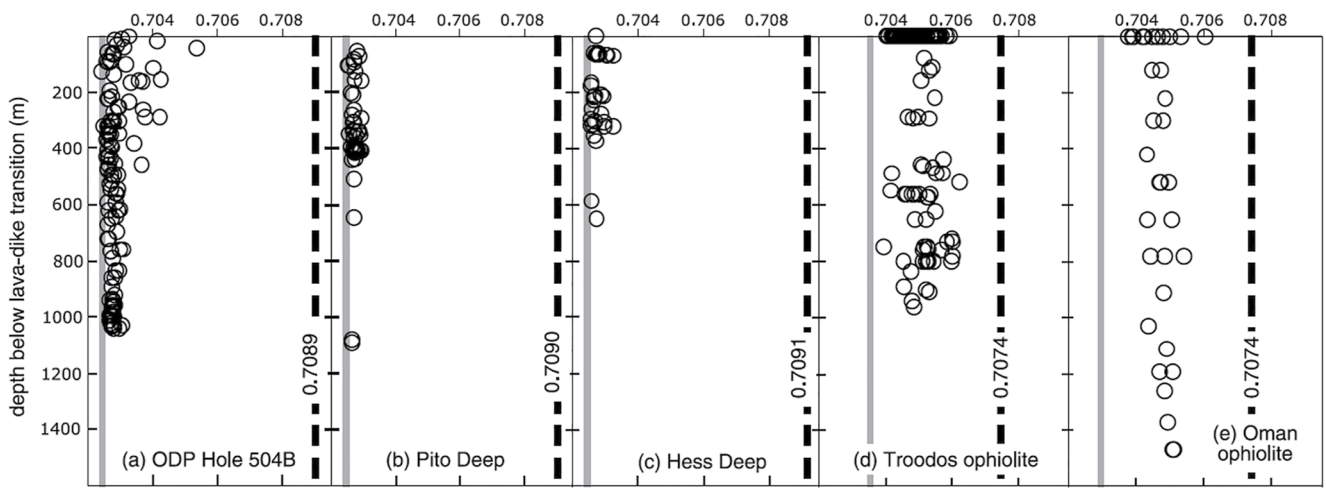

Figure 22. Contrasting Sr isotope shifts in young (<6 Ma) oceanic crust and Cretaceous ophiolites that formed at a time when seawater had high (Ca + Sr)/SO_4 (from Coogan, 2009), as well as higher temperature and lower pH. The gray vertical lines are the fresh rock isotopic compositions and the heavy dashed lines are the contemporaneous seawater compositions.

15252027, 2022, 12, Downloaded from https://agupubs.onlinelibrary.wiley.com/doi/10.1029/2022GC010524, Wiley Online Library on [21/06/2023]. See the Terms and Conditions (https://onlinelibrary.wiley.com/terms-and-conditions) on Wiley Online Library for rules of use; OA articles are governed by the applicable Creative Commons License

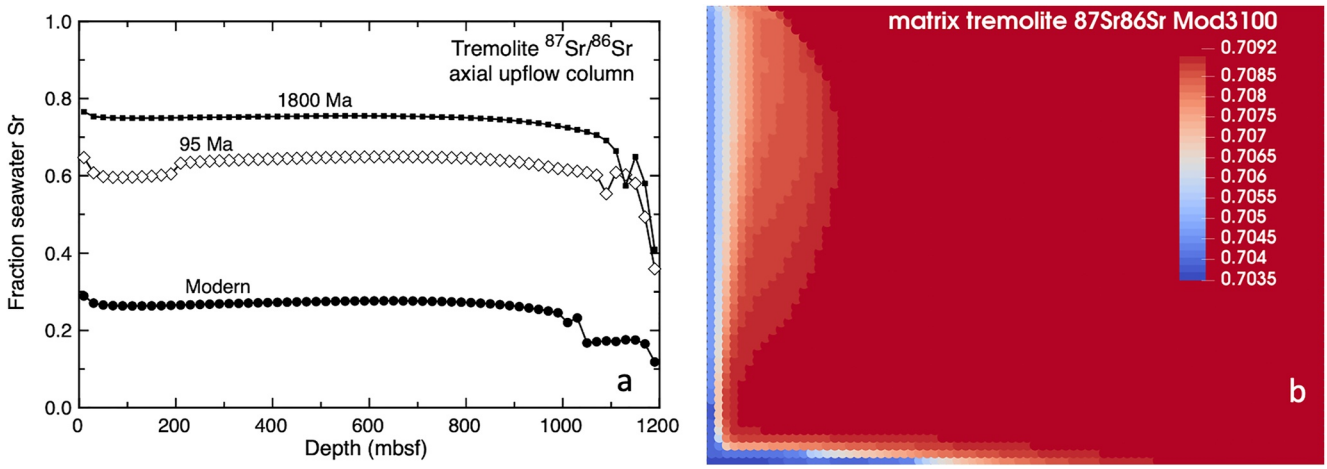

Figure 23. (a) Depth profile of Sr isotopic composition of secondary tremolite for different seawater compositions, expressed as the fraction of seawater Sr. The data are taken from the first column of the simulation, which represents a distance of 0–20 m from the spreading axis and includes the highest temperature upwelling fluids. (b) 2D map of tremolite $^{87}Sr/^{86}Sr$, using modern seawater as an example, showing that tremolite forming farther from the axis has higher $^{87}Sr/^{86}Sr$, although the majority of the tremolite forms within about 60 m of the axis. Tremolite that forms in the horizontal flow region at the base generally has lower $^{87}Sr/^{86}Sr$.

been interpreted as a back-arc spreading center, probably did have a slow spreading rate (Varga & Moores, 1985). The Oman ophiolites are inferred to represent faster spreading rates (Braun & Keleman, 2002), which would be more comparable to the model presented here.

The model paleo-vent fluids also have increased fluxes of HS^- and Na^+ to the oceans. According to the model results, when seawater has low SO_4, the hydrothermal system converts that sulfur to a reduced form at a substantial rate and does not significantly sequester sulfur into the oceanic crust. Also, the model suggests that when the seawater Na concentration is low, hydrothermal systems *leach Na from the rocks* and supply it to the oceans. On billion-year timescales the leaching rate would be high enough to supply a substantial fraction of seawater Na. Simulations with a model "early Archean" ocean with 210 mM Ca and 110 mM Na (see Halevy & Bachan, 2017 for the Ca concentration) indicate even larger Na enrichments in venting fluids relative to the contemporary oceans, enough to supply the current budget of seawater Na in less than 10^9 years. The implication is that early in Earth history, seawater Na could have been derived from ocean floor basalts rather than requiring continental weathering. For the modern system, there is little difference in Na between seawater and vent fluids, so the effects of the seafloor hydrothermal process are small relative to other fluxes of Na to the oceans, and do not significantly affect seawater Na.

7. Discussion

The models presented represent in two dimensions the fluid flow, reaction kinetics, alteration patterns, and Sr isotopic exchange between seawater and a model oceanic crustal section of 1.2 km vertical dimension. The heating rates and vertical dimension are similar to those inferred for fast spreading ridges; those with total spreading rates of about 10 cm/yr. However, the crustal sections of such ridges are inferred to have a two-layer permeability structure rather than the uniform permeability modeled here (Alt et al., 2010). The shallow convective layer tends to isolate the lower layer thermally, producing somewhat higher temperatures than in the current models. The effect of such higher temperatures can be inferred from the temperature-alteration relationships found in the current models (Figure 17b). Higher temperatures produce more rock alteration (assuming fluid flow is still large), and because the upper layer has relatively low temperatures, mostly restrict it to the lower layer (e.g., Alt et al., 2010).

Other evidence from Site 1,256 indicates that fast spreading ridges also incur alteration at temperatures well above 400°C (Alt et al., 2010), and under conditions where seawater is supercritical (Coumou et al., 2008). There has been no attempt to model those conditions here, mainly because they complicate the fluid flow and will require a focused effort at representing them accurately in reactive transport models that is beyond the scope of this paper. However, at temperatures in excess of 400°C it is also likely that permeabilities are low and fluid fluxes are much

15252027, 2022, 12, Downloaded from https://agupubs.onlinelibrary.wiley.com/doi/10.1029/2022GC010524, Wiley Online Library on [21/06/2023]. See the Terms and Conditions (https://onlinelibrary.wiley.com/terms-and-conditions) on Wiley Online Library for rules of use; OA articles are governed by the applicable Creative Commons License

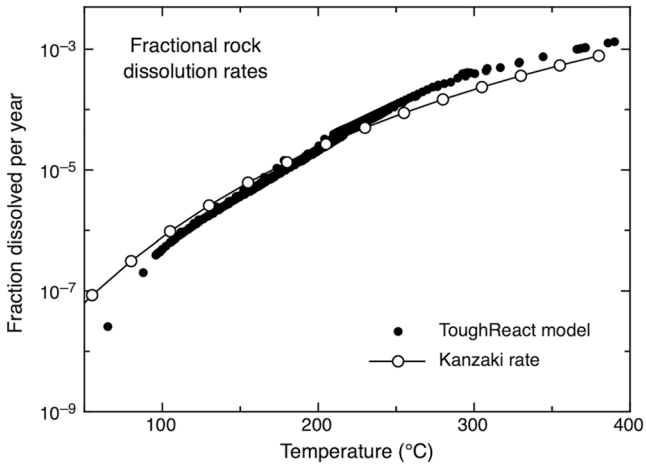

Figure 24. Comparison of matrix alteration rate in the Toughreact model to the bulk rock dissolution or exchange rate used by Kanzaki (2020), which is based on O isotope exchange experiments of Cole et al. (1987).

smaller. The preponderance of fluid flow in natural systems is inferred to be at temperature below 400°C (Driesner, 2010). Although higher temperature fluid fluxes deep in the hydrothermal systems must be low, the length of time the rocks spend at those high temperatures could be considerably longer, which must be the case to account for the $\delta^{18}O$ shifts observed in ophiolitic gabbro (Gregory, 2003).

In our model, fluids enter the upflow zone at 1,200 mbsf at temperatures above 350°C, but are cooled by about 100°C in the first 250 m of upflow. The venting fluids at the axis are further cooled to 210°C or 220°C. The initial large decrease in temperature is a result of admixed cool, rapidly descending seawater that is injected into the base of the upwelling zone. This effect is an unavoidable feature of the convection that results from the strong upwelling at the ridge axis. The fact that natural vent fluids can emerge on the seafloor at much higher temperature presumably requires appropriate permeability structure that can separate the hot upwelling fluid from the cool downwelling fluids only a few tens of meters away. The continued cooling of the axial upflow fluids is a consequence of the circulation around the stagnation zone, which causes cooler fluids to continually be mixed into the axial upflow fluids. Considering that the model allows us to "see" the deep fluids before they are cooled, the cooling effect does not prevent us from assessing the fluid chemistry produced at higher temperatures in the model. In general, the fluids at temperatures >300°C have near-zero Mg and SO_4, low $^{87}Sr/^{86}Sr$, and high Ca.

7.1. Reaction Rates

An important aspect of the model used here, described in more detail in Text S3 in Supporting Information S1, is that the fracture-matrix diffusion scheme sets a limit to the reaction rates of the matrix minerals at high temperature. This limit may in fact represent fairly accurately how a dual permeability system works at high temperature. The high temperature reaction rates therefore are appropriate even with the small mineral RSA's; the small RSA's compensate for diffusive transport limitations. However, in the model the small RSA's also apply to the lower temperature parts of the system, where diffusion between matrix and fractures does not limit reaction to the same extent. The consequence may be that the low-temperature reaction rates in the matrix could be too slow. If this were the case, then the curve shown in Figure 17b would have a lower slope below about 200°C. This could make some difference, but it might be subtle on the short timescales associated with high temperature alteration near the ridge axis. For example, rocks held at 100°C for 400 years might be 0.2% altered instead of 0.02%. This difference becomes much more significant for older seafloor rocks. An alternative explanation of the small RSA values needed for the simulations is that they compensate for the non-linear nature of plagioclase and pyroxene dissolution kinetics (Daval et al., 2010; Dixit & Carroll, 2007), an effect that may apply equally at low- and high temperature.

An interesting comparison is afforded by the approach of Kanzaki (2020) who used a model for hydrothermal convection and a simplified formulation of rock-fluid reaction rates to estimate the effect of hydrothermal exchange on oxygen isotopes. His model assumes porous flow, and his porosity of 5% matches ours for matrix. His rate of bulk O isotopic exchange, based on experimental data for fluid-rock effects on oxygen isotopes (Cole et al., 1987), is compared to our rock matrix alteration rates in Figure 24. The agreement is good above 100°C. As noted above, our rates might be too low below 100°C, but the change in alteration fraction on a 1,000-year timescale might be from 10^{-5} to 10^{-4}, which would not affect the results presented here. Limitations of the thermodynamic database above 300°C are not evident in Figure 24.

7.2. Fluid/Rock Ratios and Sr Isotopes

There has been much discussion about the effective fluid/rock ratios that should be used in conceptual models of MOR hydrothermal alteration (cf. Kanzaki, 2020). One aspect of the model presented here is to highlight the difficulty in reducing the system to a simple mass balance concept. An example that can be used for illustration

15252027, 2022, 12, Downloaded from https://agupubs.onlinelibrary.wiley.com/doi/10.1029/2022GC010524, Wiley Online Library on [21/06/2023]. See the Terms and Conditions (https://onlinelibrary.wiley.com/terms-and-conditions) on Wiley Online Library for rules of use; OA articles are governed by the applicable Creative Commons License

15252027, 2022, 12, Downloaded from https://agupubs.onlinelibrary.wiley.com/doi/10.1029/2022GC010524, Wiley Online Library on [21/06/2023]. See the Terms and Conditions (https://onlinelibrary.wiley.com/terms-and-conditions) on Wiley Online Library for rules of use; OA articles are governed by the applicable Creative Commons License

is the imaginative and largely insightful analysis done by Bickle and Teagle (1992) in an effort to understand the implications of Sr isotope modification of the Troodos ophiolite. They divided the hydrothermal exchange process into separate high temperature "equilibrium" regions and lower temperature "disequilibrium" or kinetically-controlled regions. They associated the low temperature region with downwelling fluids and the high temperature region with the narrow upwelling region. The problem highlighted by our model is that the downwelling regions are so cold that very little fluid-rock reaction occurs at all (see also Barker et al., 2008). The lower temperature alteration happens at the fringe of the upwelling region where the fluids have not been fully heated and/or are admixed with local downwelling fluids. The lower temperature alteration still tends to overprint the high-temperature alteration because the rocks start out at the ridge axis where temperatures are highest and migrate to lower temperatures over a period of thousands of years. Our simulations also indicate that the lower-T overprint will be associated with fluids that look chemically a lot more like seawater, so an important point is that altered rock will have interacted with fluids that *changed composition with time as temperature decreased*.

A problem with conceiving of the high-T part of the system as "equilibrium" is that it results in an inappropriate description of fluid Sr isotope ratio evolution. As Bickle and Teagle (1992) point out, equilibrium between fluid and rock in terms of Sr isotopes implies that an isotopic "front" moves through the rocks. This is an incorrect view of the process; it implies that the Damköhler numbers are >>1, whereas in fact they are <<1. The fluids in the rocks being altered at low temperature are upwelling fluids and largely vent to the ocean rather than feed the regions where higher temperature alteration is happening. However, there is downward flow of warm fluids that have previously reacted slightly with the rocks just outboard of the stagnation zone, although the temperatures are still substantially below 150°C and fluids reach the base of the upwelling region having retained $^{87}Sr/^{86}Sr$ that is little changed from that of seawater (Figure 12b).

The total fluid volume calculated by Bickle and Teagle (1992) to account for the Sr isotope shift in Troodos rocks is 3×10^7 kg/m^2, although this number should be decreased by 3× or 4× to account for higher seawater Sr concentration in the Cretaceous. The fluxes that come from our model in the high-T regions are in the range of 1,000–3,000 kg/m^2/yr. So 10 Ky of fluid flow would give an integrated number similar to that calculated by Bickle and Teagle (1992).

It isn't obvious how to calculate an effective fluid/rock ratio that can be used to approximate the isotopic shifts in the rocks. The integrated fluid flux of say, 10^7 kg/m^2 moving through rock that has a density of 3,000 kg/m^3 seems to imply a fluid/rock ratio of 3,000. If the fluid and rock equilibrated Sr isotopes as a closed system with this fluid/rock ratio, the rock $^{87}Sr/^{86}Sr$ ratio would be completely converted to the seawater ratio. Bickle and Teagle (1992) get around this point by hypothesizing that the fluid, before entering the high-T region, has already been modified to have a lower $^{87}Sr/^{86}Sr$ than seawater. Our model suggests that this is unlikely. As shown in Figure 16d, downwelling fluid reaches all the way to within three grid blocks of the bottom of the system without having its $^{87}Sr/^{86}Sr$ changed significantly.

Figure 25 shows the Bickle and Teagle (1992) concept, and something that more closely resembles what comes from our model. Using the same framework, fluid moves through the first 1.5 km without being modified much at all, then, as temperature ramps up over a short distance, rapidly shifts toward the rock value but not all the way to the rock value. Mixing with local downwelling fluids then causes the fluid $^{87}Sr/^{86}Sr$ to increase, and further reaction causes it to drift back to lower values as the fluid moves through the upwelling region. Different fluid paths trace different trajectories on this plot depending on what maximum temperatures they traverse, and much of the fluid is shifted by a lesser amount toward the rock $^{87}Sr/^{86}Sr$.

The Bickle and Teagle (1992) representation has value in understanding what is happening in our model system. The rock being traversed by downwelling fluid has already been altered and presumably has the endpoint $^{87}Sr/^{86}Sr$ of about 0.7054; it does not get further modified by the downwelling fluid. The downwelling fluid maintains the seawater value until it reaches the high-T region, which coincidentally is made up largely of fresh rock just formed at the ridge axis and with low $^{87}Sr/^{86}Sr$. As the fresh rock moves through the high-T aureole as a result of spreading, its $^{87}Sr/^{86}Sr$ gradually shifts toward the 0.7054 value. At no time has the rock and fluid $^{87}Sr/^{86}Sr$ value "equilibrated." Especially with regard to isotopic modification of the rocks, the process cannot be understood without accounting for and modeling the role of mineral-fluid reaction kinetics.

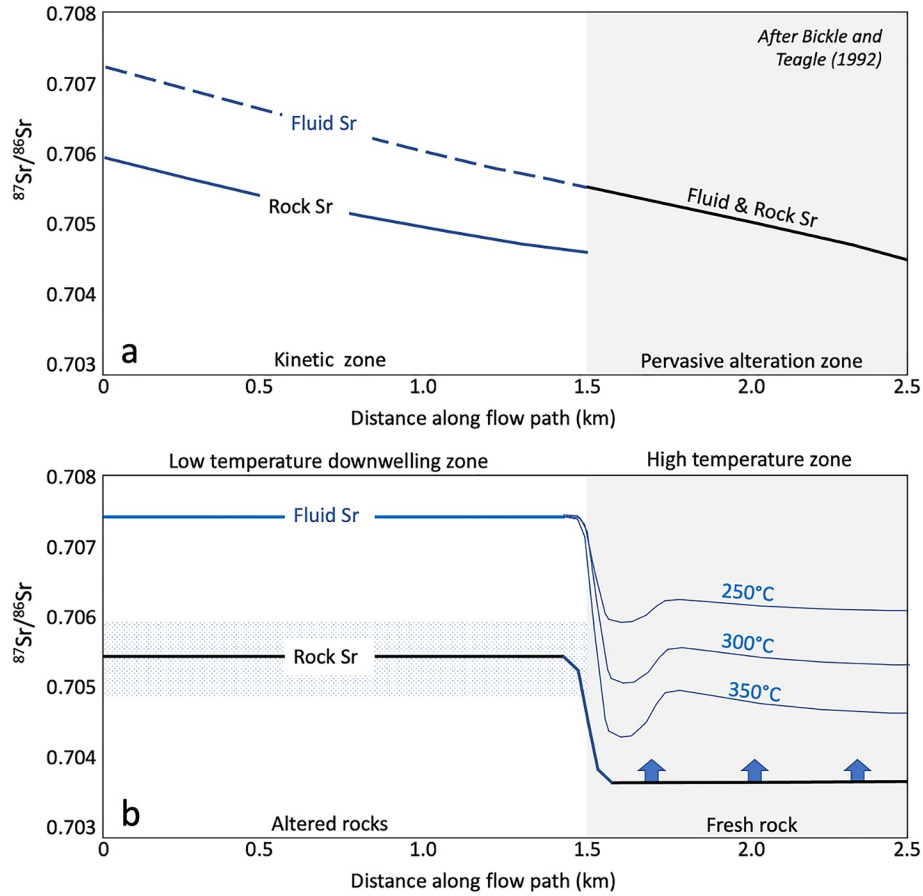

Figure 25. Representations of the evolution of $^{87}Sr/^{86}Sr$ in 95 Ma seawater fluid circulated into and through a MOR hydrothermal system. (a) After Bickle and Teagle (1992) for the Troodos ophiolite and (b) schematic representation of our model.

7.3. Precambrian "Mantle" Sr Isotope Evolution

An interesting issue in Precambrian mantle geochemistry is the discrepancy between the values estimated for mantle Nd and Hf isotopic ratios and those that have been found for Sr isotopes. This discrepancy is illustrated in Figure 26, which shows that the initial $^{87}Sr/^{86}Sr$ of a selection of Precambrian mafic rocks thought to represent the equivalent of modern oceanic mantle, and two curves (in bold) that describe the mantle evolution for Sr based on analogy with Nd and Hf isotopes. The bold curves use the measured Precambrian isotope ratios for Hf and Nd, and assume that the departure from the bulk Earth curve for Sr is proportional to that for Nd, with the proportionality indicated by that of modern oceanic basalts.

In most discussions of Precambrian mantle isotopic evolution, mantle Sr isotopes are either not mentioned (e.g., Vervoort & Blichert-Toft, 1999) or are not emphasized (McCulloch & Bennett, 1993). One reason is that it is unclear how representative the existing data are of the depleted mantle $^{87}Sr/^{86}Sr$ values. The uncertainty stems partly from the fact that the Sr data depart so strongly from the patterns established with Nd and Hf data, and partly from the recognition that Sr isotopes are more readily modified by post-magmatic processes. The modeling presented here amplifies this second explanation-that the high Sr concentrations, and low SO_4 concentrations, in the Precambrian oceans caused the Sr isotopic composition of oceanic crust to be much more affected by hydrothermal exchange with seawater. The high-$^{87}Sr/^{86}Sr$ oceanic crust, when subducted, could carry its signal into the mantle where it may have affected the Sr isotopic composition of island-arc rocks such as those represented by the 1.73 Ga rock compositions plotted in Figure 25.

The effect of ocean floor basalt Sr exchange with seawater could have been a maximum at about 1.6–2.0 Ga because it took until about 2.0 Ga for seawater to evolve a relatively high $^{87}Sr/^{86}Sr$ ratio of about 0.7045–0.7048

15252027, 2022, 12, Downloaded from https://agupubs.onlinelibrary.wiley.com/doi/10.1029/2022GC010524, Wiley Online Library on [21/06/2023]. See the Terms and Conditions (https://onlinelibrary.wiley.com/terms-and-conditions) on Wiley Online Library for rules of use; OA articles are governed by the applicable Creative Commons License

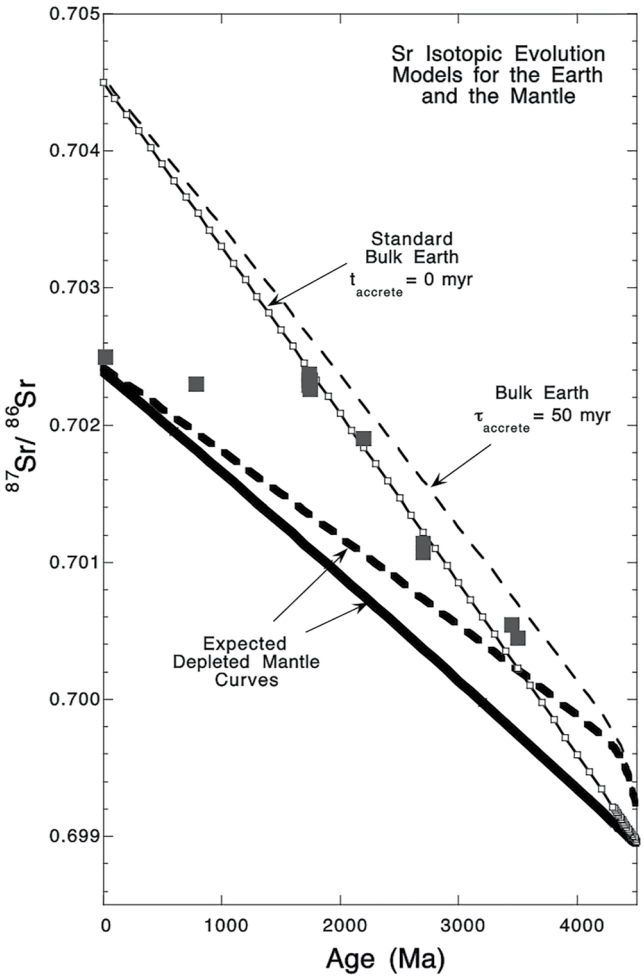

Figure 26. Sr isotopic evolution diagram showing bulk Earth evolution, expected "depleted mantle" evolution, and some available data on Mantle Sr isotopic composition. The modern (MORB) data (typical $^{87}Sr/^{86}Sr = 0.7025$) show the strong depletion effects of preferential loss of Rb from the mantle and fit the depleted mantle models. The samples older than 1,700 Ma plot substantially above the depleted mantle lines. The contrast between the modern and Precambrian samples, especially for those at 1,600 to 2,000 Ma, is problematical. The curve labeled $\tau_{accrete} = 50$ myr corresponds to a model of extended Earth accretion as discussed by Halliday (2000). The extended accretion model elevates the effective initial ratio of the Earth and hence makes the measured $^{87}Sr/^{86}Sr$ ratios plot below the bulk Earth line and hence look more like "depleted mantle" values. The bulk Earth curve could also be moved to slightly higher values by making the modern endpoint higher than 0.7045. The Sr data are taken from Stern and Abdelsalam (1998) (790 Ma), McCulloch (1994) (3,504 Ma), Zindler (1982) (2,704 Ma), Machado et al., 1986 (3,500 Ma), DePaolo, unpublished (1,730 Ma).

(Shields & Veizer, 2002). Subsequent to 1.6 Ga, the Ca and Sr concentrations of seawater may have been lower, decreasing the size of the effect (Halevy & Bachan, 2017), at least until the Phanerozoic when the seawater $^{87}Sr/^{86}Sr$ was higher. However, even in the Archean, Sr isotopic modification of ocean floor rocks may have been extreme if the seawater Sr concentration were as high as 400 ppm. In fact, the entire global Sr cycle may have been quite different.

8. Summary and Conclusions

Our simplified MOR hydrothermal model is useful for a first look at the likely internal structure of hydrothermal systems, and the relationships between temperature, fluid flux, fluid composition, and rock alteration. Further modifications are needed to improve the correspondence between model and natural systems, but the simple model provides useful insight into what can be gained from simulations. In this work, we place an emphasis on using the model to evaluate effects of changing seawater chemical composition, but it also provides an initial view of relationships between chemistry, mineralogy, heat flux, and fluid flow.

8.1. Fluid Chemistry

The simple representation using modern seawater and a rectangular computational grid with dual permeability and heating from below produces fracture fluid compositions at $T > 300°C$ that have the characteristics of observed vent fluids on the seafloor. The model fluids have low Mg (≤1 mM), zero SO_4, a small amount of HS-, elevated Ca, Sr concentration slightly higher than seawater, and $^{87}Sr/^{86}Sr$ near 0.704. The model unaltered rock has the chemical composition of typical MORB with a diabase mineralogy, no glass, Sr concentration of about 120 ppm, and $^{87}Sr/^{86}Sr$ of 0.7028.

8.2. Mineralogy, Heating, Permeability, and Fracture Spacing

The model primary rock mineralogy is based on a typical igneous assemblage, adjusted to give a bulk composition close to average MORB. The array of secondary minerals considered is guided by observations in ophiolites and basement drill cores. The model fracture spacing of 2 m is close to the average observed in ophiolites. Heating rate and permeability were adjusted to yield steady flow with a maximum temperature <400°C to minimize critical point effects on flow. The basal heat flux is compatible with a shallow magma lens 200–300 m below the computational grid. The (fracture) permeability used is 1.5×10^{-14} m^2, close to an average inferred value for the real systems. Fracture spacing is an important parameter, simulations with larger fracture spacing (4 or 10 m) tend to isolate the matrix too much from the fracture flow so that the fracture fluids do not evolve sufficiently as they pass through the model system.

8.3. Role of Fractures

A dual permeability grid allows us to evaluate separately the fluid flow and chemical evolution in fractures and in the larger volume of rock matrix. Because flow is confined almost entirely to fractures, flow velocities reach 500–1,000 m/yr or more in the upflow zone, consistent with residence time estimates. We have a baseline model where reaction timescales are similar for matrix and fracture minerals, and another version where the reaction timescales are accelerated in the fractures. For the baseline model fracture fluids tend not to reach zero Mg except

15252027, 2022, 12, Downloaded from https://agupubs.onlinelibrary.wiley.com/doi/10.1029/2022GC010524, Wiley Online Library on [21/06/2023]. See the Terms and Conditions (https://onlinelibrary.wiley.com/terms-and-conditions) on Wiley Online Library for rules of use; OA articles are governed by the applicable Creative Commons License

15252027, 2022, 12, Downloaded from https://agupubs.onlinelibrary.wiley.com/doi/10.1029/2022GC010524, Wiley Online Library on [21/06/2023]. See the Terms and Conditions (https://onlinelibrary.wiley.com/terms-and-conditions) on Wiley Online Library for rules of use; OA articles are governed by the applicable Creative Commons License

at the highest temperatures, which is a consequence of the high fluid velocities in the fractures. With accelerated fracture mineral dissolution rates the fluids have near-zero Mg over a wider temperature range and spatial extent. We use the baseline model to assess longer term effects of fluid-rock interaction because the fracture mineral evolution is too fast when reaction kinetics are accelerated. This simplification doesn't greatly affect the amount of alteration that occurs in the rock matrix; and rock matrix accounts for 99.5% of rock mass. In a natural system it is likely that reactions are faster near the fractures, but also that new fractures are continually generated and replace older fractures, so that the average fracture mineralogy doesn't evolve too quickly. Our current model does not have the capacity to simulate new fracture formation during a simulation, but that could be a feature that could be useful if sufficiently well constrained. Our current interpretation is that rapid fracture mineral reaction, and continual production of fresh fractures, are needed to yield fully evolved vent fluids.

8.4. Alteration Rate

In our models, alteration rate depends mainly on temperature, and alteration extent depends on temperature-time history. This simple relationship may apply only when fluid flow is adequate and there is sufficient porosity. In our model, porosity is more or less constant and about 5% in matrix, and permeability is also constant. At temperatures sufficiently in excess of 400°C, permeability and porosity are likely to be smaller and the extent of alteration could be less strongly correlated with temperature.

8.5. Permeability Evolution

In our models we have made permeability independent of porosity. Anhydrite formation does decrease porosity near the base of the upwelling zone, and simulations that include a porosity-permeability feedback show that the permeability changes cause significant changes in flow of the high temperature fluids. The overall effects on the system are not large. Fluid chemistry, typical flow velocities, and rock alteration patterns change minimally. Secondary mineral formation, including anhydrite formation in fractures, is balanced by primary mineral dissolution, and this effect plus continuing fracture generation may cause average permeability to remain close to constant on 100- to 1,000-year timescales.

8.6. Reaction Rates

The dual permeability model requires adjustments to mineral reaction rates to account properly for diffusive transport between matrix blocks and fractures. For reasons detailed in Text S3 in Supporting Information S1, we have done this by setting the RSA of the primary minerals to a value of 0.00004 m^2/kg. This value yields alteration timescales for the 2-m fracture spacing model that accord with observations of natural systems (Figures 17 and 23), and in any case are close to maxima because the formulation used for fracture-matrix communication limits high temperature reaction rates in the matrix blocks (Text S3 in Supporting Information S1). We use secondary mineral RSA values that are 2× the values for the primary minerals (0.00008 m^2/kg). The reaction rates for the primary secondary minerals chlorite and amphibole are similar to those of plagioclase and pyroxenes (Text S1 in Supporting Information S1). Additional adjustment was made to the RSA of albite to enhance its formation. Anhydrite kinetics at elevated temperatures are not well constrained by available data. We have used celestite kinetics from Dove and Czank (1995), which are consistent with the experimental results of Syverson et al. (2018).

8.7. Seawater Composition Effects

At various times in the geologic past seawater had higher Ca and Sr concentration, and lower SO_4, Mg, and Na than modern seawater. Deep water temperature and pH were also different. We used the model to evaluate the effect of changing seawater composition while keeping all other input parameters the same. Using model seawater compositions for the Cretaceous (95 Ma) and early Proterozoic (1,800 Ma), we find that the evolution of fluid $^{87}Sr/^{86}Sr$ is limited and vent fluid compositions are much less shifted toward rock values and more similar to the seawater values. A correlative effect is that altered seafloor rocks take on $^{87}Sr/^{86}Sr$ values that are much more strongly shifted toward the seawater values. As with modern systems, vent fluids are somewhat enriched in Ca and Sr relative to seawater and have zero SO_4 and near-zero Mg. Unlike modern systems, in paleo-seawater

15252027, 2022, 12, Downloaded from https://agupubs.onlinelibrary.wiley.com/doi/10.1029/2022GC010524, Wiley Online Library on [21/06/2023]. See the Terms and Conditions (https://onlinelibrary.wiley.com/terms-and-conditions) on Wiley Online Library for rules of use; OA articles are governed by the applicable Creative Commons License

systems much less anhydrite is formed, vent fluids are quite highly enriched in reduced sulfur as HS-, and are substantially enriched in Na relative to the contemporaneous seawater. The latter results suggest that MOR hydrothermal systems could have been a significant contributor to keeping the oceans in a reducing state when SO_4 was low, and could be the ultimate source of seawater Na in the Archean, before emergent continents were a major source.

8.8. Limitations of 2D Static Simulations

Our simulations do not account for effects that can only be fully represented by 3D simulations that include spreading. The rapid ascent and minimal cooling of fluids such as those observed at black smokers is a consequence of the formation of cylindrical pipes with high permeability that are sufficiently isolated from cool downwelling fluids that the deep, hot fluids can flow quickly to the seafloor vents without cooling. They also move heat out of the deeper regions efficiently and could alter the overall thermal structure. The effects of fracture clogging by anhydrite and its effect on flow also is not addressed in our models, and can probably only be appropriately treated in 3D. The continuous movement of rock away from the ridge due to spreading means that most of the rock in the cooler parts of the system has already been altered near the ridge axis. We have not tested this effect extensively, except for a few experimental runs with zero olivine, and with chlorite and amphibole as additional primary minerals. These experiments showed only minor differences relative to those with the typical igneous mineralogy.

8.9. Future Work

There are many additional features that can be added to the simulations, and most of those can be implemented in ToughReact. The next generation of models could evaluate slower spreading systems with deeper circulation, ultramafic host rocks, two-layered permeability systems, enhanced vertical permeability, seafloor spreading, alternate mineral kinetic formulations, and the effects of sediment cover. Improved modeling of the rock alteration process is important, because many observational constraints come from study of altered rocks. Three-dimensional simulations might also be useful, but represent another level of computational power and parameter sensitivity analysis. The ultimate goal, to have models that are realistic enough to be a valuable parallel effort to accompany continued observation and characterization of natural systems, probably requires a community effort. The simulations also suggest that better data and models are needed for mineral reaction kinetics and trace element partitioning.

Data Availability Statement

Input and output files, as well selected figures used for the simulation results shown in the manuscript and the Supporting Information S1 are available at Zenodo (CERN Data Centre) via https://doi.org/10.5281/zenodo.7328447 with open access. Version 4.13 of the TOUGHREACT software, similar to that used for MOR hydrothermal system simulations described in the manuscript, is described at https://tough.lbl.gov/software/toughreact_v4-13-omp/, and is available with an Academic, Commercial, Government, or Collaborator license agreement at https://marketplace.lbl.gov/search?q=toughreact.

Acknowledgments
This work has been supported by an EAGER grant from NSF Marine Geology and Geophysics (OCE2103214) and partly through a prior Grant (OCE1737186). ELS also acknowledges support from the Department of Energy, Office of Energy Efficiency and Renewable Energy, Geothermal Technologies Program, under award number DE-AC02-05CH11231 to the Lawrence Berkeley National Laboratory. A thoughtful review by Norm Sleep is gratefully acknowledged, as are helpful comments on earlier drafts by Jim Watkins, Frank Richter, and Jenny Druhan.

References

Alexander, R. J., Harper, G. D., & Bowman, J. R. (1993). Oceanic faulting and fault-controlled subseafloor hydrothermal alteration in the sheeted dike complex of the Josephine ophiolite. *Journal of Geophysical Research*, *98*(B6), 9731–9759. https://doi.org/10.1029/92jb01413

Allen, D. E., & Seyfried, W. E., Jr. (2003). Compositional controls on vent fluids from ultramafic-hosted hydrothermal systems at midocean ridges: An experimental study at 400°C, 500 bars. *Geochimica et Cosmochimica Acta*, *67*(8), 1531–1542. https://doi.org/10.1016/s0016-7037(02)01173-0

Alt, J. C. (1995). Sulfur isotopic profile through the oceanic crust: Sulfur mobility and seawater-crustal sulfur exchange during hydrothermal alteration. *Geology*, *23*(7), 585–588. https://doi.org/10.1130/0091-7613(1995)023<0585:siptto>2.3.co;2

Alt, J. C., Honnorez, J., Laverne, C., & Emmermann, R. (1986). Hydrothermal alteration of a 1 km section through the upper oceanic crust, deep sea drilling project Hole 504B: Mineralogy, chemistry, and evolution of seawater-basalt interactions. *Journal of Geophysical Research: Solid Earth*, *91*(B10), 10309–10335. https://doi.org/10.1029/jb091ib10p10309

Alt, J. C., Laverne, C., Coggon, R. M., Teagle, D. A. H., Banerjee, N. R., Morgan, S., et al. (2010). Subsurface structure of a submarine hydrothermal system in ocean crust formed at the East Pacific Rise, ODP/IODP Site 1256. *Geochemistry, Geophysics, Geosystems*, *11*(10), Q10010. https://doi.org/10.1029/2010GC003144

Alt, J. C., & Teagle, D. A. H. (2000). Hydrothermal alteration and fluid fluxes in ophiolites and oceanic crust. In: In Y. Dilek, E. M. Moores, D. Elthon, & A. Nicolas (Eds.), *Ophiolites and oceanic crust: New insights from field studies and the ocean drilling program, Geological Society of America special paper* (Vol. *349*, pp. 273–282).

Alt, J. C., Teagle, D. A. H., Laverne, C., Vanko, D., Bach, W., Honnorez, J., et al. (1996). Ridge flank alteration of upper ocean crust in the eastern Pacific: A synthesis of results for volcanic rocks of Holes 504B and 896A. In J. C. Alt, H. Kinoshita, L. B. Stokking, & P. J. Michael (Eds.), *Proceedings of the ocean drilling program, science result* (Vol. 148, pp. 435–452). Ocean Drilling Program.

Antonelli, M. A., Pester, N. J., Brown, S. T., & DePaolo, D. J. (2017). Effect of paleoseawater composition on hydrothermal exchange in midocean ridges. *Proceedings of the National Academy of Sciences*, *144*(47), 12413–12418. https://doi.org/10.1073/pnas.1709145114

Aradóttir, E. S. P., Sonnenthal, E. L., Björnsson, G., & Jónsson, H. (2012). Multidimensional reactive transport modeling of CO_2 mineral sequestration in basalts at the Hellisheidi geothermal field, Iceland. *International Journal of Greenhouse Gas Control*, *9*, 24–40. https://doi.org/10.1016/j.ijggc.2012.02.006

Aradóttir, E. S. P., Sonnenthal, E. L., & Jónsson, H. (2012). Development and evaluation of a thermodynamic dataset for phases of interest in CO_2 mineral sequestration in basaltic rocks. *Chemical Geology*, *304*, 26–38. https://doi.org/10.1016/j.chemgeo.2012.01.031

Bach, W., & Humphris, S. E. (1999). Relationship between the Sr and O isotope compositions of hydrothermal fluids and the spreading and magma-supply rates at oceanic spreading centers. *Geology*, *27*(12), 1067–1070. https://doi.org/10.1130/0091-7613(1999)027<1067:rbtsao>2.3.co;2

Baker, E. T. (2007). Hydrothermal cooling of midocean ridge axes: Do measured and modeled heat fluxes agree? *Earth and Planetary Science Letters*, *263*(1–2), 140–150. https://doi.org/10.1016/j.epsl.2007.09.010

Barker, A. K., Coogan, L. A., Gillis, K. M., & Weis, D. (2008). Strontium isotope constraints on fluid flow in the sheeted dike complex of fast spreading crust: Pervasive fluid flow at Pito Deep. *Geochemistry, Geophysics, Geosystems*, *9*(6), Q06010. https://doi.org/10.1029/2007GC001901

Barreyre, T., Olive, J.-A., Crone, T. J., & Sohn, R. A. (2018). Depth-dependent permeability and heat output at basalt-hosted hydrothermal systems across mid-ocean ridge spreading rates. *Geochemistry, Geophysics, Geosystems*, *19*(4), 1259–1281. https://doi.org/10.1002/2017GC007152

Berndt, M. E., Seyfried, W. E., Jr., & Beck, J. W. (1988). Hydrothermal alteration processes at midocean ridges: Experimental and theoretical constraints from Ca and Sr exchange reactions and Sr isotopic ratios. *Journal of Geophysical Research*, *93*(B5), 4573–4583. https://doi.org/10.1029/jb093ib05p04573

Berner, R. A. (1991). A model for atmospheric CO_2 over Phanerozoic time. *American Journal of Science*, *291*(4), 339–376. https://doi.org/10.2475/ajs.291.4.339

Berner, R. A. (2003). Long term carbon cycle, fossil fuels, and atmospheric composition. *Nature*, *426*(6964), 323–326. https://doi.org/10.1038/nature02131

Berner, R. A. (2004). A model for calcium, magnesium and sulfate in seawater over Phanerozoic time. *American Journal of Science*, *304*(5), 438–453. https://doi.org/10.2475/ajs.304.5.438

Bickle, M. J., & Teagle, D. A. (1992). Strontium alteration in the Troodos ophiolite: Implications or fluid fluxes and geochemical transport in mid-ocean ridge hydrothermal systems. *Earth and Planetary Science Letters*, *113*(1–2), 219–237. https://doi.org/10.1016/0012-821x(92)90221-g

Blättler, C. L., & Higgins, J. A. (2014). Calcium isotopes in evaporites record variations in Phanerozoic seawater SO_4 and Ca. *Geology*, *42*(8), 711–714. https://doi.org/10.1130/g35721.1

Bosch, D., Jamais, M., Boudier, F., Nicolas, A., Dautria, J.-M., & Agrinier, P. (2004). Deep and high-temperature hydrothermal circulation in the Oman ophiolite—Petrological and isotopic evidence. *Journal of Petrology*, *45*(6), 1181–1208. https://doi.org/10.1093/petrology/egh010

Bowers, T. S., Campbell, A. C., Measures, C. I., Spivack, A. J., & Edmond, J. M. (1988). Chemical controls on the composition of vent fluids at 13°–11°N and 218°N East Pacific Rise. *Journal of Geophysical Research*, *93*(B5), 4522–4536. https://doi.org/10.1029/jb093ib05p04522

Bowers, T. S., & Taylor, H. P., Jr. (1986). An integrated chemical and stable-isotope model of the origin of mid-ocean ridge hot spring systems. *Journal of Geophysical Research*, *90*(B14), 12583–12606. https://doi.org/10.1029/jb090ib14p12583

Braun, M. G., & Keleman, P. B. (2002). Dunite distribution in the Oman Ophiolite: Implications for melt flux through porous dunite conduits. *Geochemistry, Geophysics, Geosystems*, *3*(11), 8603–8621. https://doi.org/10.1029/2001GC000289

Butterfield, D. A., Massoth, G. J., McDuff, R. E., Lupton, J. E., & Lilley, M. D. (1990). Geochemistry of hydrothermal fluids from Axial Seamount hydrothermal emissions study vent field, Juan de Fuca Ridge: Subseafloor boiling and subsequent fluid-rock interaction. *Journal of Geophysical Research*, *95*(B8), 12895–12921. https://doi.org/10.1029/jb095ib08p12895

Butterfield, D. A., McDuff, R. E., Mottl, M. J., Lilley, M. D., Lupton, J. E., & Massoth, G. J. (1994). Gradients in the composition of hydrothermal fluids from the Endeavor Segment vent field: Phase separation and brine loss. *Journal of Geophysical Research*, *99*(B5), 9561–9583. https://doi.org/10.1029/93jb03132

Butterfield, D. A., Nelson, B. K., Wheat, C. G., Mottl, M. J., & Roe, K. K. (2001). Evidence for basaltic Sr in midocean ridge-flank hydrothermal systems and implications for the global oceanic Sr isotope balance. *Geochimica et Cosmochimica Acta*, *65*(22), 4141–4153. https://doi.org/10.1016/s0016-7037(01)00712-8

Canales, J. P., Detrick, R. S., Carbotte, S. M., Kent, G. M., Diebold, J. B., Harding, A., et al. (2005). Upper crustal structure and axial topography at intermediate spreading ridges: Seismic constraints from the southern Juan de Fuca Ridge. *Journal of Geophysical Research*, *110*(B12), B12104. https://doi.org/10.1029/2005JB003630

Cathles, L. M. (1993). A capless 350°C flow zone model to explain megaplumes, salinity variations, and high-temperature veins in ridge axis hydrothermal systems. *Economic Geology*, *88*(8), 1977–1988. https://doi.org/10.2113/gsecongeo.88.8.1977

Charlou, J. L., Fouquet, Y., Donval, J. P., Auzende, J. M., Jean-Baptiste, P., Stievenard, M., & Michel, S. (1996). Mineral and gas chemistry of hydrothermal fluids on an ultrafast spreading ridge: East Pacific Rise, 17° to 19°S (Naudur cruise, 1993) phase separation processes controlled by volcanic and tectonic activity. *Journal of Geophysical Research*, *101*(15), 899–815. https://doi.org/10.1029/96jb00880

Chen, Y. J., & Morgan, J. P. (1996). The effects of spreading rate, the magma budget, and the geometry of magma emplacement on the axial heat flux at mid-ocean ridges. *Journal of Geophysical Research*, *101*(B5), 11475–11482. https://doi.org/10.1029/96jb00330

Cherkaoui, A. S. M., Wilcock, W. S. D., Dunn, R. A., & Toomey, D. R. (2003). A numerical model of hydrothermal cooling and crustal accretion at a fast spreading mid-ocean ridge. *Geochemistry, Geophysics, Geosystems*, *4*(9), 8616. https://doi.org/10.1029/2001GC000215

Cole, D. R., Mottl, M. J., & Ohmoto, H. (1987). Isotopic exchange in mineral-fluid systems. II. Oxygen and hydrogen isotopic investigation of the experimental basalt-seawater system. *Geochimica et Cosmochimica Acta*, *51*(6), 1523–1538. https://doi.org/10.1016/0016-7037(87)90334-6

Coogan, L. A. (2009). Altered oceanic crust as an inorganic record of paleoseawater Sr concentration. *Geochemistry, Geophysics, Geosystems*, *10*(Q04001). https://doi.org/10.1029/2008GC002341

Coogan, L. A., & Dosso, S. (2012). An internally consistent, probabilistic, determination of ridge-axis hydrothermal fluxes from basalt-hosted hydrothermal systems. *Earth and Planetary Science Letters*, *323*, 92–101. https://doi.org/10.1016/j.epsl.2012.01.017

Coogan, L. A., & Gillis, K. M. (2013). Evidence that low-temperature oceanic hydrothermal systems play an important role in the silicate-carbonate weathering cycle and long-term climate regulation. *Geochemistry, Geophysics, Geosystems*, *14*(6), 1771–1786. https://doi.org/10.1002/ggge.20113

15252027, 2022, 12, Downloaded from https://agupubs.onlinelibrary.wiley.com/doi/10.1029/2022GC010524, Wiley Online Library on [21/06/2023]. See the Terms and Conditions (https://onlinelibrary.wiley.com/terms-and-conditions) on Wiley Online Library for rules of use; OA articles are governed by the applicable Creative Commons License

Coogan, L. A., & Gillis, K. M. (2018). Low-temperature alteration of the seafloor: Impacts on ocean chemistry. *Annual Review of Earth and Planetary Sciences*, *46*(1), 21–45. https://doi.org/10.1146/annurev-earth-082517-010027

Coumou, D., Driesner, T., & Heinrich, C. A. (2008). The structure and dynamics of mid-ocean ridge hydrothermal systems. *Science*, *321*(5897), 1825–1828. https://doi.org/10.1126/science.1159582

Coumou, D., Weiss, P., Driesner, T., & Heinrich, C. A. (2009). Phase separation, brine formation, and salinity variation at Black Smoker hydrothermal systems. *Journal of Geophysical Research*, *114*(B3), B03212. https://doi.org/10.1029/2008JB005764

Crowe, S. A., Paris, G., Katsev, S., Jones, C., Kim, S.-T., Zerkle, A. L., et al. (2014). Sulfate was a trace constituent of Archean seawater. *Science*, *346*(6210), 735–739. https://doi.org/10.1126/science.1258966

Daval, D., Hellmann, R., Corvisier, J., Tisserand, D., Martinez, I., & Guyot, F. (2010). Dissolution kinetics of diopside as a function of solution saturation state: Macroscopic measurements and implications for modeling of geological storage of CO_2. *Geochimica et Cosmochimica Acta*, *74*(9), 2615–2633. https://doi.org/10.1016/j.gca.2010.02.003

Dixit, S., & Carroll, S. A. (2007). Effect of solution saturation state and temperature on diopside dissolution. *Geochemical Transactions*, *8*(1), 3. https://doi.org/10.1186/1467-4866-8-3

Dove, P. M., & Czank, C. A. (1995). Crystal chemical controls on the dissolution kinetics of the isostructural sulfates: Celestite, anglesite, and barite. *Geochimica et Cosmochimica Acta*, *59*(10), 1907–1915. https://doi.org/10.1016/0016-7037(95)00116-6

Driesner, T. (2010). The interplay of permeability and fluid properties as a first order control of heat transport, venting temperatures and venting salinities at mid-ocean ridge hydrothermal systems. *Geofluids*, *10*, 132–141. https://doi.org/10.1111/j.1468-8123.2009.00273.x

Edmond, J. M., Measures, C., McDuff, R. E., Chan, L., Collier, R., Grant, B., et al. (1979). Ridge crest hydrothermal activity and the balances of the major and minor elements in the ocean: The Galapagos data. *Earth and Planetary Science Letters*, *46*, 1–18. https://doi.org/10.1016/0012-821x(79)90061-x

Edmond, J. M., Von Damm, K. L., McDuff, R. E., & Measures, C. I. (1982). Chemistry of hot springs on the East Pacific Rise and their effluent dispersal. *Nature*, *297*(5863), 187–191. https://doi.org/10.1038/297187a0

Elderfield, H., & Schultz, A. (1996). Mid-ocean ridge hydrothermal fluxes and the chemical composition of the ocean. *Annual Review of Earth and Planetary Sciences*, *24*(1), 191–224. https://doi.org/10.1146/annurev.earth.24.1.191

Farough, A., Moore, D. E., Lockner, D. A., & Lowell, R. P. (2016). Evolution of fracture permeability of ultramafic rocks undergoing serpentinization at hydrothermal conditions: An experimental study. *Geochemistry, Geophysics, Geosystems*, *17*(1), 44–55. https://doi.org/10.1002/2015gc005973

Fisher, A. T., Alt, J., & Bach, W. (2014). Hydrogeologic properties, processes, and alteration in the igneous ocean crust. *Developments in Marine Geology*, *7*, 507–551. https://doi.org/10.1016/B978-0-444-62617-2.00018-9

Francois, L. M., & Walker, J. C. G. (1992). Modelling the phanerozoic carbon cycle and climate: Constraints from the $^{87}Sr/^{86}Sr$ isotopic ratio of seawater. *American Journal of Science*, *292*(2), 81–135. https://doi.org/10.2475/ajs.292.2.81

Gale, A., Dalton, C. A., Langmuir, C. H., Su, Y., & Schilling, J.-G. (2013). The mean composition of ocean ridge basalts. *Geochemistry, Geophysics, Geosystems*, *14*(3), 489–518. https://doi.org/10.1029/2012GC004334

Gallant, R. M., & Von Damm, K. L. (2006). Geochemical controls on the hydrothermal fluids from the Kairei and Edmond vent fields, 23°–25°S, Central Indian ridge. *Geochemistry, Geophysics, Geosystems*, *7*(6), Q06018. https://doi.org/10.1029/2005gc001067

Gilbert, L. A., Bona, M. L., Nishioka, T., Kodama, K., Mochizuki, N., & Tsunakawa, H. (2016). Permeability of oceanic crustal rock samples from IODP Hole 1256D. *Geochemistry, Geophysics, Geosystems*, *17*(7), 3825–3832. https://doi.org/10.1002/2016GC006406

Gillis, K. M. (1995). Controls on hydrothermal alteration in a section of fast-spreading oceanic crust. *Earth and Planetary Science Letters*, *134*(3–4), 473–489. https://doi.org/10.1016/0012-821x(95)00137-2

Gillis, K. M., Coogan, L. A., & Pedersen, R. (2005). Strontium isotope constraints on fluid flow in the upper oceanic crust at the East Pacific Rise. *Earth and Planetary Science Letters*, *232*(1–2), 83–94. https://doi.org/10.1016/j.epsl.2005.01.008

Gillis, K. M., & Sapp, K. (1997). Distribution of porosity in a section of upper oceanic crust exposed in the Troodos Ophiolite. *Journal of Geophysical Research*, *102*(B5), 10133–10149. https://doi.org/10.1029/96jb03909

Gregory, R. T. (2003). Ophiolites and global geochemical cycles: Implications for the isotopic evolution of seawater. In Y. Dilek & P. T. Robinson (Eds.), *Ophiolites in earth history* (Vol. 218, pp. 353–368). Geological Society, London, Special Publications.

Habicht, K. S., Gade, M., Thamdrup, B., Berg, P., & Canfield, D. E. (2002). Calibration of sulfate levels in the Archean ocean. *Science*, *298*(5602), 2372–2374. https://doi.org/10.1126/science.1078265

Halevy, I., & Bachan, A. (2017). The geologic history of seawater pH. *Science*, *355*(6329), 1069–1071. https://doi.org/10.1126/science.aal4151

Halliday, A. N. (2000). Terrestrial accretion rates and origin of the Moon. *Earth and Planetary Science Letters*, *176*(1), 17–30. https://doi.org/10.1016/s0012-821x(99)00317-9

Hasenclever, J., Theissen-Krah, S., Rüpkel, L. H., Morgan, J. P., Iyer, K., Petersen, S., & Devey, C. W. (2014). Hybrid shallow on-axis and deep off-axis hydrothermal circulation at fast-spreading ridges. *Nature*, *508*(7497), 508–512. https://doi.org/10.1038/nature13174

Heft, K. L., Gillis, K. M., Pollock, M. A., Karson, J. A., & Klein, E. M. (2008). Role of upwelling hydrothermal fluids in the development of alteration patterns at fast spreading ridges: Evidence from the sheeted dike complex at Pito Deep. *Geochemistry, Geophysics, Geosystems*, *9*(5), Q05O07. https://doi.org/10.1029/2007GC001926

Hellman, R., Daval, D., & Tisserand, D. (2010). The dependence of albite feldspar dissolution kinetics on fluid saturation state at acid and basic pH: Progress towards a universal relation. *Comptes Rendus Geoscience*, *342*(7–8), 676–684. https://doi.org/10.1016/j.crte.2009.06.004

Hess, J., Bender, M., & Schilling, J.-G. (1991). Evolution of the ratio of strontium-87 to strontium-86 in seawater from Cretaceous to present. *Science*, *231*(4741), 979–984. https://doi.org/10.1126/science.231.4741.979

Holland, H. D. (1984). *The chemical evolution of the atmosphere and oceans*. Princeton University Press.

Holland, H. D. (2003). The geologic history of seawater. In H. Elderfield, H. D. Holland, & T. K. Turekian (Eds.), *Treatise on geochemistry, volume 6: The oceans and marine geochemistry* (pp. 583–625). Elsevier.

Horita, J., Zimmerman, H., & Holland, H. D. (2002). Chemical evolution of seawater during the phanerozoic: Implications from the record of marine evaporites. *Geochimica et Cosmochimica Acta*, *66*, 3733–3745.

Ingebritsen, S. E., Geiger, S., Hurwitz, S., & Driesner, T. (2010). Numerical simulation of magmatic hydrothermal systems. *Reviews of Geophysics*, *48*(1), RG1002. https://doi.org/10.1029/2009RG000287

Jupp, T., & Schultz, A. (2000). A thermodynamic explanation for black smoker temperatures. *Nature*, *403*(6772), 880–883. https://doi.org/10.1038/35002552

Jupp, T. E., & Schultz, A. (2004). Physical balances in subseafloor hydrothermal convection cells. *Journal of Geophysical Research*, *109*(1–12), B05101. https://doi.org/10.1029/2003jb002697

Kadko, D., & Butterfield, D. A. (1998). The relationship of hydrothermal fluid composition and crustal residence time to maturity of vent fields on the Juan de Fuca Ridge. *Geochimica et Cosmochimica Acta*, *62*(9), 1521–1533. https://doi.org/10.1016/s0016-7037(98)00088-x

15252027, 2022, 12, Downloaded from https://agupubs.onlinelibrary.wiley.com/doi/10.1029/2022GC010524, Wiley Online Library on [21/06/2023]. See the Terms and Conditions (https://onlinelibrary.wiley.com/terms-and-conditions) on Wiley Online Library for rules of use; OA articles are governed by the applicable Creative Commons License

Kadko, D., Koski, R., Tatsumoto, M., & Bouse, R. (1985). An estimate of hydrothermal fluid residence times and vent chimney growth-rates based on ^{210}Pb/Pb ratios and mineralogic studies of sulfides dredged from the Juan de Fuca Ridge. *Earth and Planetary Science Letters*, *76*(1–2), 35–44. https://doi.org/10.1016/0012-821x(85)90146-3

Kadko, D., & Moore, W. (1988). Radiochemical constraints on the crustal residence time of submarine hydrothermal fluids: Endeavour Ridge. *Geochimica et Cosmochimica Acta*, *52*(3), 659–668. https://doi.org/10.1016/0016-7037(88)90328-6

Kanzaki, Y. (2020). Quantifying the buffering of oceanic oxygen isotopes at ancient midocean ridges. *Solid Earth*, *11*(4), 1475–1488. https://doi.org/10.5194/se-11-1475-2020

Kuhn, T., Herzig, P. M., Hannington, M. D., Garbe-Schonberg, D., & Stoffers, P. (2003). Origin of fluids and anhydrite precipitation in the sediment-hosted Grimsey hydrothermal field north of Iceland. *Chemical Geology*, *202*(1–2), 5–21. https://doi.org/10.1016/s0009-2541(03)00207-9

Larson, B. I., Houghton, J. L., Lowell, R. P., Farough, A., & Meile, C. D. (2015). Subsurface conditions in hydrothermal vents inferred from diffuse flow composition, and models of reaction and transport. *Earth and Planetary Science Letters*, *424*, 245–255. https://doi.org/10.1016/j.epsl.2015.05.033

Lilley, M. D., Lupton, J. E., Butterfield, D. A., & Olson, E. (2003). Magmatic events can produce rapid changes in hydrothermal vent chemistry. *Nature*, *422*(6934), 878–881. https://doi.org/10.1038/nature01569

Liu, L., & Lowell, R. P. (2009). Models of hydrothermal heat output from a convecting, crystallizing, replenished magma chamber beneath an oceanic spreading center. *Journal of Geophysical Research*, *114*(B2), B02102. https://doi.org/10.1029/2008JB005846

Lowell, R. P. (1975). Circulation in fractures, hot springs, and convective heat transport on mid-ocean ridge crests. *Geophysical Journal of the Royal Astronomical Society*, *40*(3), 351–365. https://doi.org/10.1111/j.1365-246x.1975.tb04137.x

Lowell, R. P., Farough, A., Hoover, J., & Cummings, K. (2013). Characteristics of magma-driven hydrothermal systems at oceanic spreading centers. *Geochemistry, Geophysics, Geosystems*, *14*(6), 1756–1770. https://doi.org/10.1002/ggge.20109

Lowell, R. P., Yao, Y., & Germanovich, L. N. (2003). Anhydrite precipitation and the relationship between focused and diffuse flow in seafloor hydrothermal systems. *Journal of Geophysical Research*, *108*(B9), 2424. https://doi.org/10.1029/2002jb002371

Lowenstein, T. K., Kendall, B., & Anbar, A. D. (2014). The geologic history of seawater. In *Treatise on geochemistry* (2nd ed., pp. 569–616). Elsevier.

Lowenstein, T. K., Timofeef, M. N., Brennan, S. T., Hardie, A., & Demicco, R. V. (2001). Oscillations in phanerozoic seawater chemistry: Evidence from fluid inclusions. *Science*, *294*(5544), 1086–1088. https://doi.org/10.1126/science.1064280

Machado, N., Brooks, C., & Hart, S. R. (1986). Determination of initial ^{87}Sr/^{86}Sr and ^{143}Nd/^{144}Nd in primary minerals from mafic and ultramafic rocks: Experimental procedure and implications for the isotopic characteristics of the Archean mantle under the Abitibi greenstone belt, Canada. *Geochimica et Cosmochimica Acta*, *50*(10), 2335–2348. https://doi.org/10.1016/0016-7037(86)90086-4

McCulloch, M. T. (1994). Primitive ^{87}Sr/^{86}Sr from an Archean barite and conjecture on the Earth's age and origin. *Earth and Planetary Science Letters*, *126*(1–3), 1–13. https://doi.org/10.1016/0012-821x(94)90238-0

McCulloch, M. T., & Bennett, V. C. (1993). Evolution of the early Earth: Constraints from ^{143}Nd-^{142}Nd isotopic systematics. *Lithos*, *30*(3–4), 237–255. https://doi.org/10.1016/0024-4937(93)90038-e

Michard, G., Albarede, F., Michard, A., Minster, J.-F., Charlou, J.-L., & Tan, N. (1984). Chemistry of solutions from the 13°N East Pacific Rise hydrothermal site. *Earth and Planetary Science Letters*, *67*(3), 297–307. https://doi.org/10.1016/0012-821x(84)90169-9

Mottl, M. J., & Holland, H. D. (1978). Chemical exchange during hydrothermal alteration of basalt by seawater I. Experimental results for major and minor components of seawater. *Geochimica et Cosmochimica Acta*, *42*(8), 1103–1115. https://doi.org/10.1016/0016-7037(78)90107-2

Mottl, M. J., Seewald, J. S., Wheat, C. G., Tivey, M. K., Michael, P. J., Proskurowski, G., et al. (2011). Chemistry of hot springs along the eastern Lau spreading center. *Geochimica et Cosmochimica Acta*, *75*(4), 1013–1038. https://doi.org/10.1016/j.gca.2010.12.008

Mottl, M. J., & Wheat, C. G. (1994). Hydrothermal circulation through mid-ocean ridge flanks: Fluxes of heat and magnesium. *Geochimica et Cosmochimica Acta*, *58*(10), 2225–2237. https://doi.org/10.1016/0016-7037(94)90007-8

Muelenbachs, K. (1998). The oxygen isotope composition of the oceans sediments and the seafloor. *Chemical Geology*, *145*(3–4), 263–273.

Muelenbachs, K., Furnes, H., Fonneland, H. C., & Hellevang, B. (2003). Ophiolites as faithful records of the oxygen isotope ratio of ancient seawater: The solund-stavfjord ophiolite complex as a late Ordovician example. In Y. Dilek & P. T. Robinson (Eds.), *Ophiolites in earth history* (pp. 401–414). Geological Society Special Publication, Geological Society London.

Nehlig, P. (1994). Fracture and permeability analysis in magma-hydrothermal transition zones in the Samail ophiolite (Oman). *Journal of Geophysical Research*, *99*(B1), 589–601. https://doi.org/10.1029/93JB02569

Oelkers, E. H., Schott, J., & Devidal, J.-L. (1994). The effect of aluminum, pH, and chemical affinity on the rates of aluminosilicate dissolution reactions. *Geochimica et Cosmochimica*, *58*(9), 2011–2024. https://doi.org/10.1016/0016-7037(94)90281-x

Ono, S., Shanks III, W. C., Rouxel, O. J., & Rumble, D. (2007). S-33 constraints on the seawater sulfate contribution in modern seafloor hydrothermal vent sulfides. *Geochimica et Cosmochimica Acta*, *71*(5), 1170–1182. https://doi.org/10.1016/j.gca.2006.11.017

Palandri, J., & Kharaka, Y. (2004). A compilation of rate parameters of water–mineral interaction kinetics for Application to geochemical modeling. In *U.S. Geological Survey open file report 2004-1068*.

Palmer, M. R., & Edmond, J. M. (1989). The strontium isotope budget of the modern ocean. *Earth and Planetary Science Letters*, *92*(1), 11–27. https://doi.org/10.1016/0012-821x(89)90017-4

Pester, N. J., Ding, K., & Seyfried, W. E., Jr. (2014). Magmatic eruptions and iron volatility in deep-sea hydrothermal fluids. *Geology*, *42*(3), 255–258. https://doi.org/10.1130/g35079.1

Pester, N. J., Reeves, E. P., Rough, M. E., Ding, K., Seewald, J. S., & Seyfried, W. E., Jr. (2012). Subseafloor phase equilibria in high-temperature hydrothermal fluids of the Lucky Strike Seamount (Mid-Atlantic Ridge, 37°17'N). *Geochimica et Cosmochimica Acta*, *90*, 303–322. https://doi.org/10.1016/j.gca.2012.05.018

Pester, N. J., Rough, M., Ding, K., & Seyfried, W. E., Jr. (2011). A new Fe/Mn geothermometer for hydrothermal systems: Implications for high-salinity fluids at 13°N on the East Pacific Rise. *Geochimica et Cosmochimica Acta*, *75*(24), 7881–7892. https://doi.org/10.1016/j.gca.2011.08.043

Reed, M. H., & Palandri, J. (2006). Sulfide mineral precipitation from hydrothermal fluids. *Reviews in Mineralogy and Geochemistry*, *61*, 609–631. https://doi.org/10.2138/rmg.2006.61.11

Rosenbauer, R. J., & Bischoff, J. L. (1983). Uptake and transport of heavy metals by heated seawater: A summary of the experimental results. In P. A. Rona, K. Bostrom, L. Laubier, & K. L. Smith (Eds.), *Hydrothermal processes at seafloor spreading centers* (pp. 177–197). Plenum Press.

Seyfried, W. E., & Bischoff, J. L. (1979). Low temperature basalt alteration by seawater: An experimental study at 70°C and 150°C. *Geochimica et Cosmochimica Acta*, *43*(12), 1937–1947. https://doi.org/10.1016/0016-7037(79)90006-1

Seyfried, W. E., Jr. (1987). Experimental and theoretical constraints on hydrothermal alteration processes at mid-ocean ridges. *Annual Review of Earth and Planetary Sciences*, *15*(1), 317–335. https://doi.org/10.1146/annurev.ea.15.050187.001533

15252027, 2022, 12, Downloaded from https://agupubs.onlinelibrary.wiley.com/doi/10.1029/2022GC010524, Wiley Online Library on [21/06/2023]. See the Terms and Conditions (https://onlinelibrary.wiley.com/terms-and-conditions) on Wiley Online Library for rules of use; OA articles are governed by the applicable Creative Commons License

Seyfried, W. E., Jr., & Bischoff, J. L. (1981). Experimental seawater-basalt interaction at 300°C, 500 bars, chemical exchange, secondary mineral formation and implications for the transport of heavy metals. *Geochimica et Cosmochimica Acta*, *45*(2), 135–147. https://doi.org/10.1016/0016-7037(81)90157-5

Seyfried, W. E., Jr., & Janecky, D. R. (1985). Heavy metal and sulfur transport during subcritical and supercritical hydrothermal alteration of basalt: Influence of fluid pressure and basalt composition and crystallinity. *Geochimica et Cosmochimica Acta*, *49*(12), 2545–2560. https://doi.org/10.1016/0016-7037(85)90123-1

Seyfried, W. E., Jr., & Mottl, M. J. (1982). Hydrothermal alteration of basalt by seawater under seawater-dominated conditions. *Geochimica et Cosmochimica Acta*, *46*(6), 985–1002. https://doi.org/10.1016/0016-7037(82)90054-0

Seyfried, W. E., Jr., Pester, N., Ding, K., & Rough, M. (2011). Vent fluid chemistry of the Rainbow hydrothermal system (36°N, MAR): Phase equilibria and in-situ pH controls on subseafloor alteration processes. *Geochimica et Cosmochimica Acta*, *75*(6), 1574–1593. https://doi.org/10.1016/j.gca.2011.01.001

Seyfried, W. E., Jr., & Shanks III, W. C. (2004). Alteration and mass transport in mid-ocean ridge hydrothermal systems: Controls on the chemical and isotopic evolution of high-temperature crustal fluids. In E. Davis & H. Elderfield (Eds.), *Hydrogeology of the oceanic lithosphere* (pp. 451–495). Cambridge University Press.

Shields, G., & Veizer, J. (2002). Precambrian marine carbonate carbonate isotope database: Version 1.1. *Geochemistry, Geophysics, Geosystems*, *3*(6), 1–12. https://doi.org/10.1029/2001GC000266

Sleep, N. H. (1991). Hydrothermal circulation, anhydrite precipitation, and thermal structure at ridge axes. *Journal of Geophysical Research*, *96*(B2), 2375–2387. https://doi.org/10.1029/90jb02335

Sleep, N. H., Bird, D. K., & Pope, E. (2012). Paleontology of Earth's mantle. *Annual Review of Earth and Planetary Sciences*, *40*(1), 277–300. https://doi.org/10.1146/annurev-earth-092611-090602

Sleep, N. H., & Zahnle, K. (2001). Carbon dioxide cycling and implications for climate on ancient Earth. *Journal of Geophysical Research*, *106*(E1), 1373–1399. https://doi.org/10.1029/2000je001247

Sonnenthal, E. L., Spycher, N., Xu, T., Zheng, L., Miller, N., & Pruess, K. (2014). TOUGHREACT V3.0-OMP. Retrieved from http://esd.lbl.gov/research/projects/tough/software/toughreact.html

Staudigel, H. (2003). Hydrothermal alteration processes in the oceanic crust. *Treatise on geochemistry*, 511–535. https://doi.org/10.1016/b0-08-043751-6/03032-2

Stein, C. A., & Stein, S. (1994). Constraints on hydrothermal heat-flux through the oceanic lithosphere from global heat flow. *Journal of Geophysical Research*, *99*(B2), 3081–3095. https://doi.org/10.1029/93jb02222

Stern, R. J., & Abdelsalam, M. G. (1998). Formation of juvenile continental crust in the Arabian–Nubian shield: Evidence from granitic rocks of the Nakasib suture, NE Sudan. *Geologische Rundschau*, *87*(1), 150–160. https://doi.org/10.1007/s005310050196

Syverson, D. D., Scheuermann, P., Higgins, J. A., Pester, N. J., & Seyfried, W. E. (2018). Experimental partitioning of Ca isotopes and Sr into anhydrite: Consequences for the cycling of Ca and Sr in subseafloor mid-ocean ridge hydrothermal systems. *Geochimica et Cosmochimica Acta*, *236*, 160–178. https://doi.org/10.1016/j.gca.2018.03.018

Teagle, D. A. H., Alt, J. C., & Halliday, A. N. (1998). Tracing the evolution of hydrothermal fluids in the upper oceanic crust: Sr isotopic constraints from DSDP/ODP Holes 504B and 896A. In R. A. Mills & K. Harrison (Eds.), *Modern ocean-floor processes and the geological record* (Vol. 148, pp. 81–97). Geological Society of London, Special Publication.

Teagle, D. A. H., Bickle, M. J., & Alt, J. C. (2003). Recharge flux to ocean-ridge black smoker systems: A geochemical estimate from ODP Hole 504B. *Earth and Planetary Science Letters*, *210*(1–2), 81–89. https://doi.org/10.1016/s0012-821x(03)00126-2

Theissen-Krah, S., Iyer, K., Rupke, L. H., & Morgan, J. P. (2011). Coupled mechanical and hydrothermal modeling of crustal accretion at intermediate to fast spreading ridges. *Earth and Planetary Science Letters*, *311*(3–4), 275–286. https://doi.org/10.1016/j.epsl.2011.09.018

Theissen-Krah, S., Rüpke, L. H., & Hasenclever, J. (2016). Modes of crustal accretion and their implications for hydrothermal circulation. *Geophysical Research Letters*, *43*(3), 1124–1131. https://doi.org/10.1002/2015GL067335

Turchyn, A. V., & DePaolo, D. J. (2019). Seawater chemistry through phanerozoic time. *Annual Review of Earth and Planetary Sciences*, *47*(1), 197–224. https://doi.org/10.1146/annurev-earth-082517-010305

van Everdingen, D. A. (1995). Fracture characteristics of the sheeted dike complex, Troodos ophiolite, Cyprus: Implications for permeability of oceanic crust. *Journal of Geophysical Research*, *100*(B10), 19957–19972. https://doi.org/10.1029/95JB01575

Varga, R. J., & Moores, E. M. (1985). Spreading structure of the Troodos ophiolite. *Cyprus. Geology*, *13*(12), 846–850. https://doi.org/10.1130/0091-7613(1985)13<846:ssotto>2.0.co;2

Vervoort, J. D., & Blichert-Toft, J. (1999). Evolution of the depleted mantle: Hf isotope evidence from juvenile rocks through time. *Geochimica et Cosmochimica Acta*, *63*(3–4), 533–556. https://doi.org/10.1016/s0016-7037(98)00274-9

Von Damm, K. L. (1995). Controls on the chemistry and temporal variability of seawater hydrothermal fluids. In S. E. Humphris, R. A. Zierenberg, L. S. Mullineaux, & R. E. Thomson (Eds.), *Seafloor hydrothermal systems* (pp. 222–247). American Geophysical Union.

Von Damm, K. L., Edmond, J. M., Grant, B., Measures, C. I., Walden, B., & Weiss, R. F. (1985). Chemistry of submarine hydrothermal solutions at 21°N, East Pacific Rise. *Geochimica et Cosmochimica Acta*, *49*(11), 2197–2220. https://doi.org/10.1016/0016-7037(85)90222-4

Walker, J. C. G., Hays, P. B., & Kasting, J. F. (1981). A negative feedback mechanism for the longterm stabilization of Earth's surface temperature. *Journal of Geophysical Research*, *86*(C10), 9776–9782. https://doi.org/10.1029/jc086ic10p09776

Wheat, C. G., & Mottl, M. J. (2000). Composition of pore and spring waters from Baby Bare: Global implications of geochemical fluxes from a ridge flank hydrothermal system. *Geochimica et Cosmochimica Acta*, *64*(4), 629–642. https://doi.org/10.1016/s0016-7037(99)00347-6

Wolery, T. J., & Sleep, N. H. (1976). Hydrothermal circulation and geochemical flux at mid-ocean ridges. *The Journal of Geology*, *84*(3), 249–275. https://doi.org/10.1086/628195

Xu, T., Spycher, N., Sonnenthal, E., Zhang, G., Zheng, L., & Pruess, K. (2011). TOUGHREACT version 2.0: A simulator for subsurface reactive transport under non-isothermal multiphase flow conditions. *Computers & Geosciences*, *37*(6), 763–774. https://doi.org/10.1016/j.cageo.2010.10.007

Zindler, A. (1982). Nd and Sr isotopic studies of komatiites and related rocks. In N. T. Arndt & E. G. Nisbet (Eds.), *Komatiites, chapter 23* (pp. 399–420). George Allen & Unwin.

References From the Supporting Information

Beig, M. S., & Lüttge, A. (2006). Albite dissolution kinetics as a function of distance from equilibrium: Implications for natural feldspar weathering. *Geochimica et Cosmochimica Acta*, *70*(6), 1402–1420. https://doi.org/10.1016/j.gca.2005.10.035

15252027, 2022, 12, Downloaded from https://agupubs.onlinelibrary.wiley.com/doi/10.1029/2022GC010524, Wiley Online Library on [21/06/2023]. See the Terms and Conditions (https://onlinelibrary.wiley.com/terms-and-conditions) on Wiley Online Library for rules of use; OA articles are governed by the applicable Creative Commons License

Dai, Z., Kan, A. T., Shi, W., Zhang, N., Zhang, F., Yan, F., et al. (2017). Solubility measurements and predictions of gypsum, anhydrite, and calcite over wide ranges of temperature, pressure, and ionic strength with mixed electrolytes. *Rock Mechanics and Rock Engineering*, *50*(2), 327–339. https://doi.org/10.1007/s00603-016-1123-9

Taylor, A. S., Blum, J. D., & Lasaga, A. C. (2000). The dependence of labradorite dissolution and Sr isotope release rates on solution saturation state. *Geochimica et Cosmochimica Acta*, *64*(14), 2389–2400. https://doi.org/10.1016/s0016-7037(00)00361-6

15252027, 2022, 12, Downloaded from https://agupubs.onlinelibrary.wiley.com/doi/10.1029/2022GC010524, Wiley Online Library on [21/06/2023]. See the Terms and Conditions (https://onlinelibrary.wiley.com/terms-and-conditions) on Wiley Online Library for rules of use; OA articles are governed by the applicable Creative Commons License